

TESI DI DOTTORATO

UNIVERSITA' DEGLI STUDI DI NAPOLI "FEDERICO II"



DIPARTIMENTO DI INGEGNERIA ELETTRONICA
E DELLE TELECOMUNICAZIONI

DOTTORATO DI RICERCA IN
INGEGNERIA ELETTRONICA E DELLE TELECOMUNICAZIONI

Airborne Synthetic Aperture Radar
Models, Focusing and Experiments

STEFANO PERNA

Il Coordinatore del Corso di Dottorato
Ch.mo Prof. Giovanni Poggi

Il Tutore
Ch.mo Prof. Giorgio Franceschetti

Anno accademico 2004–2005

to my father

Index

Introduction	1
Chapter 1 SAR Fundamentals	
1.1 Raw data	11
1.2 SAR Transfer Function	19
1.3 SAR focusing	22
1.3.1 Point target analysis	22
1.3.2 Extended scene analysis: range invariant SAR focusing	26
1.3.3 Extended scene analysis: range variant SAR focusing	29
1.4 SAR Interferometry	35
1.4.1 Differential SAR interferometry	40
1.5 Summary	44
Appendixes	45
Tables	49
References	50
Chapter 2 Airborne SAR Acquisition Model	
2.1 Raw data spectrum	54
2.2 Raw data simulation	58
2.2.1 Narrow beam and slow track deviation	61
2.2.1.1 Validity limits	62
2.2.1.2 Simulation results	64
2.2.2 Narrow azimuth beam and arbitrary track deviation	70
2.2.2.1 Simulation results	72
2.2.3 Narrow azimuth beam and moderate track deviation	76
2.2.3.1 Simulation results	80
2.2.4 Computational efficiency	85
2.3 Summary	87
Appendixes	89
References	95
Chapter 3 Accuracy of Airborne SAR Images	
3.1 Airborne SAR focusing: Motion compensation procedure	99
3.2 Residual error sources	104
3.3 Spectral analysis in the presence of residual errors	106

3.4	Effects of residual linear errors	108
3.4.1	Analysis	108
3.4.2	Simulation results	111
3.4.3	Phase accuracy and extension to the interferometric case	116
3.5	Effects of residual quadratic errors	120
3.6	Accuracy of modern aircraft motion sensing systems	124
3.7	Center beam approximation in motion compensation	126
3.7.1	Topography approximation	128
3.7.2	LOS approximation	131
3.8	Summary	137
	Appendixes	139
	References	146

Chapter 4 Airborne SAR Focusing in the Presence of Squint

4.1	SAR squinted data focusing in the absence of track deviations	150
4.2	SAR focusing in conical geometry	153
4.3	Standard MOCO in conical geometry	157
4.4	Motion compensation in the presence of squint	161
4.5	Summary	166
	Appendixes	167
	References	170

Chapter 5 Airborne DIFSAR: Experiments with Real Data

5.1	Motion sensing system requirements	173
5.2	Experimental results	174
	References	181

Introduction

Remote Sensing involves detection and measure, by means of a receiver, of electromagnetic field radiated from distant objects. Generally, the final products of this technology are **images** containing information about the objects under investigation. Such images are basically characterized by a *spatial resolution*, i.e., the minimum distance at which two different objects are detected as separated entities.

Remote sensing is widely used in seismology, hydrology, volcanology and in many other areas of geophysics for risk monitoring and safety.

Remote Sensing imaging sensors can be basically classified as *passive* and *active*: the former make use of the radiation naturally emitted or reflected by Earth's (or any other planet's) surface; the latter are equipped with a transmitting system and receive the signal backscattered from the illuminated surface.

Passive sensors [1], [2] operating in the visible and infrared region of the electromagnetic spectrum, at a few (airborne systems) or at hundreds (spaceborne systems) kilometers of altitude, allow achieving spatial resolution between fractions of meter to a few meters; whereas lower spatial resolution can be achieved when such sensors operate in the microwave region of the electromagnetic spectrum. Principal limitations of passive sensors are represented by lack of an independent source of radiation and by the presence of clouds or fog covering the area of interest.

These limitations are overcome by active sensors that complement passive ones in the existing areas of study, research, and applications.

Imaging active sensors are mostly realized by radar systems [3] operating in the microwave region of the electromagnetic spectrum. The presence of transmitting system renders these sensors independent of external sources (e.g. sunlight); moreover, the used frequency bands drastically reduce the impact of clouds, fog and rain on the obtained images. These features allow night and day and all-weather imaging, an important prerequisite for continuous and global monitoring of Earth's surface. The main limitation of these sensors is the poor resolution achievable with the operating wavelengths. In fact, as shown in Chapter 1, both spaceborne and airborne microwave sensors would require antenna dimensions between hundreds of meters to some kilometers (depending on the transmitted wavelength and on the sensor altitude) to achieve resolutions on the order of magnitude of meters.

In order to overcome this limitation, use of the concept of the *synthetic antenna* also referred to as *synthetic aperture*, can be conveniently be made: a very large antenna is synthesized by moving a small one along the platform flight path. The synthesis is carried out by coherently combining the

backscattered echoes received (and recorded) onboard along the flight path. Accordingly, Synthetic Aperture Radar (SAR) data received onboard (*raw data*) must be properly *processed*: such an operation, also referred to as SAR *focusing* [4], [5] leads to an along path resolution independent of the used wavelength, and of the order of the along path physical antenna dimension.

SAR all-weather, day and night imaging capabilities coupled with the achievable high resolutions make it a fundamental instrument for Earth [6] and other planet [7] observation.

Moreover, use of two antennas has extended SAR applications to the generation of three-dimensional (3D) images [8] of the illuminated surface. This result is possible thanks to the so called SAR interferometry (IFSAR) technique, which exploits the phase difference (*phase interferogram*) between the two images generated by two antennas pointing to the same area with slightly different observation angles. The two antennas can be present at the same time [9] on the aircraft or spacecraft (*single-pass interferometry*) or can be synthesized by two subsequent passages [10] of the platform (*repeat-pass interferometry*).

An interesting extension of *repeat-pass* IFSAR, is a relatively new technique, referred to as differential SAR interferometry (DIFSAR), which exploits the phase difference between SAR image pairs acquired at different times, in order to detect the relative displacement occurred in the illuminated surface between the different acquisitions [11]. This DIFSAR technique makes SAR sensors powerful instruments for forecasting environmental hazard on one hand [12], and for evaluation of environmental damages on the other [13].

Satellite DIFSAR allows, today, generating spatially dense surface deformation maps with centimeter to millimeter accuracy, with no environmental impact on the investigated areas. Furthermore, different algorithms have been recently proposed [14], [15] and successfully applied [16] to detect and follow the temporal evolution of deformations via the generation of time series.

Unfortunately, this powerful technique is strongly limited by the use of satellite SAR sensors. Satellites orbits, indeed, are governed by celestial laws; this implies, first of all, that the repeat cycle of satellites (often referred to as *revisiting time*), after which the same region is imaged again, is fixed and cannot be changed in the case of emergencies. Moreover, the orbits covered by remote sensing satellites, cannot allow North-South deformation detections. Accordingly, spaceborne sensors could be not flexible enough to be really helpful in catastrophe management, and exploitation of a more flexible use of the DIFSAR technique is thus today needed.

In this context airborne SAR platforms could allow overcoming the above mentioned limits also assuring spatial resolutions higher than those of

satellite SAR sensors, due to smaller acceptable dimensions of transmitting antennas. Unfortunately, extension of satellite SAR techniques to the airborne case is not always straightforward.

In this thesis the study of problems related to the use of airborne SAR data is addressed.

Airborne SAR acquisition *model* is deeply analyzed, and realization of an efficient airborne raw data simulator, which represents a useful tool for mission planning, SAR system design and inversion algorithm testing, is presented (Chapter 2).

The analysis of the airborne acquisition model allows also highlighting problems related to airborne SAR *focusing*. In particular, a quantitative analysis of the accuracy achievable by airborne SAR images is performed; extension to the airborne repeat pass interferometry is also included (Chapter 3). Such an analysis allows, on one side, quantifying the airborne repeat pass interferogram phase accuracy in terms of the expected motion measurement system accuracy (Chapter 3); on the other side, designing a new efficient airborne SAR processor (Chapter 4).

Theoretical results presented in Chapter 3 are, finally, validated by an airborne differential interferometry *experiment* carried out by using real data. (Chapter 5).

As far as airborne SAR raw data simulator realization is concerned, it must be noted that a 2-D Fourier domain SAR raw signal simulator, exploiting the efficiency of FFT algorithms, was presented in [17]-[19] and is able to generate the raw signal corresponding to extended scenes. Unfortunately, it is based on the assumption that the sensor flight path is a straight line. This is usually a good approximation for a short portion of the elliptical orbit of a spaceborne sensor, whereas in the case of airborne sensors significant deviations from the ideal trajectory as well as attitude and forward velocity deviations frequently occur due to atmospheric turbulences [20], [21]. In the SAR jargon, raw data acquired in this condition are said to be affected by motion errors.

Such errors introduce space variant aberrations, which are not accounted for by the SAR raw data simulator of [17]-[19].

In Chapter 2, the possibility to extend the efficient Fourier domain simulation approach [17]-[19] to the case of sensor trajectory deviations, which is more realistic for airborne SAR systems, is explored.

A general, i.e., without approximations, and compact Fourier Domain formulation of the SAR raw signal acquired in the presence of arbitrary trajectory deviations is presented.

Such a formulation allows showing that in this general case no efficient simulation scheme can be devised. However, it is demonstrated that, if some reasonable assumptions on the sensor motion and on the SAR system

features are made, an efficient simulation approach can be used: it consists of a 1-D azimuth Fourier domain processing followed by a range time domain integration. This approach turns out to be still much more efficient than the time domain ones presented in [22]-[25], so that airborne raw data acquired in the presence of track deviations and relative to extended scenes can be simulated, for the first time, in a few minutes.

In addition, it is also shown that if a narrow beam and slow trajectory deviation assumption is made, a full 2-D Fourier domain simulation can be used. This latter approach can be applied only to some SAR systems, but it has the advantage that processing time is practically not increased with respect to the nominal trajectory case.

Turning to the problems related to airborne SAR focusing, in Chapter 3 a deep analysis of the accuracy of airborne SAR image is performed.

Indeed, motion errors occurring at raw data level must be properly accounted for during the focusing stage; accordingly, implementation of the so called Motion Compensation (MOCO) procedures is required [20], [21], [26]-[30].

However, correct implementation of MOCO algorithms requires knowledge of both sensor position and topographic profile of the illuminated area; flight parameters are thus measured onboard with Global Positioning Systems (GPS) and Inertial Navigation Units (INU), and use of a Digital Elevation Model (DEM) of the illuminated scene is also needed. Accordingly, inaccuracies of the available DEM and of the motion sensing system mounted onboard the aircraft could generate amplitude and phase residual aberrations in final airborne SAR images.

Moreover, even in the absence of residual errors induced by DEM and GPS/INU inaccuracies, image aberrations may appear in final airborne SAR images due to approximations commonly adopted by efficient MOCO procedures [21], [26], [30]. In fact, a space-variant processing, tailored to each illuminated target, would be, in principle, necessary to fully compensate the space-variant aberrations induced by motion errors. However, although precise, this approach is extremely time consuming: approximations involving airborne raw data features are thus commonly needed [20] to allow efficient incorporation of MOCO within 2D frequency-based SAR processing algorithms [4].

In Chapter 3, it is shown that uncompensated motion errors, introduced by inaccuracies of the available DEM and/or of motion sensing instruments mounted onboard the aircraft, as well as by approximations commonly adopted by efficient MOCO algorithms, not only introduce range and azimuth target location errors and phase calibration losses in the focused images (geometrical errors) [31], but also generate additional phase artifacts.

These artifacts are introduced by the SAR focusing operation and play an important role in interferometric applications.

In particular, it is shown that residual image aberrations in single pass airborne IFSAR are intrinsically mitigated by the system.

Major problems arise when repeat pass airborne IFSAR is addressed: this is of key interest in differential interferometry where data are not acquired simultaneously. In this case uncompensated trajectory deviations due to positioning measurement instruments or DEM inaccuracies may be significantly different in the two channels: accordingly, the final repeat-pass interferogram not only shows differential geometric phase errors, which are well known in the literature [31], but also differential phase artifacts. These artifacts, unlike the differential geometric phase errors, cannot be compensated by using known residual post processing compensation algorithms [31], [32]. However, the theoretical analysis presented in Chapter 3 allows quantifying the repeat pass interferogram phase accuracy in terms of the expected motion sensing system accuracy.

Turning to approximations adopted by airborne SAR MOCO procedures, it must be noted that due to platform attitude instabilities, airborne SAR raw data may be acquired in “squinted” geometries [26], [33], i.e., with an offset angle (*squint* angle) of the radar beam from broadside direction. In Chapter 3 the concept of *isomoco lines* (ground lines where MOCO approximations are minimized) is introduced to explain how squint angle and track deviations introduce defocusing in the final image when standard MOCO algorithms are used [21]. In particular, in Chapter 4, the role played by the so called range-curvature compensation procedure during the compensation of motion errors in the presence of squint is highlighted. Based on this analysis, realization of a new efficient airborne SAR processor, able to deal with both, airborne track deviations and attitude instabilities is also presented in Chapter 4.

Finally, results of an airborne differential interferometry *experiment* carried out by using the X-band OrbiSAR system [34], which is equipped by a motion measurement system fulfilling the requirements fixed in Chapter 3, are shown in Chapter 5.

Final comments are now in order.

The thesis is organized in five chapters and Chapter 1 presents the basic rationale of SAR technique. The assumption that the sensor flight path is a straight line is adopted in the first chapter, which is preliminary to the subsequent analysis, and allows introducing the formalism adopted in Chapters 2-5, where the assumption of straight flight path, not realistic for airborne systems, is relaxed, and the original results of this thesis are presented.

In order to make reading of this thesis easier, a short description of symbols introduced in Chapter 1 and largely used in Chapters 2-5 is collected in Table of Symbols.

Finally, it must be noted that a great part of the material presented from a systematic and unitary point of view in this thesis, has been already published by the author in the last three years, see [35]-[48].

References

- [1] R.N. Colwell; Manual of Remote Sensing, American Society of Photogrammetry, Falls Church, VA, 1983.
- [2] C. Elachi; Introduction to Physics and Techniques of Remote Sensing, John Wiley & Sons, New York, 1987.
- [3] C. Elachi; Spaceborne Radar Remote Sensing: Applications and Techniques, IEEE Press, New York, 1988.
- [4] G. Franceschetti and R.Lanari; Synthetic Aperture Radar Processing, CRC PRESS, New York, 1999
- [5] C.A. Wiley; Pulsed Doppler radar methods and apparatus, U.S. Patent 3,196,436, filed in 1954, 1965.
- [6] C. Elachi; "Radar images of the earth", *Sci. Am.*, 271, 54, 1982.
- [7] L.E. Roth and S.D. Wall; "The face of Venus, the Magellan_Radar-Mapping Mission"; National Aeronautics and Space Administration, Washington, D.C., 1995.
- [8] L.C. Graham; "Synthetic interferometer radar for topographic mapping", *Proc. IEEE*, 62, 763, 1974.
- [9] S. Madsen, H.A. Zebker and J. Martin; "Topographic mapping using radar interferometry: processing techniques", *IEEE Trans. Geosci. Remote Sens.*, 34, 246, 1993.
- [10] H.A. Zebker and R.M. Goldstein; "Topographic mapping from synthetic aperture radar observations", *J. Geophys. Res.*, 91, 4993, 1986.
- [11] K. Gabriel, R. M. Goldstein and H. A. Zebker; "Mapping small elevation changes over large areas: Differential interferometry", *J. Geophys. Res.*, 94, 1989.
- [12] D. Massonnet, P. Briole and A. Arnaud; "Deflation of Mount Etna monitored by spaceborne radar interferometry", *Nature*, London, 375, 567, 1995.
- [13] D. Massonnet, M. Rossi, C. Carmona, F. Ardagna, G. Peltzer, K. Feigl and T. Rabaute; "The displacement field of the Landers earthquake mapped by radar interferometry", *Nature*, 364, 138-142, 1993
- [14] A. Ferretti, C. Prati and F. Rocca; "Permanent scatterers in SAR interferometry", *IEEE Trans. Geosci. Remote Sens.*, 39, 1, 2001.
- [15] P. Berardino, G. Fornaro, R. Lanari and E. Sansosti; "A new Algorithm for Surface Deformation Monitoring based on Small Baseline

Differential SAR Interferograms”, *IEEE Trans. Geosci. Remote Sens.*, 40, 11, 2002.

[16] A. Borgia, P. Tizzani, G. Solaro, M. Manzo, F. Casu, G. Luongo, A. Pepe, P. Berardino, G. Fornaro, E. Sansosti, G.P. Ricciardi, N. Fusi, G. Di Donna and R. Lanari; “Volcanic spreading of Vesuvius, a new paradigm for interpreting its volcanic activity”, *Geoph. Res. Lett.*, 32, L03303, doi:10.1029/2004GL022155.

[17] G.Franceschetti, M.Migliaccio, D.Riccio and G.Schirinzi; “SARAS: a SAR raw signal simulator”, *IEEE Trans. Geosci. Remote Sens.*, 30, 1992.

[18] G.Franceschetti, M.Migliaccio and D.Riccio; “SAR simulation of actual ground sites described in terms of sparse input data”, *IEEE Trans. Geosci. Remote Sens.*, 32, 1994.

[19] G.Franceschetti, A.Iodice, M.Migliaccio and D.Riccio, “A Novel Across-Track SAR Interferometry Simulator”, *IEEE Trans. Geosci. Remote Sens.*, 36, 1998.

[20] S.Buckreuss; “Motion errors in airborne synthetic aperture radar system”, *European Trans. Telecommunications*, 2, 1991.

[21] G.Fornaro; “Trajectory Deviations in Airborne SAR: Analysis and Compensation”, *IEEE Trans. Aerosp. Electron. Syst.*, vol. 35, pp.997-1009, July 1999.

[22] A.Mori and F.De Vita; “A time-domain raw signal Simulator for interferometric SAR”, *IEEE Trans. Geosci. Remote Sens.*, 42, 2004.

[23] H.J.Song, M.H.Zhu and Y.T.Bai; “Design of general purpose simulation package of SAR system”, *Proc. Radar 97*, 697-699, 1997

[24] L.de Salvador, P.Bemad, A.Fidalgo, G.Ilundain, J.M.Dominguez and L.Ojalvo; “IFSAR: an airborne interferometric SAR simulator”, *Proc. IGARSS’04*, Anchorage, 2004.

[25] E.Boerner, R.Lord, J.Mittermayer and R.Bamler; “Evaluation of TerraSAR-X Spotlight processing accuracy based on a new Spotlight raw data simulator”, *Proc. IGARSS*, Toulouse 2003.

[26] A.Moreira and Y.Huang; “Airborne SAR Processing of highly squinted data using a chirp scaling approach with integrated motion compensation”, *IEEE Trans. on Geosci. Remote Sensing*, vol. 32, pp. 1029-1040, Sept.1994.

[27] S. Madsen; “Motion Compensation for Ultra Wide Band SAR”, *Proc. IGARSS*, Sydney, 2001.

- [28] P.Prats, A.Reigber and J.J.Mallorqui; "Topography Dependent Motion Compensation Repeat-pass Interferometric SAR Systems", IEEE Geosci. and Rem. Sensing Lett., 2, 2005.
- [29] K.A.C.de Macedo and R.Scheiber; "Precise Topography-and Aperture Dependent Motion Compensation for Airborne SAR", IEEE Geosci. and Rem. Sensing Lett., 2, 2005.
- [30] E.Alivizatos, A.Potsis, A.Reigber, A. Moreira and N. Uzunoglu; "SAR Processing with motion compensation using the extended wavenumber algorithm", Proc. EUSAR, Ulm, 2004.
- [31] A.Reigber and K.P.Papathanassiou; "Correction of residual motion errors in airborne repeat-pass interferometry", Proc. IGARSS, Sydney, 2001.
- [32] A.Reigber and R.Scheiber; "Airborne Differential SAR Interferometry: first results at L-band", IEEE Trans. Geosci. Remote Sens., 41, 6, 2003.
- [33] G.Fornaro, E.Sansosti, R.Lanari and M.Tesauro; "Role of Processing Geometry in SAR Raw Data Processing", IEEE Trans. Aerosp. Electron. Syst., vol. 38, pp.441-454, April 2002.
- [34] M.Rombach, A.Fernandes, D.Luebeck and J.Moreira; "Newest Technology for mapping using airborne interferometric synthetic aperture radar systems", Proc. IGARSS, Toulouse, 2003.
- [35] G.Fornaro, G.Franceschetti, S.Perna and E.Sansosti; "Phase Accuracy of Motion Compensated Airborne SAR Images", Proc. IGARSS, Toulouse, 2003.
- [36] G.Fornaro, G.Franceschetti and S.Perna; "Motion Compensation of Squinted Airborne SAR Raw Data: Role of Processing Geometry", Proc. IGARSS, Anchorage, 2004.
- [37] G.Fornaro, G.Franceschetti and S.Perna; "Approssimazioni nella compensazione degli errori di moto di dati SAR"; atti del III Workshop Associazione Italiana Telerilevamento, Napoli, 2004.
- [38] G. Fornaro, G. Franceschetti, A. Gois, R. Lanari, J. Moreira, S. Perna and E.Sansosti; "Airborne Differential Interferometry: X-Band Experiments", Proc. IGARSS, Anchorage, 2004.
- [39] S.Perna, G.Fornaro, G.Franceschetti and E.Sansosti; "Experimental Results on Airborne Differential Interferometry"; Proc. 2004 IEEE GOLD Remote Sens. Conf., Napoli, 2004.
- [40] G.Fornaro, G.Franceschetti, R.Lanari, S.Perna and E.Sansosti; "Esperimenti di Interferometria Differenziale SAR da Aereo"; atti della XV Riunione Nazionale di Elettromagnetismo, Cagliari, 2004.

- [41] S.Perna, G.Fornaro and G.Franceschetti; “Airborne Repeat Pass Interferometry with X-Band OrbiSAR Data”; Atti della Fondazione Giorgio Ronchi, Anno LX, N.4, 2005.
- [42] G.Franceschetti, A.Iodice, S.Perna and D.Riccio; “2-D Fourier Domain SAR Raw Signal Simulation Accounting for Sensor Trajectory Deviations”; proc. IGARSS, IEEE International Geoscience & Remote Sensing Symposium, Seoul, 2005.
- [43] G.Fornaro, G.Franceschetti and S.Perna; “Motion Compensation Errors: Effects on the Accuracy of Airborne SAR Images”, in press on IEEE Trans. Aerosp. Electron. Syst..
- [44] G.Fornaro, G.Franceschetti and S.Perna; “On Center Beam Approximation in SAR Motion Compensation”; in press on IEEE Geosci. Remote Sens. Lett.
- [45] G.Franceschetti, A.Iodice, S.Perna and D.Riccio; “SAR Sensor Trajectory Deviations: Fourier Domain Formulation and Extended Scene Simulation of Raw Signal”; submitted to IEEE Trans. Geosci. Remote Sens.
- [46] G.Franceschetti, A.Iodice, S.Perna and D.Riccio; “Efficient Simulation of Airborne SAR Raw Data of Extended Scenes”; submitted to IEEE Trans. Geosci. Remote Sens.
- [47] G.Franceschetti, A.Iodice, S.Perna and D.Riccio; “A Novel Airborne SAR Simulator”; submitted to EUSAR, 6th European Conference on Synthetic Aperture Radar, Dresden, 2006.
- [48] G.Fornaro, G.Franceschetti and S.Perna; “Approximations in Efficient 2-D SAR Motion Compensation”; submitted to EUSAR, 6th European Conference on Synthetic Aperture Radar, Dresden, 2006.

Chapter 1

SAR Fundamentals

In the following we introduce basic concepts relative to Synthetic Aperture Radar (SAR). The assumption that the sensor flight path is a straight line is made in this chapter. This is usually a good approximation for a short portion of the elliptical orbit of a spaceborne sensor. However, in the case of airborne sensors, significant deviations from the ideal trajectory, due to the presence of atmospheric turbulences, may occur: the analysis of the effects of these deviations represent one of the goals of this thesis and is deeply performed in the next chapters.

1.1 Raw data

Let us refer to Fig. 1, where the SAR system geometry is depicted: a cylindrical reference system, the axis (azimuth direction) of which coincides with the sensor flight path, is considered. Let us denote with:

- (x,r) the azimuth and (slant) range coordinates of the scene generic scattering point P ;
- $\vartheta(x,r)$ the soil surface equation in cylindrical coordinates, also referred to as *look angle*;
- R the target-to-antenna distance in the generic antenna position.

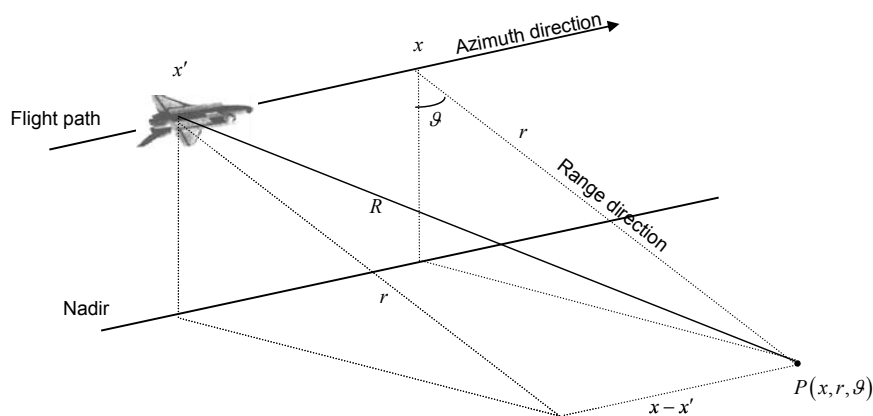


Figure 1 SAR system geometry.

The SAR sensor is located on the platform that moves at velocity supposed to be constant and equal to $\vec{v} = v \cdot \hat{x}$. At times $t_n - \tau/2$, the sensor radiates pulses represented, but for an amplitude factor, by:

$$f_{tx}(t) = \exp(j2\pi f t) p(t - t_n) \text{rect}\left[\frac{t - t_n}{\tau}\right], \quad (1)$$

where $p(t - t_n)$ describes the signal modulation, τ represents the duration of the transmitted pulse, and f is the carrier frequency.

In order to analyze characteristics and properties of the signal backscattered and received onboard, in the following, we first consider an elementary scene consisting of a single scatterer, and then, we extended our analysis to the case of extended scene.

Accordingly, let us consider the elementary scatterer located at $P \equiv (x, r, \vartheta)$, see Fig. 1. The signal backscattered and received onboard is given by:

$$f_r(x - x_n, t - t_n, r) = \gamma(x, r) \exp\left(-j2\pi f \frac{2R}{c}\right) p\left(t - t_n - \frac{2R}{c}\right) \cdot \text{rect}\left[\frac{t - t_n - \frac{2R}{c}}{\tau}\right] w^2[x_n - x, r] \quad (2)$$

where the fast-varying $\exp(j\omega t)$ term of eq.(1) is cancelled by the heterodyne process, and where:

- $x_n = vt_n$ is the azimuth coordinate of the antenna phase center;
- $\gamma(x, r)$ is the *reflectivity pattern* proportional to the ratio between backscattered and incident field;
- c is the speed of the light;
- $w(\cdot)$ is the antenna illumination function, related to the azimuth antenna footprint over the ground.

The latter term is squared in eq. (2) because the same antenna operates also in the receive mode. Equation (2) assumes the platforms to move in a *stop and go way*, in the sense that the system is supposed to transmit and receive the same pulse at the same position: it can be shown [1] that this is a reasonable approximation for all the available SAR systems. From Fig. 1 we have:

$$R = R(x_n - x, r) = \sqrt{r^2 + (x_n - x)^2}. \quad (3)$$

Let us now change the time coordinates in range (spatial) coordinates as follows:

$$r' = \frac{ct'}{2} \quad (4)$$

with:

$$t' = t - t_n. \quad (5)$$

Moreover, we assume the discrete x_n -coordinate to be continuous, that is,

$$x_n \rightarrow x'. \quad (6)$$

Accordingly, eq. (2) can be rewritten as follows:

$$f_r(x' - x, r', r) = \gamma(x, r) \exp\left(-j \frac{4\pi}{\lambda} R\right) p\left[\frac{2}{c}(r' - R)\right] \cdot \text{rect}\left[\frac{r' - R}{c\tau/2}\right] w^2[x' - x, r] \quad (7)$$

where $\lambda=c/f$ is the carrier wavelength. Equation (7) can be easily rearranged as follows:

$$f_r(x' - x, r' - r, r) = \gamma(x, r) \text{rect}\left[\frac{r' - r - \Delta R}{c\tau/2}\right] w^2[x' - x, r] \exp\left[-j \frac{4\pi}{\lambda}(r + \Delta R)\right] p\left[\frac{2}{c}(r' - r - \Delta R)\right] \quad (8)$$

where ΔR is given by:

$$\Delta R(x' - x, r) = R - r = \sqrt{r^2 + (x' - x)^2} - r, \quad (9)$$

and use of (6) in eq. (3) has been made in the last equation.

Some considerations on eq.(8) are now in order.

First of all we underline that eq. (8) represents the signal backscattered by an isolated point target located at fixed range and azimuth coordinates (x, r) and received onboard. In particular, we must note that in eq.(8) x and r are fixed; conversely, x' and r' do vary: they represent the spatial coordinates of the received two-dimensional image $fr(\cdot)$.

As a matter of fact, we must observe that the signal $fr(\cdot)$ collected onboard, referred to as *raw data relative to $P(x, r)$* in the following, represents an estimate of the *reflectivity pattern* $\gamma(x, r)$ of the illuminated point target. In order to evaluate how much accurate this estimate is, we now

focus our attention on the geometric resolution achievable by the received data $f_r(\cdot)$. Simply speaking, geometric resolution is the ability of the system to localize nearby objects. More precisely, the resolution length is the minimum spacing between two objects that are detected as separate entities, and are, therefore, *resolved*. In the two-dimensional received data we have the azimuth and the range resolution, hereafter denoted as Δx_{raw} and Δr_{raw} , respectively.

Range resolution of the received, i.e., raw, data is now addressed.

The range resolution of the raw data is clearly given by the spatial extension of the $\text{rect}(\cdot)$ function in (8), that is:

$$\Delta r_{raw} = \frac{c\tau}{2}. \quad (10)$$

Accordingly, very short pulse durations τ are needed ($\tau \approx 10^{-8} \div 10^{-7}$ s) to achieve a range resolution of some meters (c being approximately 3×10^8 m/s). Improvement of the range resolution requires a reduction of the pulse width, and high peak power for a prescribed mean power operation. A way to circumvent this limitation is to substitute the short pulses by modulated long ones, provided that they are followed by a processing step (usually referred to as *pulse compression*). To this end, the very popular linear frequency modulation is commonly adopted; in this case $p(t)$ in eq.(1) becomes:

$$p(t) = \exp\left[-j\frac{\alpha t^2}{2}\right], \quad (11)$$

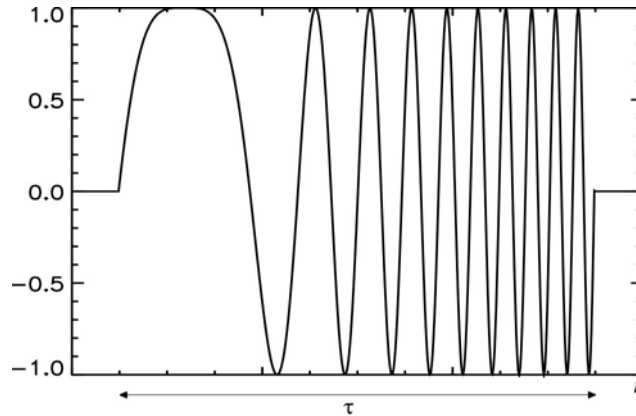


Figure 2 Chirp waveform. Arbitrary units. $\alpha > 0$

where α is the chirp rate; it can be shown that for large value of $\alpha\tau^2$ we have:

$$\alpha\tau = 2\pi\Delta f \quad (12)$$

being Δf the bandwidth [Hz] of the transmitted pulse.

In this case, $f_{rx}(t)$ in (1) becomes the so-called *chirp pulse*, the real part of which is depicted in Fig. 2, and eq.(8) can be rewritten as follows:

$$f_r(x' - x, r' - r, r) = \gamma(x, r) \operatorname{rect}\left[\frac{r' - r - \Delta R}{c\tau/2}\right] w^2[x' - x, r] \exp\left[-j\frac{4\pi}{\lambda}(r + \Delta R)\right] \exp\left[\frac{2\alpha}{c^2}(r' - r - \Delta R)^2\right] \quad (13)$$

Pulse compression consists of convolution of (13) with the reference function:

$$rf(r') = \exp\left[j\frac{2\alpha}{c^2}r'^2\right] \operatorname{rect}\left[\frac{r'}{c\tau/2}\right]; \quad (14)$$

it is easy to show [1] that this step allows obtaining the following resolution:

$$\Delta r = \frac{c}{2\Delta f} = \frac{\pi c}{\alpha\tau}; \quad (15)$$

which is of some meters, if use of larger pulse durations ($\tau \approx 10^{-6}$ s) is coupled with adoption of very large chirp rates ($\alpha \approx 10^{14}$ rad·s⁻²). A more detailed analysis of this processing step, along with an analysis in the Fourier domain, is performed in Sect 1.3.

Azimuth resolution of the received, i.e., raw, data is now addressed.

According to eqs.(8) and (13), two targets at a given range can be resolved only if they are not within the radar beam at the same time. Accordingly, the azimuth resolution of the raw data coincides with the antenna azimuth footprint X related, in turn, to the antenna beam width λ/L by means of the relation:

$$\Delta x_{raw} = X = r_0 \frac{\lambda}{L} \quad (16)$$

where L is the (effective) antenna dimension along the azimuth direction. Equation (16) represents the resolution limit of a conventional *side-looking Real Aperture Radar*, commonly referred to as RAR. To have an idea of the

achievable azimuth resolutions let us apply eq.(16) to the ERS* sensor parameters collected in Table I: the azimuth resolution is of the order of kilometers and this is not acceptable for most application. On the other side, airborne sensors ($r_0 \approx 1 \div 10$ km, and $L \approx 1$ m) may achieve azimuth resolution of the order of hundreds of meters, which is not acceptable too. To improve the azimuth resolution we must reduce the wavelength of the carrier frequency and/or increase the antenna dimension. The former is constrained by system characteristics. The latter is not an easy task, unless we implement the synthetic antenna (or aperture): a very large antenna is synthesized by moving along a reference path a real one of limited dimension, see Fig. 3.

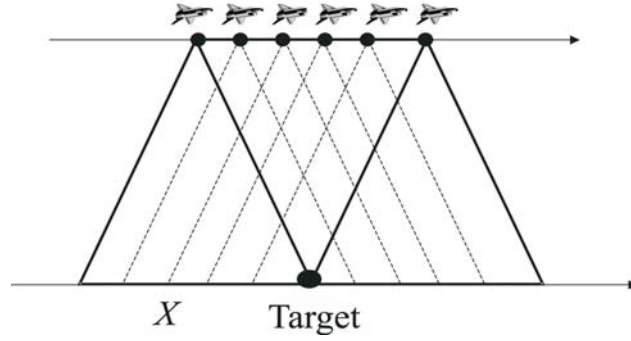


Figure 3 Synthetic aperture concept.

The synthesis is carried out by coherently combining the back-scattered echoes received and recorded along the flight path. A more detailed analysis of this operation is addressed in Sect. 1.3; however, at this stage we can observe that a second order expansion of the ΔR term in eq.(9) leads to:

$$\Delta R \approx \frac{(x' - x)^2}{2r}, \quad (17)$$

accordingly, eq.(13) can be rewritten as follows:

$$f_r(x' - x, r' - r, r) \approx \gamma(x, r) \text{rect} \left[\frac{r' - r - \Delta R}{c\tau/2} \right] w^2[x' - x, r] \cdot \exp \left[-j \frac{4\pi}{\lambda} r \right] \exp \left[-j \frac{4\pi}{\lambda} \frac{(x' - x)^2}{2r} \right] \exp \left[\frac{2\alpha}{c^2} (r' - r - \Delta R)^2 \right] \quad (18)$$

* ERS-1 and ERS-2 are two flying C-band SAR sensors launched in 1991 and 1995, respectively, by the European Space Agency (ESA).

thus exhibiting an interesting characteristic, which is now addressed. The second exponential term in eq.(18) is similar to the chirp term of the third exponential in the same equation; this suggests, also for the azimuth case, a processing procedure similar to that considered for the range case, aimed at improving the azimuth resolution of eq.(16). Similarly to range pulse compression, also this procedure is deeply investigated in Sect. 1.3.

In summary, we can say, according to eqs. (10) and (16), which are the range and the azimuth resolution (see Fig. 4) of the SAR raw data collected onboard, that eq.(8) represents a bad estimate of the reflectivity pattern $\rho(x,r)$ in terms of geometrical resolution.

This problem can be tackled, for what concerns the range direction, by transmitting chirp pulses (or other modulated pulses), provided that they are followed by a proper processing step.

As far as azimuth direction is concerned, we observe that the sensor movement “generates” approximately a chirp also along this direction, see eq.(18); accordingly, a strategy similar to that adopted for the range direction can be followed to improve the azimuth resolution, too; this is equivalent to synthesize a very large antenna along the azimuth direction.

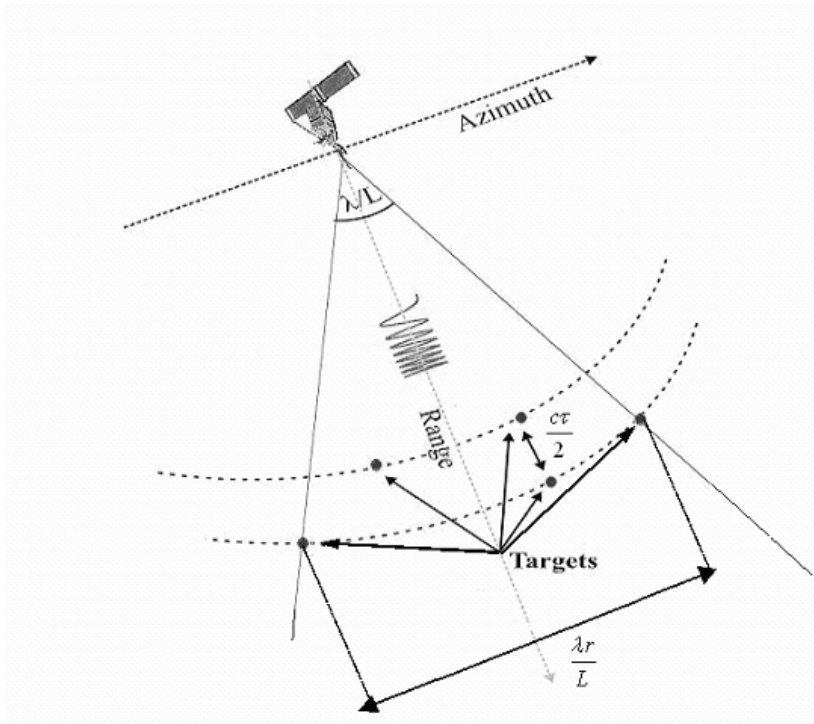


Figure 4 Geometric resolutions of the raw data.

Let us now move to consider SAR raw data collected in the presence of an extended scene.

In the situation of a continuous distribution of scatterers described by a *reflectivity pattern* $\gamma(x,r)$ proportional to the ratio between backscattered and incident field, the signal collected onboard, i.e., the *raw data*, can be obtained from eq.(8) by superimposing all the elementary returns from the illuminated surface, hence:

$$h(x',r') = \iint dx dr \gamma(x,r) \exp\left(-j\frac{4\pi}{\lambda}r\right) \exp\left(-j\frac{4\pi}{\lambda}\Delta R\right) \times \\ \times p\left[\frac{2}{c}(r'-r-\Delta R)\right] \text{rect}\left[\frac{r'-r-\Delta R}{c\tau/2}\right] w^2[x'-x,r], \quad (19)$$

Equation (19) can be recast in most compact form:

$$h(x',r') = \iint dx dr \gamma(x,r) \exp\left[-j\frac{4\pi}{\lambda}r\right] g(x'-x,r'-r,r), \quad (20)$$

where:

$$g(x'-x,r'-r,r) = \text{rect}\left[\frac{r'-r-\Delta R}{c\tau/2}\right] w^2[x'-x,r] \\ \exp\left(-j\frac{4\pi}{\lambda}\Delta R\right) \cdot p\left[\frac{2}{c}(r'-r-\Delta R)\right] \quad (21)$$

is the *impulse response* of the system (i.e., the return due to a *unitary point target*).

Equation (20) represents the basic functional form of the SAR raw signal. It exhibits the relationship between the recorded signal, $h(\cdot)$, the reflectivity pattern, $\gamma(\cdot)$, and the SAR system impulse response $g(\cdot)$, the latter depending on the physical parameters of the SAR system. Equation (20) clearly shows that the SAR imaging problem, aimed at improving the geometric resolutions (10) and (16), can be managed via an appropriate filter operation that recovers an high resolution estimate of the reflectivity pattern $\gamma(\cdot)$, starting from the received signal, i.e., the raw data $h(\cdot)$.

Hereafter, although not necessary for the subsequent analysis, the assumption of a chirp modulation, which implies use of eq.(11) in eq.(1), is made. In this case eq.(21) becomes:

$$g(x' - x, r' - r, r) = \text{rect}\left[\frac{r' - r - \Delta R}{c\tau/2}\right] w^2\left[\frac{x' - x}{X}\right] \cdot \exp\left(-j\frac{4\pi}{\lambda}\Delta R\right) \cdot \exp\left[-j\frac{2\alpha}{c^2}(r' - r - \Delta R)^2\right] \quad (22)$$

where the r -dependence of $w(\cdot)$ is now accounted for through the azimuth footprint X term [1], see eq.(16). From eq.(22) we obtain the general expression of the SAR raw data (20) when a chirped pulse is transmitted:

$$h(x', r') = \iint dx dr \gamma(x, r) \text{rect}\left[\frac{r' - R}{c\tau/2}\right] w^2\left[\frac{x' - x}{X}\right] \cdot \exp\left(-j\frac{4\pi}{\lambda}R\right) \cdot \exp\left[-j\frac{2\alpha}{c^2}(r' - R)^2\right] \quad (23)$$

1.2 SAR Transfer Function

In this Section, we evaluate the *Transfer Function* (TF) of the SAR system, by calculating the 2D Fourier Transform (FT) of the raw data.

Starting from eq.(20) we can obtain the following expression for the raw data spectrum:

$$\begin{aligned} H(\xi, \eta) &= \iint dx' dr' h(x', r') \exp(-j\xi x') \exp(-j\eta r') \\ &= \iint dx dr \bar{\gamma}(x, r) \iint dx' dr' g(x - x', r - r', r) \exp(-j\xi x') \exp(-j\eta r') \quad (24) \\ &= \iint dx dr \bar{\gamma}(x, r) \exp(-j\xi x) \exp(-j\eta r) G(\xi, \eta, r) \end{aligned}$$

where:

$$\bar{\gamma}(x, r) = \gamma(x, r) \exp\left(-j\frac{4\pi}{\lambda}r\right) \quad (25)$$

and:

$$G(\xi, \eta, r) = \iint dx' dr' g(x - x', r - r', r) \exp[-j\xi(x' - x)] \exp[-j\eta(r' - r)] \quad (26)$$

is the SAR system TF, that is, the Fourier Transform (FT) of the system impulse response $g(\cdot)$.

Let us note that, when the r -dependence of the function $g(\cdot)$ can be neglected, eq.(20) reduces to the two-dimensional (2D) convolution $\bar{\gamma}(x', r') \otimes g(x', r')$, and, accordingly, the simplified expression for eq. (26):

$$\begin{aligned} H(\xi, \eta) &= \iint dx dr \gamma(x, r) \exp(-j\xi x) \exp(-j\eta r) G(\xi, \eta) \\ &= \bar{\Gamma}(\xi, \eta) G(\xi, \eta) \end{aligned} \quad (27)$$

is obtained. In eq.(27) $\bar{\Gamma}(\cdot)$ is the FT of $\bar{\gamma}(\cdot)$. Unfortunately, the simplification leading to eq.(27) is not allowed in general, and the direct r -dependence of the function $g(\cdot)$ requires special care when SAR data processing operations are implemented. Use of stationary phase method [2] allows calculating the integral (26) as follows (see Appendix I):

$$\begin{aligned} G(\xi, \eta, r) &= \text{rect}\left[\frac{\eta}{\Omega_r}\right] \exp\left[j\frac{\eta^2}{4b}\right] \\ &\cdot \text{rect}\left[\frac{\xi}{\Omega_x}\right] \exp\left[-j\left(\sqrt{\bar{\eta}^2 - \xi^2} - \bar{\eta}\right)r\right] \end{aligned} \quad (28)$$

where:

$$b = \frac{4\pi}{\lambda} \frac{\Delta f}{c\tau} \quad (29)$$

$$\Omega_x = 2\pi \frac{2}{L} \quad (30)$$

$$\Omega_r = bc\tau = 2\pi \frac{2\Delta f}{c} \quad (31)$$

$$\bar{\eta} = \eta + \frac{4\pi}{\lambda} \quad (32)$$

f being the carrier frequency; other symbols used in eqs.(29)-(32) have already been defined in the previous Section and, in any case, they are collected in Table of Symbols.

We note that nonessential amplitude factors have been neglected in (28).

Some considerations on the SAR TF of eq.(28) are now in order.

First of all we observe that $G(\cdot)$ is a function band limited, Ω_r and Ω_x being the range and the azimuth spatial bandwidth (rad/m), respectively. As far as azimuth bandwidth is concerned, we observe that Ω_x when converted in Hz (via the multiplication by the converting factor $v/2\pi$, v being the sensor velocity) is equal to $2v/L$, which is often interpreted as Doppler bandwidth. Turning to the range bandwidth, we note that Ω_r when converted in Hz (via

the multiplication by the converting factor $c/4\pi$, c being the speed of the light) is equal, see eq.(31), to Δf , i.e., to the transmitted pulse bandwidth. Furthermore, examination of eq.(28) shows the presence of a chirp along the η -direction: it is the FT of the transmitted chirp, see eq. (101) in Appendix I; accordingly, the pulse compression step, introduced in the previous Section, is equivalent to the multiplication, carried out in the spectral domain, of (28) by the following term:

$$RF(\eta) = \text{rect}\left[\frac{\eta}{\Omega_r}\right] \exp\left[-j\frac{\eta^2}{4b}\right] \quad (33)$$

which is the FT of eq.(14).

For what concerns the remaining exponential term of eq.(28), we can consider the following approximation:

$$\sqrt{\bar{\eta}^2 - \xi^2} - \bar{\eta} = \frac{4\pi}{\lambda} \left(1 + \frac{\lambda\eta}{4\pi}\right) \sqrt{1 - \left[\frac{\xi}{\frac{4\pi}{\lambda} \left(1 + \frac{\lambda\eta}{4\pi}\right)}\right]^2} - \bar{\eta} \approx -\frac{1}{2} \frac{\lambda}{4\pi} \frac{\xi^2}{\left(1 + \frac{\lambda\eta}{4\pi}\right)} \quad (34)$$

since $|\xi| \leq \frac{2\pi}{L} \ll \frac{2\pi}{\lambda}$, see eq.(30). Accordingly, we can approximate eq.(28) as follows:

$$G(\xi, \eta, r) \approx \text{rect}\left[\frac{\eta}{\Omega_r}\right] \exp\left[j\frac{\eta^2}{4b}\right] \text{rect}\left[\frac{\xi}{\Omega_x}\right] \exp\left[j\frac{1}{2} \frac{\lambda r}{4\pi} \frac{\xi^2}{\left(1 + \frac{\lambda\eta}{4\pi}\right)}\right] \quad (35)$$

According to the approximated, more manageable expression (35), introduced here only for the sake of clearness, we note that eq.(35) cannot be factorized in the product of two terms, each one depending on ξ and η only. This factorization requires an additional approximation: to neglect the coupling factor $\lambda\eta/4\pi$ (see condition (107) in Appendix I) which leads to:

$$G(\xi, \eta, r) \approx \text{rect}\left[\frac{\eta}{\Omega_r}\right] \exp\left[j\frac{\eta^2}{4b}\right] \text{rect}\left[\frac{\xi}{\Omega_x}\right] \exp\left[j\frac{\lambda r}{4\pi} \frac{\xi^2}{2}\right] \quad (36)$$

In this case the TF becomes the product of the spectra of two FM chirps. As noted in the previous Section, the movement of the SAR sensor “generates” approximately a chirp along the azimuth direction, see eq.(18), the FT of which is the spectral ξ -dependent chirp of eq.(36), which, interestingly, exhibits an r -dependent rate.

The impact of the coupling term $\lambda\eta/4\pi$ on the SAR image properties is addressed in the next Section.

1.3 SAR focusing

In this Section we focus our attention on the possibility to improve the geometric resolution (10) and (16) of the received raw data $h(x',r')$. We first refer to the signal backscattered by a (unitary) point target, in order to explain the rationale of the *SAR focusing procedure*, also referred to as *SAR processing procedure*. Then, we move to analyze extended scenes.

1.3.1 Point target analysis.

Let us refer to the raw data collected in the presence of a unitary point target $P \equiv P(x_0, r_0)$; by letting $\gamma(x, r) = \gamma(x_0, r_0) \delta(x - x_0) \cdot \delta(r - r_0)$ in eq.(20) we obtain:

$$\begin{aligned} h(x', r') &= [\gamma(x_0, r_0) \delta(x' - x_0) \cdot \delta(r' - r_0)] \otimes \left[\exp\left(-j \frac{4\pi}{\lambda} r\right) g(x', r', r) \right] \\ &= \gamma(x_0, r_0) \exp\left(-j \frac{4\pi}{\lambda} r_0\right) g(x' - x_0, r' - r_0, r_0) \end{aligned} \quad (37)$$

where the symbol \otimes represents the two dimensional convolution operation with respect to the variables (x', r') . Obviously, eq. (37) coincides with eq.(13), provided that (x, r) are substituted by (x_0, r_0) . In this case, according to eq.(24), we have:

$$\begin{aligned} H(\xi, \eta) &= \gamma(x_0, r_0) \exp\left(-j \frac{4\pi}{\lambda} r_0\right) \times \\ &\quad \times \iint dx' dr' g(x_0 - x', r_0 - r', r_0) \exp(-j\xi x') \exp(-j\eta r') = \\ &= \gamma(x_0, r_0) \exp\left(-j \frac{4\pi}{\lambda} r_0\right) G(\xi, \eta, r_0) \exp[-j(\xi x_0 + \eta r_0)] = \\ &= \gamma(x_0, r_0) \exp\left(-j \frac{4\pi}{\lambda} r_0\right) \text{rect}\left[\frac{\eta}{\Omega_r}\right] \text{rect}\left[\frac{\xi}{\Omega_x}\right] \exp\left[j \frac{\eta^2}{4b}\right] \\ &\quad \cdot \exp\left[-j\left(\sqrt{\bar{\eta}^2 - \xi^2} - \bar{\eta}\right) r_0\right] \exp[-j(\xi x_0 + \eta r_0)] \end{aligned} \quad (38)$$

The main goal of the SAR processor is the appropriate combination of all the received contributions backscattered by each target to achieve the best resolutions. Examination of eq.(37) shows that this operation consists of a

deconvolution step applied to $h(x',r')$ to compensate for the convolution factor $g(x',r',r_0)$ and recover the target contribution. This operation can be easily and efficiently implemented in the Fourier domain via the multiplication of the signal spectrum $H(\xi, \eta)$ by the function $G^*(\xi, \eta, r_0)$, with '*' denoting the conjugate operator. This leads to the so-called *focused* SAR image of the point target:

$$\begin{aligned} \hat{\gamma}(x',r') &= \gamma(x_0, r_0) \exp\left(-j \frac{4\pi}{\lambda} r_0\right) \times \\ &\times \iint d\xi d\eta H(\xi, \eta) G^*(\xi, \eta, r_0) \exp[j\xi(x' - x_0)] \exp[j\eta(r' - r_0)] \\ &= \gamma(x_0, r_0) \exp\left(-j \frac{4\pi}{\lambda} r_0\right) \times \\ &\times \iint d\xi d\eta \operatorname{rect}\left[\frac{\eta}{\Omega_r}\right] \operatorname{rect}\left[\frac{\xi}{\Omega_x}\right] \exp[j\xi(x' - x_0)] \exp[j\eta(r' - r_0)] \end{aligned} \quad (39)$$

where nonessential multiplicative factors have been neglected. Equation (39) easily leads, but for amplitude factors, to:

$$\hat{\gamma}(x',r') = \gamma(x_0, r_0) \exp\left(-j \frac{4\pi}{\lambda} r_0\right) \operatorname{sinc}\left[\frac{\Omega_x}{2}(x' - x_0)\right] \operatorname{sinc}\left[\frac{\Omega_r}{2}(r' - r_0)\right] \quad (40)$$

where the *sinc*(·) function is defined as follows:

$$\operatorname{sinc}(x) = \frac{\sin(x)}{x}. \quad (41)$$

Equation (40), commonly referred to as SAR image Point Spread Function (PSF), represents the two-dimensional *focused SAR image* $\hat{\gamma}(x',r')$, obtained by applying a *processing procedure* to the raw data $h(x',r')$ of eq.(37) collected in the presence of an isolated target immersed in a completely absorbing scene

Some considerations on the proprieties of the focused SAR image PSF eq.(40) are now in order.

We can note a significant improvement of the geometric resolutions with respect to those achievable by the *unprocessed*, i.e., *unfocused*, raw data $h(x',r')$ (see eqs.(10), (16)). To better clarify this key point, we first focus our attention on the range resolution of $\hat{\gamma}(x',r')$.

The distance between the -3 decibel (dB) points of the r' -dependent part of the PSF of eq.(40) is given by:

$$\Delta r = \frac{2\pi}{\Omega_r} = \frac{c}{2\Delta f} = \frac{\pi c}{\alpha\tau}, \quad (42)$$

where use of eqs.(31) and (12), respectively, has been made in two equalities. Equation (42) is the effective range dimension of the imaged target, thus representing the range resolution of the focused SAR image. By comparing eq.(42) with eq. (10) we obtain:

$$\frac{\Delta r}{\Delta r_{raw}} = \frac{2\pi}{\alpha\tau^2} = \frac{1}{\Delta f\tau}; \quad (43)$$

accordingly, use of chirp rate large enough to have $\alpha\tau^2 \gg 2\pi$, which is the case of all the SAR systems (see also Appendix I), allows significant improvement of the range resolution of the focused SAR image with respect to that of the unfocused raw data $h(x',r')$. By applying eq.(43) to ERS sensor parameters we obtain $\Delta r/\Delta r_{raw} = 1/570$ (see again Appendix I), and an improvement of the geometric resolution of two-three orders of magnitude is thus achieved in the range direction.

Azimuth resolution of the processed SAR image is now addressed. The distance between the -3 decibel (dB) points of the x' -dependent part of the PSF of eq.(40) is given by:

$$\Delta x = \frac{2\pi}{\Omega_x} = \frac{L}{2} \quad (44)$$

where use of eq.(30) has been made in the last equality. Equation (44) is the effective azimuth dimension of the imaged target, thus representing the azimuth resolution of the processed SAR image $\hat{\gamma}(x',r')$; in this case, differently from the raw data azimuth resolution of eq.(16), it is independent of the target-to-sensor distance, and depends only on the (effective) antenna dimension along the azimuth direction. By comparing eq.(44) with eq.(16), we obtain:

$$\frac{\Delta x}{\Delta x_{raw}} = \frac{L}{2X} = \frac{L^2}{2\lambda r}; \quad (45)$$

accordingly, the improvement of azimuth resolution of $\hat{\gamma}(x',r')$, with respect to that of $h(x',r')$, depends on the ratio between the physical (L) and the synthetic (X) antenna dimension. For all the SAR systems the condition $2\lambda r/L^2 = 2X/L \gg 1$ is well satisfied. By applying eq.(45) to ERS sensor parameters we obtain $\Delta x/\Delta x_{raw} = 1/891$ (see again Appendix I), and an improvement of the geometric resolution of two-three orders of magnitude is

thus achieved also in the azimuth direction. Moreover, we note that, according to eq.(44), Δx can be rendered smaller by adopting airborne sensors, which allow using smaller antenna dimensions.

Let us now give a more detailed interpretation of eqs.(39), (40). Letting $G(\xi, \eta, r_0) = G_1^*(\eta) \cdot G_2^*(\xi, \eta, r_0)$, with:

$$G_1(\eta) = \text{rect} \left[\frac{\eta}{\Omega_r} \right] \exp \left[j \frac{\eta^2}{4b} \right] \quad (46)$$

and:

$$G_2(\xi, \eta, r_0) = \text{rect} \left[\frac{\eta}{\Omega_r} \right] \text{rect} \left[\frac{\xi}{\Omega_x} \right] \exp \left[-j \left(\sqrt{\eta^2 - \xi^2} - \eta \right) r_0 \right] \quad (47)$$

we want to decouple the effect of $G_1^*(\cdot)$ and $G_2^*(\cdot)$ on the image formation.

Consider first the multiplication step involving the function $G_1^*(\eta)$. Its counterpart in the r' -domain is the convolution operation of SAR data with the $rf(\cdot)$ of eq.(14), which, as noted in the previous Section, is the inverse FT of $G_1^*(\eta) = RF(\eta)$, see eq.(33). This convolution, as noted above, is referred to as *range compression* and easily leads to:

$$h_{rc}(x', r') = \text{sinc} \left[\frac{\Omega_r}{2} [r' - r_0 - \Delta R(x' - x_0, r_0)] \right] \exp \left(-j \frac{4\pi}{\lambda} r_0 \right) \cdot \text{rect} \left[\frac{x' - x_0}{X} \right] \exp \left(-j \frac{4\pi}{\lambda} \Delta R(x' - x_0, r_0) \right) \quad (48)$$

where ΔR is given by eq.(9), provided that r is substituted by r_0 . This range compressed signal is spread along the curve:

$$r' - r_0 = \Delta R \approx \frac{(x' - x_0)^2}{2r_0}, \quad (49)$$

where use of eq.(17) has been made in the last approximation. This curve represents the sensor-to-target distance, and the above mentioned spreading effect is referred to as *Range Cell Migration (RCM)*.

According to (49), the last complex exponential factor in eq.(48) is approximately a chirp, the rate of which is related to the target range location r_0 . Accordingly, the factor $G_2^*(\cdot)$ plays a double role: it rectifies the range compressed signal in eq.(48) on a rectilinear path:

$$\text{sinc} \left[\frac{\Omega_r}{2} [r' - r_0 - \Delta R(x' - x_0, r_0)] \right] \rightarrow \text{sinc} \left[\frac{\Omega_r}{2} [r' - r_0] \right] \quad (50)$$

and coherently combines the azimuth chirp contributions:

$$\text{rect}\left[\frac{x' - x_0}{X}\right] \exp\left(-j \frac{4\pi}{\lambda} \Delta R(x' - x_0, r_0)\right) \rightarrow \text{sinc}\left[\frac{\Omega_x}{2}(x' - x_0)\right] \quad (51)$$

The result of the operation described in eq.(50) is referred to as *Range Cell Migration Compensation*, while the one in eq.(51) as *Azimuth Compression*.

Results provided by eqs.(48), (50), (51) are pictorially shown in Fig. 5. As already discussed in connection with eq.(35), the RCM effect is accounted for by the term $\lambda/4\pi$ that couples the ξ and η variables in the approximated expression of eq. (35) for $G(\cdot)$. It can be interesting to additionally decouple, in eq. (35) the two effects accounted for by the compensation operations in eqs.(50) and (51). This result is obtained by means of a series expansion of the coupling term in the approximated expression of eq. (35), which leads to:

$$G_2(\xi, \eta, r_0) \approx \text{rect}\left[\frac{\eta}{\Omega_r}\right] \text{rect}\left[\frac{\xi}{\Omega_x}\right] \exp\left[j \frac{\xi^2}{2} \frac{\lambda r_0}{4\pi}\right] \exp\left[-j \frac{\xi^2}{2} \frac{\lambda r_0}{4\pi} \frac{\eta \lambda}{4\pi}\right]. \quad (52)$$

The first exponential term accounts only for the azimuth chirp compression, while the second one accounts for the range cell migration compensation in frequency domain. The latter maintains coupling of ξ and η variables, even in this approximated version.

1.3.2 Extended scene analysis: range invariant SAR focusing.

Let us extend the point target analysis of the previous sub-Section to the case of extended illuminated area.

As noted in the previous sub-Section, a two-dimensional multiplication, performed in the Transformed Fourier Domain, allows the generation of high resolution SAR image of a generic target located in (x_0, r_0) . However, we must note that use of a filter tailored to the range coordinate r_0 of the considered target was necessary, see eq.(39), to carry out precise focusing of such a target. This is due to the fact that, as discussed in Sect. 1.2, the SAR Transfer Function $G(\cdot)$, see eq.(28), depends on the range coordinate of the illuminated target. Accordingly, if we move to the extended scene case, a range space-variant filtering tailored to each range coordinate would be necessary to achieve perfect focusing. This would be highly time consuming,

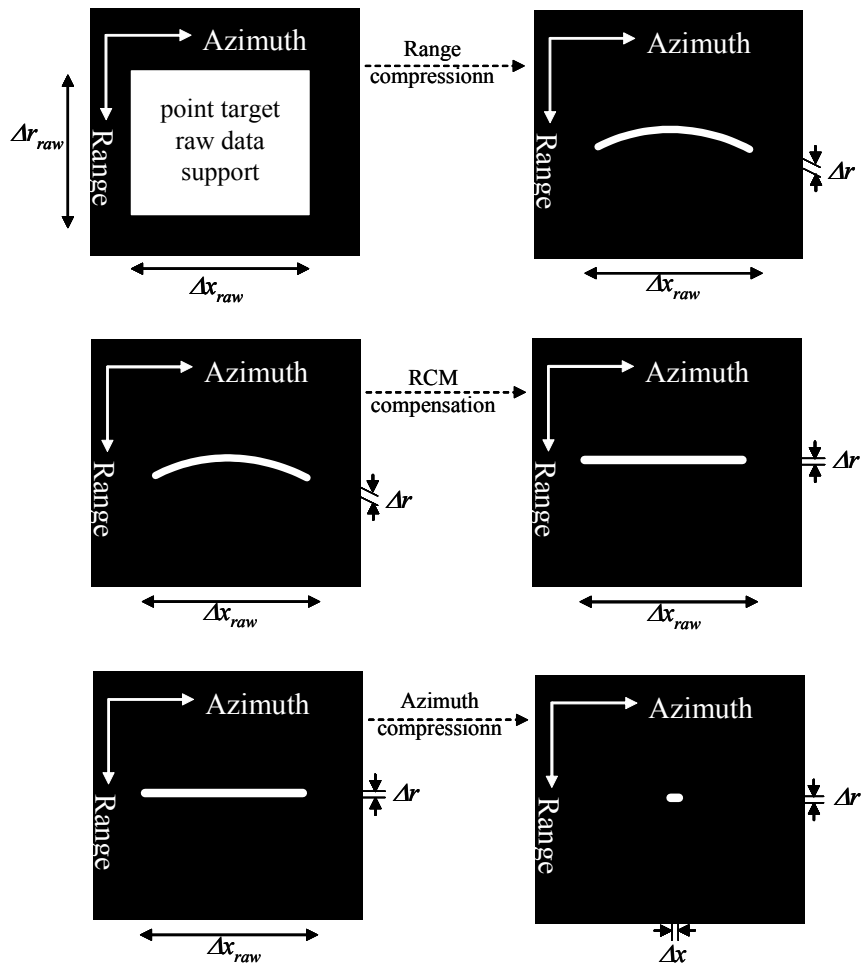


Figure 5 SAR focusing of a point target.

and thus not desirable, so that exploitation of more efficient focusing scheme has been investigated in the last years.

The simplest and most efficient processing scheme is based on the following approximation:

$$G(\xi, \eta, r) \approx G(\xi, \eta, r_0) = G_0(\xi, \eta) \quad (53)$$

where r_0 is the range coordinate of the scene center. The approximation in (53) leads to the approximated expression of the raw data spectrum already introduced in Sect. 1.2:

$$H(\xi, \eta) \approx \bar{\Gamma}(\xi, \eta) G_0(\xi, \eta), \quad (54)$$

thus suggesting the following space invariant filtering:

$$\hat{\Gamma}(\xi, \eta) = H(\xi, \eta) G_0^*(\xi, \eta) \approx \bar{\Gamma}(\xi, \eta) G_0(\xi, \eta) G_0^*(\xi, \eta) \quad (55)$$

carried out in the two dimensional Fourier Domain. The spectral multiplication of eq.(56) allows efficient focusing of the SAR image along the scheme depicted in Fig.6.

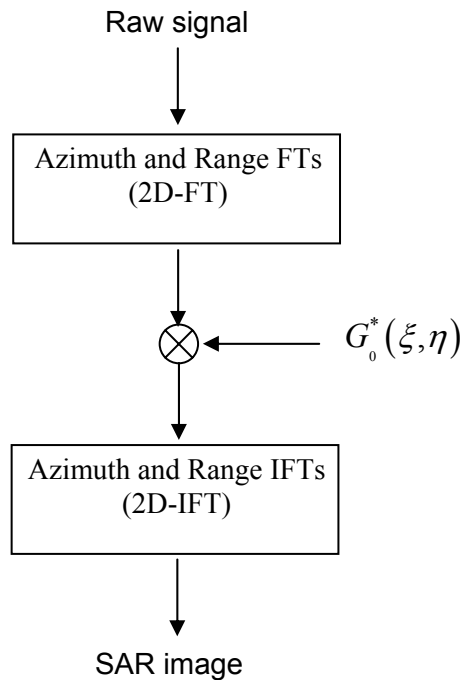


Figure 6 Narrow focus SAR processing block diagram.

Note that the operation implemented by such a processing scheme can be carried out directly in time domain, since it is equivalent to a deconvolution step applied to $h(x',r')$. However, the system impulse response generally extends for several hundreds points in both azimuth and range directions; typical dimensions of the raw data set are very large too (thousands complex samples for each direction). Hence, it is convenient to carry out the deconvolution operation in the Fourier Domain due to the availability of Fast Fourier Transform (FFT) codes.

A final comment on the processing approach depicted in Fig. 6 is now in order.

The key point of the such a procedure is represented by knowledge of the TF obtained in Sect. 1.3, eq.(28) by assuming $r=r_0$. For this reason we refer to this processing procedure as the *narrow focus* code, as only the central part of the scene, $r=r_0$, is perfectly focused. A quantitative analysis of the aberrations caused by the r -dependence simplification in eq.(53) is addressed in [1].

1.3.3 Extended scene analysis: range variant SAR focusing.

As discussed above, the processing scheme in Fig. 6 does not account for range dependence of the TF: only the central part of the image, around $r \approx r_0$ is *fully focused*. This is not acceptable in many cases and ways to obtain a fully focused image are desirable. This implies moving from a *narrow focus* to a *wide focus* processor.

Let us start from the expression of the spectrum of SAR raw data, see eqs.(24) and (28):

$$H(\xi, \eta) = \iint dx dr \bar{\gamma}(x, r) \text{rect}\left[\frac{\eta}{\Omega_r}\right] \text{rect}\left[\frac{\xi}{\Omega_x}\right] \times \exp[-jK(\xi, \eta)r] \exp(-j\xi x) \exp(-j\eta r) \quad (57)$$

where, according to eq. (28),

$$K(\xi, \eta) = \sqrt{\bar{\eta}^2 - \xi^2} - \bar{\eta}. \quad (58)$$

In eq.(57), the r -dependence of the SAR TF $G(\cdot)$ is clearly highlighted: it is evident that only the argument of the first exponential term in (57) depends on r ; moreover, such a dependence is recognized to be linear. In order to obtain a more manageable expression of the signal, we let $\bar{r} = r - r_0$ in eq.(57), thus obtaining:

$$H_1(\xi, \eta) = G_0(\xi, \eta) \times \iint dx d\bar{r} \bar{\gamma}_1(x, \bar{r}) \exp[-j(\eta + K(\xi, \eta))\bar{r}] \exp(-j\xi x) \quad (59)$$

where, as usual, $G_0(\xi, \eta) = G(\xi, \eta, r_0)$, and

$$\begin{cases} H_1(\xi, \eta) = H(\xi, \eta) \exp(j\eta r_0) = FT[h(x', r' + r_0)] \\ \bar{\gamma}_1(x, \bar{r}) = \bar{\gamma}(x, \bar{r} + r_0) \end{cases} \quad (60)$$

Due to the introduced change of variables, the range center of the image $h_r(\cdot)$ is now located at $r'=0$. Advantages related to this variable change will be clarified at the end of the Section.

Equation (59) clearly leads to the following:

$$H_1(\xi, \eta) = G_0(\xi, \eta) \cdot \bar{\Gamma}_1(\xi, \eta + K(\xi, \eta)) \quad (61)$$

In eq.(61) $\bar{\Gamma}_1(\xi, \eta + K(\xi, \eta))$ is the FT of $\bar{\gamma}_1(\cdot)$ computed over the new grid $[\xi, \eta + K(\xi, \eta)]$, instead of the conventional one $[\xi, \eta]$. It is evident that the r -dependence of the SAR TF $G(\cdot)$ generates a nonlinear mapping of the range frequencies of the spectrum of $\bar{\gamma}(\cdot)$, often referred to as *Stolt mapping* in the literature [3], [4]. Accordingly, it is possible to account for the r -dependence of SAR TF by applying a *counter-deformation* that allows the correct generation of $\bar{\Gamma}_1(\xi, \eta)$

$$\bar{\Gamma}_1(\xi, \eta + K(\xi, \eta)) \rightarrow \bar{\Gamma}_1(\xi, \eta) \quad (62)$$

The operation of eq.(62) requires a ξ -dependent shift of the $\bar{\Gamma}_1(\cdot)$ spectrum in the η direction, according to the function $K(\xi, \eta)$.

It is now evident, see eqs.(61) and (62), that wide focus SAR processor, the block diagram of which is depicted in Fig.7, consists of a multiplication, carried out in the two dimensional transformed domain, followed by a spectral complex re-sampling [5].

Some considerations on the processing approach of Fig. 7, referred to as Ω - K algorithm in the literature, are now in order.

First of all, we note that the result of the filtering operation of eq.(61) is band limited, according to eqs.(53), (28). Accordingly, the final SAR image spectrum, after the counter-deformation step of eq.(62) is given by:

$$\hat{\Gamma}_1(\xi, \eta) = \Gamma_1(\xi, \eta) \text{rect}\left[\frac{\xi}{\Omega_x}\right] \text{rect}\left[\frac{\eta}{\Omega_r}\right] \quad (63)$$

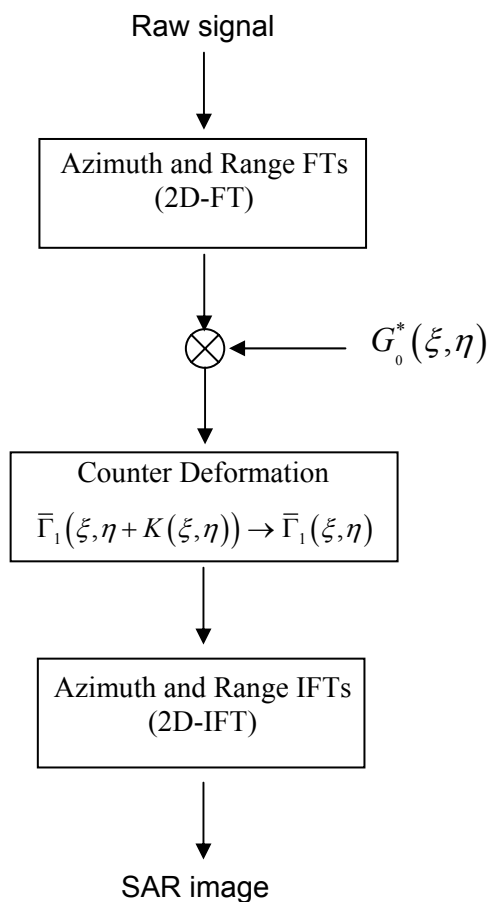


Figure 7 Wide focus SAR processing block diagram based on Ω - K approach.

which leads, after proper range-shift and subsequent 2D inverse Fourier Transform, to the following focused SAR image:

$$\hat{\gamma}(x', r') \approx \iint dx dr \bar{\gamma}(x, r) \text{sinc}\left[\frac{\Omega_r}{2}(r' - r)\right] \text{sinc}\left[\frac{\Omega_r}{2}(x' - x)\right], \quad (64)$$

the geometrical resolutions of which are coincident with those of eqs.(42) and (44).

Furthermore, we note that the spectral re-sampling operation of eq.(62) is a relatively time consuming step that must be properly carried out to avoid artifacts generated by the truncated interpolation kernels. Such a limitation is overcome by other efficient algorithms developed in the last years[6]-[11], the basic rationale of which is addressed in the following.

Let us refer to eq.(59) and consider the following approximation:

$$\exp[-j(K(\xi, \eta) + \eta)\bar{r}] \approx \exp[-j(\mu(\xi) + \Omega(\xi) \cdot \eta)\bar{r}] \quad (65)$$

where a series expansion along η of $K(\cdot)\bar{r}$ has been considered, so that:

$$\mu(\xi) = \sqrt{\left(\frac{4\pi}{\lambda}\right)^2 - \xi^2} - \frac{4\pi}{\lambda} \quad (66)$$

$$\Omega(\xi) = \frac{1}{\sqrt{1 - \left(\frac{\xi\lambda}{4\pi}\right)^2}} \quad (67)$$

Some considerations on the approximation in (65) are now in order.

First of all we observe that, since in all the realistic cases $\bar{r} < r$, the approximation (65) takes benefit by the variable change considered in eq. (59), which allows the presence of \bar{r} , instead of r , in the exponential term considered in eq.(65).

Furthermore, according to eq.(65), we can rearrange eq.(61) as follows:

$$\begin{aligned} H_1(\xi, \eta) &= H(\xi, \eta) \exp[j\eta r_0] = \\ &= G_0(\xi, \eta) \iint dx d\bar{r} \bar{\gamma}_1(x, \bar{r}) \exp[-j(\mu(\xi) + \Omega(\xi) \cdot \eta)\bar{r}] \exp(-j\xi x) \end{aligned} \quad (68)$$

Equation (68) suggests the following four-step processing strategy, the block diagram of which is depicted in Fig. 8.

As first step we compute the 2D spectrum $H_1(\xi, \eta)$ of the shifted SAR raw signal and remove its r -invariant TF component $G_0(\cdot)$ by multiplying $H_1(\cdot)$ by $G_0^*(\cdot)$:

$$H'(\xi, \eta) = H(\xi, \eta) \exp[j\eta r_0] \cdot G_0^*(\xi, \eta) \quad (69)$$

The obtained data $H'(\xi, \eta)$ are now given by:

$$\begin{aligned} H'(\xi, \eta) &= \iint dx d\bar{r} \bar{\gamma}(x, \bar{r} + r_0) \text{rect}\left[\frac{\eta}{\Omega_r}\right] \text{rect}\left[\frac{\xi}{\Omega_x}\right] \times \\ &\quad \times \exp[-j(\mu(\xi) + \Omega(\xi) \cdot \eta)\bar{r}] \exp(-j\xi x) \end{aligned} \quad (70)$$

where use of eq.(60) has been done. As a matter of fact, we observe that the operation accomplished in (69) corresponds to focusing the data in the range direction, and to fully focusing in azimuth all the points placed at the middle

range, i.e., $r=r_0$, including, for these targets, the compensation of the range cell migration phenomenon. The residual terms $\mu(\xi)\bar{r}$ and $\Omega(\xi)\bar{r}$ account for the so called *focus depth effect* [1] and *range-variant range cell migration* (RVRCM) effect [10], respectively.

The second processing step, aimed at compensating the RVRCM effect, consists of an inverse *range-scaled* FT, hereafter referred to as ISCFT, which includes the scaling term $\Omega(\xi)$ in its kernel:

$$H'(\xi, r') = \int d[\Omega(\xi)\eta] \exp[j\Omega(\xi)\eta r'] H'(\xi, \eta) \quad (71)$$

This operation may be carried out via known efficient approaches, such as chirp scaling [8] or chirp z-transform [9], [10], and leads, in the (ξ, r') domain, to the following expression $H'(\xi, r')$ of the signal:

$$\begin{aligned} H'(\xi, r') = & \iint dx d\bar{r} \bar{\gamma}(x, \bar{r} + r_0) \exp[-j\mu(\xi)\bar{r}] \exp(-j\xi x) \text{rect}\left[\frac{\xi}{\Omega_x}\right] \times \\ & \times \int d[\Omega(\xi)\eta] \text{rect}\left[\frac{\eta}{\Omega_r}\right] \exp[j\Omega(\xi)\eta(r' - \bar{r})] \approx \\ & \text{rect}\left[\frac{\xi}{\Omega_x}\right] \iint dx d\bar{r} \bar{\gamma}(x, \bar{r} + r_0) \exp[-j\mu(\xi)\bar{r}] \exp(-j\xi x) \text{sinc}\left[\frac{\Omega_r}{2}(r' - \bar{r})\right] \end{aligned} \quad (72)$$

By changing the variable of integration, in the integral (72), we can rearrange eq.(72) as follows:

$$\begin{aligned} H'(\xi, r') \approx & \text{rect}\left[\frac{\xi}{\Omega_x}\right] \iint dx dr \bar{\gamma}(x, r) \text{sinc}\left[\frac{\Omega_r}{2}(r' - (r - r_0))\right] \times \\ & \times \exp[-j\mu(\xi) \cdot (r - r_0)] \exp(-j\xi x) \end{aligned} \quad (73)$$

The third step of the processing procedure is aimed at compensating the focus depth effect, by letting $r - r_0 \approx r'$ in the first exponential factor: this is possible due to the fact that now the data are range compressed and do not show RCM effect, see the argument of the $\text{sinc}(\cdot)$ function in (73). Accordingly, the multiplication of eq.(73) by $\exp(j\mu(\xi) r')$, followed by a range shift of the data, that is $r' \rightarrow r' + r_0$, leads to the following expression of the data:

$$H''(\xi, r') \approx \text{rect}\left[\frac{\xi}{\Omega_x}\right] \iint dx dr \bar{\gamma}(x, r) \text{sinc}\left[\frac{\Omega_r}{2}(r' - r)\right] \exp(-j\xi x). \quad (74)$$

Accordingly, the fourth step of the processing procedure consists of a final standard inverse FT in the azimuth direction, leading to the SAR focused image:

$$\hat{\gamma}(x', r') \approx \iint dx dr \bar{\gamma}(x, r) \text{sinc}\left[\frac{\Omega_r}{2}(r' - r)\right] \text{sinc}\left[\frac{\Omega_r}{2}(x' - x)\right] \quad (75)$$

The presented approach, similarly to Ω - K algorithm of Fig.7, is based on the knowledge of the SAR TF obtained in Sect. 1.3. However, differently from the Ω - K algorithm, where the only approximation in the expression of the SAR TF is due to the use of the stationary phase method, see Sect.1.2, in this case an additional approximation, see eq.(65), is done, aimed at improving the computational efficiency of the processor.

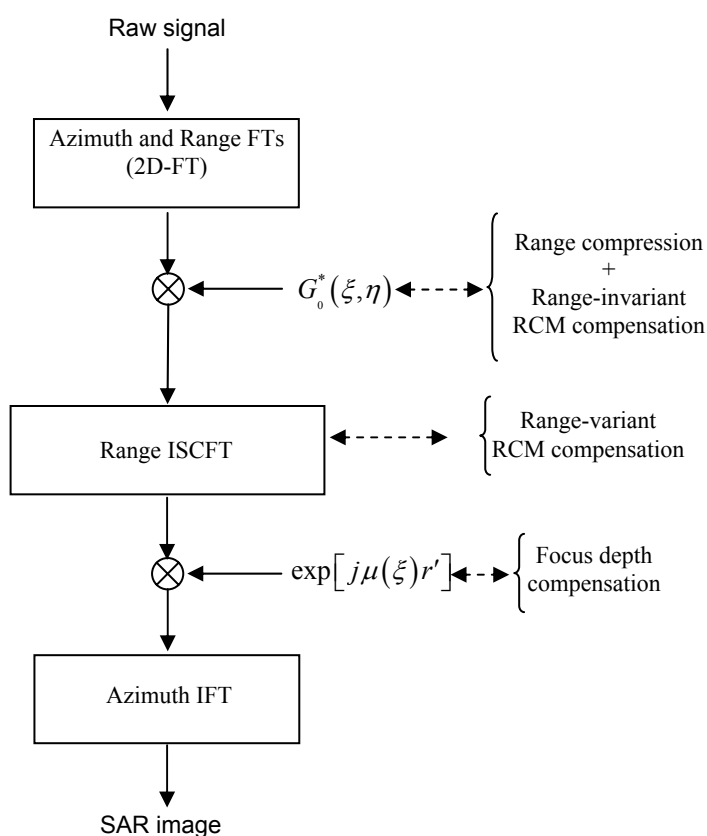


Figure 8 Wide focus SAR processing block diagram based on ISCFT algorithm.

1.4 SAR interferometry

According to the analysis of Sect. 1.3., focused SAR image, obtained after proper processing procedure implementation, allows us measuring (with finite resolution, see eqs.(75), (42) and (44)) both azimuth and range of the target. However, it is evident that knowledge of the target range coordinate, say r , is not sufficient for uniquely determine location of the target and therefore its height above the reference plane. This is clearly shown in Fig. 9 (left), in which the SAR geometry in the plane orthogonal to the azimuth direction is depicted: all the targets within the range beam and located on an equidistance curve are imaged at the same range position $r' \approx r$. In other words, the two dimensional focused SAR image does not allow accessing to the third dimension, i.e., \mathcal{G} in the usual cylindrical reference system introduced in Sect. 1.1, of the imaged target.

Such a limitation can be overcome if we consider a second image obtained with a sensor which observes the same scene from a different position (see Fig.9, right). The spacing l between the two sensors is usually referred to as *baseline*; the angle σ between the vector connecting the first sensor to the second one and the horizontal direction is referred to as *tilt angle*, see again Fig. 9b.

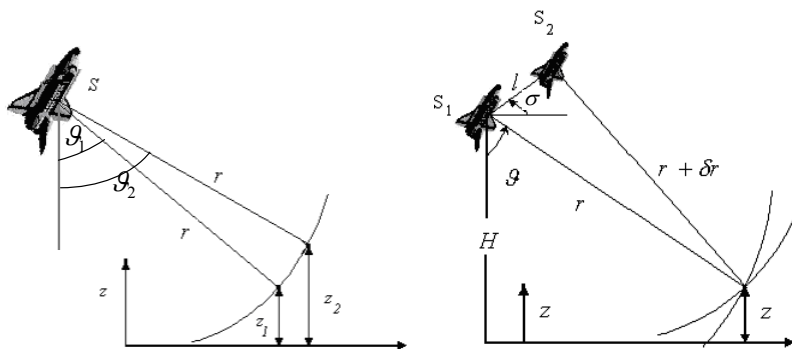


Figure 9 Single-imaging (left) and Stereo-imaging (right) sensor. Geometry in the plane orthogonal to the flight direction.

The two images can be either obtained by means of a single bistatic system with two (one active and one passive) imaging sensors, or with two repeat passes of a single (active) imaging sensor system. In this latter case the properties of the scene relevant to the sensing system must remain unchanged within the time frame of the two passes.

By using the additional information represented by the range of the target from the second system, the ambiguity existing on target location is

completely solved. As matter of fact, only one point exists which is located at distance r from the first system and $r + \delta r$ from the second one.

This is equivalent to say that knowledge of \mathcal{G} comes from knowledge of both r and $r + \delta r$. To better clarify this point, we observe that, see Fig. 9:

$$(r + \delta r)^2 = r^2 + l^2 - 2lr \sin(\mathcal{G} - \sigma). \quad (76)$$

From eq.(76) we get:

$$\delta r = \sqrt{r^2 + l^2 - 2lr \sin(\mathcal{G} - \sigma)} - r \approx -l \sin(\mathcal{G} - \sigma) \quad (77)$$

where the last approximation holds when baseline is small compared with the target slant range, as it is always the case; δr thus reduces to the baseline projection onto the look direction. According to the approximation in (77), knowledge of the path difference δr (and not necessary of the distances r and $r + \delta r$) allows us calculating the third dimension \mathcal{G} of the considered target, provided that both l and σ , describing sensor positions, are known. Moreover, it is easy to show that knowledge of \mathcal{G} allows calculating the target height above the reference plane, i.e., its third dimension in a reference system different from that introduced in Sect. 1.1, by means of the following equation:

$$z = H - r \cos \mathcal{G} \quad (78)$$

where H is the master system height above the reference plane, see Fig. 9.

According to the shown analysis, we can say that knowledge, or better, measurement, of the path difference δr represents a key point to determinate heights of illuminated target by using SAR images acquired via a stereo-imaging geometry. Hence, the height measurement accuracy is limited by the error involved in the evaluation of the path difference δr . To check how this error generates a corresponding error in the height evaluation, we can write, according to (76) and (77), that:

$$\frac{\partial z}{\partial \delta r} = \frac{\partial z}{\partial \mathcal{G}} \frac{\partial \mathcal{G}}{\partial \delta r} \approx \frac{r \sin \mathcal{G}}{l \cos(\mathcal{G} - \sigma)}. \quad (79)$$

Accordingly, the height resolution depends on the parameter r/l , which is very large in all SAR systems. This implies that errors on the evaluation of δr are strongly amplified when they are transferred to height measurements. Moreover, we observe that the larger the baseline l (or better, its projection onto the direction orthogonal to the look angle) the smaller the impact of δr measurement inaccuracies on the height evaluation accuracy.

A method (*stereometry*) to calculate the path difference δr is easily derived. We consider a point in the first focused SAR image, hereafter referred to as *master*, with range coordinate* $r_m' \approx r$. Then, we *search* for it in the second focused SAR (*slave*) image. In this way we are able to evaluate its range from the second sensor, i.e., $r_s' \approx r + \delta r$. In this case, a reasonable estimate of δr measurement error is of the order of the range resolution, that is, of the order of meters. It is easy to show, by using eq.(79) for realistic SAR systems and geometries, that this error leads to a target height accuracy of the order of hundreds meters, which is not acceptable.

An alternative way to measure δr , aimed at improving the accuracy of target height evaluation, is carried out by analyzing the phase difference of the two focused images. This idea is exploited in interferometric SAR (INSAR) systems [1], [12]-[14] and briefly shown in the following.

According to the analysis of Sect. 1.3, the first focused SAR image, i.e, the master image, may be represented as follows::

$$\hat{\gamma}_1(x', r') \approx \iint dx dr \gamma(x, r) \exp\left(-j \frac{4\pi}{\lambda} r\right) \times \times \text{sinc}\left[\frac{\Omega_r}{2}(r' - r)\right] \text{sinc}\left[\frac{\Omega_x}{2}(x' - x)\right] \quad (80)$$

where use of eq.(25) in the general expression of eq.(75) has been made. Similarly, the slave image is given by:

$$\hat{\gamma}_2(x', r') \approx \iint dx dr \gamma(x, r) \exp\left(-j \frac{4\pi}{\lambda} (r + \delta r)\right) \times \times \text{sinc}\left[\frac{\Omega_r}{2}(r' - r - \delta r)\right] \text{sinc}\left[\frac{\Omega_x}{2}(x' - x)\right] \quad (81)$$

In eqs.(80) and (81) the usual cylindrical reference system, the axis of which coincides with the flight trajectory of the master antenna, is used.

For the sake of simplicity, let us assume that system bandwidths Ω_x and Ω_r are infinite. In this case the sinc(\cdot) functions in azimuth and range approach the Dirac one and we have:

$$\hat{\gamma}_1(x', r') \approx \gamma(x', r') \exp\left(-j \frac{4\pi}{\lambda} r'\right) \quad (82)$$

* Note the important difference between *unprimed* and *primed* coordinates. Unprimed coordinates refer to the points on the scene site, whereas primed coordinates refer to the image (i.e., sampled) points.

$$\hat{\gamma}_2(x', r') \approx \gamma(x', r' - \delta r') \exp\left(-j \frac{4\pi}{\lambda} r'\right) \quad (83)$$

wherein $\delta r' = \delta r(r = r')$.

From eqs.(82) and (83) it is evident the range displacement (*misalignment*) of the two images: this is direct consequence of the existing path difference. Accordingly, the first necessary step is a proper image registration[15]-[18]:

$$\hat{\gamma}_2(x', r') \rightarrow \hat{\gamma}_2(x', r' + \delta r') = \gamma(x', r') \exp\left[-j \frac{4\pi}{\lambda} (r' + \delta r')\right] \quad (84)$$

Then, the second step consists of phase extraction, which is implemented via the product between the master image and the complex conjugate of the other:

$$\varphi(x', r') = \text{Ph}\left[\hat{\gamma}_1(x', r') \hat{\gamma}_2^*(x', r' + \delta r')\right] = \frac{4\pi}{\lambda} \delta r' \quad (85)$$

where $\text{Ph}[\cdot]$ is the operator which gives the *full* phase, i.e. the phase not restricted to the $]-\pi, \pi[$ interval. We must note that complex data allow only to measure phase differences φ_m restricted in the $]-\pi, \pi[$ interval, while the total φ variation largely exceed this range in most (if not in all) of practical cases. Techniques, referred to as *phase unwrapping* in the literature [19]-[22], which allow reconstruction of the true phase (*unwrapped phase*), φ , starting from knowledge of the wrapped phase, φ_m , are then needed .

Equation (85) provides the desired interferometric phase. Accordingly, in IFSAR systems, the information on the path difference $\delta r'$ is obtained by considering the phases of the target responses in the two SAR images. In this case, according to (85), the error $\delta e_{\delta r}$, in the evaluation of the path difference δr is related to the error δe_{φ} in the measurement of the interferometric phase φ , as follows:

$$\delta e_{\delta r} = \frac{\lambda}{4\pi} \delta e_{\varphi} \quad (86)$$

Accordingly, if a phase noise standard deviation of $\pi/4$ is assumed, we get a δr measurement error of the order of a fraction of the wavelength λ , that is, of the order of centimeters or millimeters, with an improvement of two or three orders of magnitude with respect to the stereometry technique.

The IFSAR processing chain can be summarized as depicted in fig. 10:

- Generation of two SLC images via SAR processing of raw data pair relative to the same scene;
- Registration of the two SLC images, phase difference (*interferogram* or *fringes*) extraction;
- Phase unwrapping of the wrapped interferometric phase, i.e., of the interferogram.

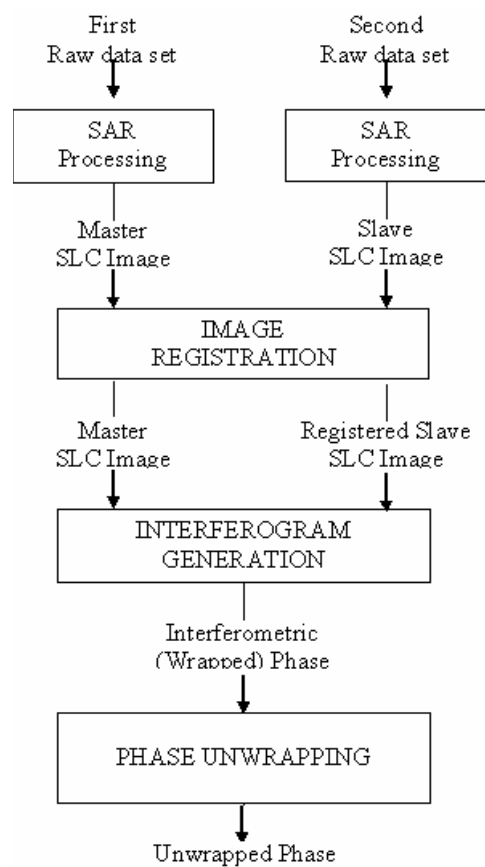


Figure10 Block diagram of the IFSAR processor.

It should be noted that the above simplified discussion does not account for inevitable noise that corrupts the fringes. In particular, it can be shown that, in the realistic hypothesis of finite system bandwidths Ω_x and Ω_r , the phase difference between two registered images is not only dependent on the

path difference δr , but it is a much more complicated issue: the interferometric exponential term is modified by multiplicative and additive factors [1], [23], [24]. These modifications can be modeled as an interferometric phase noise source and the problem is addressed in the literature as *decorrelation* between the signals received by the two antennas. Different sources of decorrelation can be categorized [1], [23], [24] and analyzed. However, such an analysis is beyond the target of this thesis, and not discussed here. For the sake of clearness, only *temporal decorrelation* is now shortly addressed.

In the case of repeat pass interferometry, temporal changes of the scene between the two time separated acquisitions make $\chi(x,r)$ time dependent: the resulting phase change is referred to as *temporal decorrelation* in the literature [1]. This is strongly dependent on the wavelength. In vegetated areas the use of lower frequencies, for instance, L- or even P-band, is preferred. On the other hand, X-band systems are suitable for getting the highest height accuracy in arid regions, see eq. (86).

1.4.1 Differential SAR interferometry.

An interesting extension of *repeat-pass* IFSAR, is a relatively new technique, referred to as Differential SAR Interferometry (DIFSAR) [25], which exploits the phase difference between SAR image pairs acquired at different times, in order to detect on the centimeter scale [26], [27] the relative displacement occurred in the illuminated surface between the different acquisitions. DIFSAR basic principles are hereafter outlined.

Let us refer to Fig. 11 where the two-passes DIFSAR geometry in the plane orthogonal to the antennas trajectories is depicted. Suppose that a ground target displacement l_d takes place in between the two passes.

As in Sect. 1.4, let us assume that system bandwidths Ω_x and Ω_r are infinite, so that the coordinates of the image points are coincident with the coordinates of the points on the scene site; i.e., primed coordinates are coincident with unprimed ones.

The target range in the slave SAR image is indicated with r'_{sd} , while r'_s is the one relevant to the same site, but with absence of surface displacements. The interferometric phase is now given by:

$$\varphi = \frac{4\pi}{\lambda} r'_{sd} - \frac{4\pi}{\lambda} r'_s \quad (87)$$

which can be rewritten as:

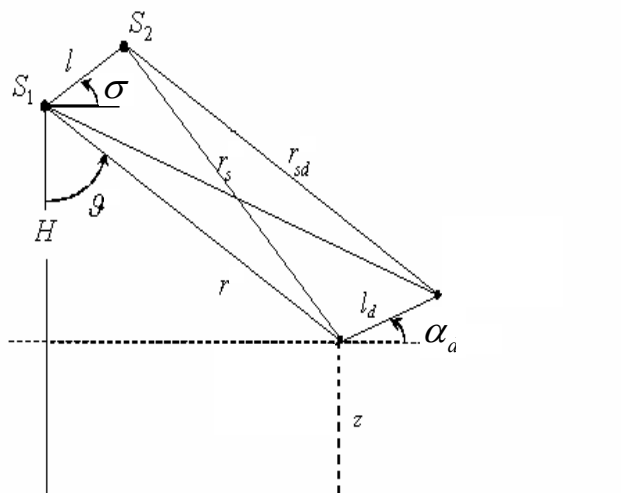


Figure 11 Relevant to the DIFSAR interferometry.

$$\varphi = \frac{4\pi}{\lambda} (r'_{sd} - r'_s + r'_s - r') = \frac{4\pi}{\lambda} (\delta r'_d + \delta r') \quad (88)$$

The contributions to the path difference due to the target displacement, $\delta r'_d$, and to the topographic height profile, $\delta r'$, have been distinguished. Note that the latter is the path difference in the absence of any ground displacement.

Let us now suppose ideally that the two passes are repeated exactly on the same orbit, i.e., $l=0$. In this case the topographic contribution is equal to zero and the interferometric phase is related only to $\delta r'_d$, as follows:

$$\frac{4\pi}{\lambda} \delta r'_d \approx \frac{4\pi}{\lambda} l_d \sin(\vartheta - \alpha_d) \quad (89)$$

where the last approximation holds when the displacement l_d is small compared with the target slant range, see Fig. 11. Equation (89) shows that $\delta r'_d$ is equal to the displacement component parallel to the look direction, usually referred to as *line of sight (los) displacement* component.

Accordingly, in this ideal situation DIFSAR technique allows measuring such a component of the displacement occurred between the different acquisitions, with an accuracy of the order of fractions of the wavelength: indeed a differential phase change of 2π is associated to a los displacement of $\lambda/2$.

Let us now move to the real situation, which requires to address the topographic contribution $\delta r'$.

The assumption $l=0$ is not realistic, so that separation between topographic and displacement contributions in eq.(88) must be carried out. To this end, we can use eqs.(77) and (78) introduced in Sect 1.4, provided that $r \rightarrow r'$ $\mathcal{G} \rightarrow \mathcal{G}'$.

Differently from Sect. 1.4, now we start from given, i.e., known, Digital Elevation Model (DEM) which gives us z . By assuming knowledge of sensor orbits, i.e., of H , l and σ , we first evaluate \mathcal{G}' via eq.(78) by knowledge of r' ; then we use this information in eq.(77) to evaluate $\delta r'$. This allows us reconstructing the so called *synthetic interferogram*, given by :

$$\varphi_t = \frac{4\pi}{\lambda} \delta r' \quad (90)$$

Accordingly, subtraction of the synthetic interferogram (90) from the interferometric phase of eq.(87) leads to:

$$\varphi_d = \frac{4\pi}{\lambda} \delta r'_d \quad (91)$$

which allows us, after proper *phase unwrapping*, measuring the component of the displacement occurred in the illuminated surface between the different acquisitions, again with an accuracy of the order of fractions of the wavelength.

The DIFSAR processing chain can be summarized as depicted in Fig. 12:

- Generation of two SLC images via SAR processing of raw data pair relative to the same scene;
- Registration of the two SLC images, phase difference (*interferogram* or *fringes*) extraction;
- Evaluation of the topographic phase term from a given (or generated) DEM (*synthetic interferogram*);
- Evaluation of the displacement phase term via subtraction of the *synthetic interferogram* from the *interferogram* generated at the second step
- Phase unwrapping of the wrapped extracted differential phase.

Additional considerations on the DIFSAR technique are now in order.

First of all, we observe that the accuracy of the surface displacement measurement is strongly related to the achievable accuracy in the generation of the synthetic interferogram of eq.(90), which, in turns, depends on the accuracy of the available DEM. To check how DEM errors generate a corresponding error in the synthetic interferogram generation, we must use

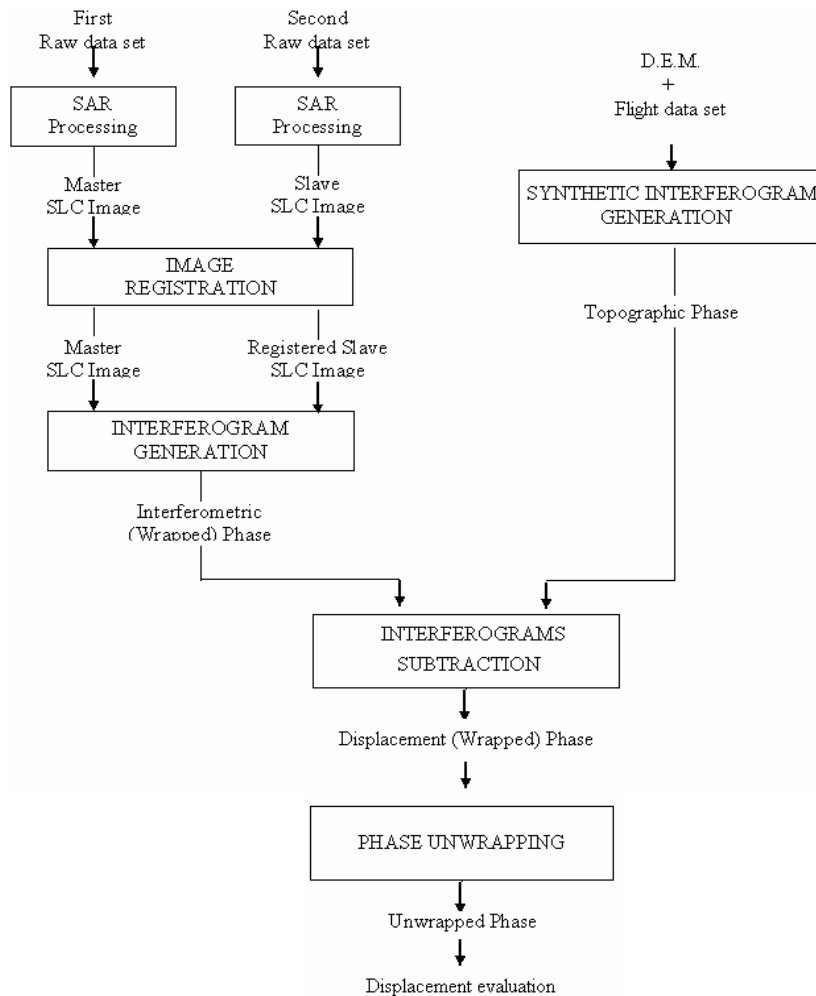


Figure 12 Block diagram of the DIFSAR processor.

again eq.(79). However, in this case, eq. (79) should be reversed because we want to ascertain the error induced on $\delta r'$ by the assumed uncertainty on z , and not vice versa. Accordingly, height measurements errors are strongly reduced when they are transferred to $\delta r'$. Moreover, differently from IFSAR (requiring large baseline for accurate three-dimensional images generation), in DIFSAR technique, the smaller the baseline l (or better, its projection onto the direction orthogonal to the look angle) the better is the accuracy of displacement measurements.

Furthermore, as already noted, decorrelation of images between the two passes is responsible for the noise associated to φ . This is a critical assumption for DIFSAR techniques, due to the fact that surface displacements are usually associated to scattering variations, for instance terrain slides. The situation is less severe for other types of displacement as fault movements [27], slow ice movements, volcanic areas deformations [26], etc..

Finally, we underline that different algorithms have been recently proposed [28], [29] and successfully applied to detect and follow the temporal evolution of deformations via the combination of several differential interferograms relative to different temporal acquisitions, with subsequent generation of surface displacement time series.

1.5 Summary

This chapter presents the basic rationale of SAR technique. Properties of the raw data collected onboard are shown, both in time (Sect. 1.1) and in spectral domain (Sect 1.2). This allows showing the basic principles of SAR focusing procedures (Sect 1.3). Final short overview on IFSAR and DIFSAR techniques is also presented (Sect 1.4).

The presented analysis, although well-known in the literature, allows introducing the formalism adopted hereafter, where the assumption of straight flight path, not realistic for airborne systems, is relaxed, and the original results of this thesis are presented.

APPENDIX I

In this appendix solution of eq. (26) is addressed.

Let us substitute eq.(22) in eq.(26); hence:

$$G(\xi, \eta, r) = \iint dx' dr' \text{rect}\left[\frac{r' - r - \Delta R}{c\tau/2}\right] \text{rect}\left[\frac{x' - x}{X}\right] \cdot \exp\left(-j \frac{4\pi}{\lambda} \Delta R\right) \cdot \exp\left[-j \frac{2\alpha}{c^2} (r' - r - \Delta R)^2\right] \cdot \exp[-j\eta(r' - r)] \cdot \exp[-j\xi(x' - x)]. \quad (92)$$

where, for the sake of simplicity, $w[\cdot]$ has been approximated with $\text{rect}[\cdot]$.
Letting

$$r' - r - \Delta R = q \quad ; \quad x' - x = p \quad (93)$$

we obtain:

$$G(\xi, \eta, r) = \int dp \text{rect}\left[\frac{p}{X}\right] \exp(-j\bar{\eta} \Delta R(p, r)) \exp(-j\xi p) \times \int dq \text{rect}\left[\frac{q}{c\tau/2}\right] \cdot \exp\left[-j \frac{2\alpha}{c^2} q^2\right] \exp(-j\eta q) \quad (94)$$

where:

$$\bar{\eta} = \eta + \frac{4\pi}{\lambda} \quad (95)$$

and:

$$\Delta R(p, r) = \sqrt{p^2 + r^2} - r \quad (96)$$

Let us now consider the following normalizations:

$$\bar{p} = \frac{p}{X} \quad ; \quad \bar{q} = \frac{q}{c\tau/2}, \quad (97)$$

leading to:

$$G(\xi, \eta, r) = \int d\bar{p} \text{rect}[\bar{p}] \exp(-j\bar{\eta} \Delta R(\bar{p}X, r)) \exp(-j\xi \bar{p}X) \times \int d\bar{q} \text{rect}[\bar{q}] \exp\left[-j \frac{2\alpha}{c^2} (\bar{q} c\tau/2)^2\right] \exp(-j\eta \bar{q} c\tau/2) \quad (98)$$

where the amplitude factors $c\tau/2$ and X deriving from the normalization (97) in eq.(94) of the differential dp and dq , respectively, have been neglected because inessential for subsequent discussion. Equation (98) is the product of two integrals, the integration domain width of which is equal to unity.

Solution of the second integral in (98):

$$\int d\bar{q} \text{rect}[\bar{q}] \exp\left[-j\frac{2\alpha}{c^2}(\bar{q}c\tau/2)^2\right] \exp(-j\eta\bar{q}c\tau/2) \quad (99)$$

is now addressed. Let us consider the argument of the first exponential:

$$\frac{2\alpha}{c^2}(\bar{q}c\tau/2)^2 = \frac{\alpha\tau^2}{2}\bar{q}^2 \approx \pi\Delta f\tau\bar{q}^2 \quad (100)$$

In all SAR system we have $\Delta f\tau = \alpha\tau^2/(2\pi) \gg 1$ (for ERS sensors, the parameters of which are collected in Table I, we have $\Delta f\tau \approx 570$); the presence of a fast varying phase term in (99) allows us applying the stationary phase method [2] for this integral evaluation; it is easy to show that the stationary phase point is given by:

$$\bar{q}_s = -\frac{\eta c}{2\alpha\tau}$$

and, accordingly, eq.(99) can be asymptotically evaluated as follows [1]:

$$\begin{aligned} & \int d\bar{q} \text{rect}[\bar{q}] \exp\left[-j\frac{2\alpha}{c^2}(\bar{q}c\tau/2)^2\right] \exp(-j\eta\bar{q}c\tau/2) \approx \\ & \approx \text{rect}[\bar{q}_s] \exp\left[-j\frac{2\alpha}{c^2}(\bar{q}_s c\tau/2)^2\right] \exp(-j\eta\bar{q}_s c\tau/2) = \\ & = \text{rect}\left[\frac{\eta}{\Omega_r}\right] \exp\left[j\frac{\eta^2}{4b}\right] \end{aligned} \quad (101)$$

where:

$$b = \frac{2\alpha}{c^2} = \frac{4\pi}{\lambda} \frac{\Delta f}{f} \frac{1}{c\tau} \quad (102)$$

$$\Omega_r = bc\tau = 2\pi \frac{2\Delta f}{c}; \quad (103)$$

and where use of eq.(12) has been made in last equality of eq.(102); moreover nonessential amplitude factors have been neglected in (101).

Evaluation of the first integral in (98):

$$\int d\bar{p} \text{rect}[\bar{p}] \exp \left[-j\bar{\eta} \left(\sqrt{(\bar{p}X)^2 + r^2} - r \right) \right] \exp(-j\xi\bar{p}X) \quad (104)$$

(where use of eq.(96) has been made) is now addressed. As for the previous case, let us focus our attention on the argument of the first exponential in (104); we first note that:

$$\sqrt{(\bar{p}X)^2 + r^2} - r \approx \frac{(\bar{p}X)^2}{2r} = \frac{\lambda^2 r^2 \bar{p}^2}{L^2 2r}; \quad (105)$$

accordingly:

$$\bar{\eta} \left(\sqrt{(\bar{p}X)^2 + r^2} - r \right) \approx \left(1 + \frac{\lambda\eta}{4\pi} \right) \frac{4\pi \lambda^2 r^2 \bar{p}^2}{\lambda L^2 2r}, \quad (106)$$

where use of (95) has been made. Furthermore, we can observe that, according to eq.(101), which multiplies the integral (104), only a limited range of values for η must be considered in (104) and (106) (see the argument of the $\text{rect}[\cdot]$ in eq.(101)); hence:

$$\left| \frac{\lambda\eta}{4\pi} \right| \leq \frac{\lambda}{4\pi} \frac{\Omega_r}{2} = \frac{1}{2} \frac{\Delta f}{f} \ll 1 \quad (107)$$

where the last inequality holds for all SAR systems. Accordingly, eq.(106) can be rewritten as follows:

$$\bar{\eta} \Delta R(\bar{p}X, r) \approx \pi \frac{2\lambda r}{L^2} = \pi \frac{2X}{L} \bar{p}^2 \quad (108)$$

In all SAR system we have $2\lambda r/L^2 = 2X/L \gg 1$ (for ERS sensors, see Table I, we have $2\lambda r/L^2 \approx 891$); accordingly, the stationary phase method can be applied also for evaluation of the integral (104). It can be shown that, in this case, the stationary phase point is given by:

$$\bar{p}_s = -\frac{1}{X} \frac{r\xi}{\sqrt{\bar{\eta}^2 - \xi^2}}$$

and, accordingly, eq.(104) can be asymptotically evaluated as follows [1]:

$$\begin{aligned}
& \int d\bar{p} \operatorname{rect}[\bar{p}] \exp\left[-j\bar{\eta}\left(\sqrt{(\bar{p}X)^2 + r^2} - r\right)\right] \exp(-j\xi\bar{p}X) \approx \\
& \approx \operatorname{rect}[\bar{p}_s] \exp\left[-j\bar{\eta}\left(\sqrt{(\bar{p}_sX)^2 + r^2} - r\right)\right] \exp(-j\xi\bar{p}_sX) = \\
& = \operatorname{rect}\left[\frac{\xi}{2\Omega_x}\right] \exp\left[-j\left(\sqrt{\bar{\eta}^2 - \xi^2} - \bar{\eta}\right)r\right]
\end{aligned} \tag{109}$$

where nonessential amplitude factors have been neglected in (109).
Use of eqs.(101) and (109) in eq. (98) easily leads to eq.(28).

We finally underline that, as discussed above, in order to correctly apply the stationary phase method for asymptotic evaluation of the integral (98), the following conditions

$$\begin{cases} \frac{2\lambda r}{L^2} = \frac{2X}{L} \gg 1 \\ \Delta f \tau = \frac{\alpha \tau^2}{2\pi} \gg 1 \end{cases} \tag{110}$$

are required to be satisfied; as shown in Sect. 1.3, conditions (110) are equivalent, see eqs.(43) and (45), to the following:

$$\begin{cases} \frac{\Delta x}{\Delta x_{raw}} \ll 1 \\ \frac{\Delta r}{\Delta r_{raw}} \ll 1 \end{cases} \tag{111}$$

where Δx and Δr are the azimuth and the range resolution, respectively, achievable by the SAR image after proper focusing operation.

TABLE I ERS Parameters

Parameters	ERS/1-2
Carrier wavelength (λ)	5.67 cm (C-band)
Transmitted Bandwidth (Δf)	15.5 MHz
pulse duration (τ)	37.1 μs
chirp rate (α)	2.62×10^{12} rad/s ²
PRF	1.678 KHz
antenna dimensions (azimuth/range)	10m x 1m
altitude	785 km
azimuth footprint (X)	100 km

References

- [1] G.Franceschetti and R.Lanari; Synthetic Aperture Radar Processing, CRC PRESS, New York, 1999
- [2] N.Bleistein and R.A.Handelsman; Asymptotic Expansion of Integrals, Dover Publications, New York, 1986.
- [3] R.H.Stolt; "Migration by Fourier Transform", *Geophysics*, 43, 23, 1978.
- [4] C.Cafforio, C.Prati and F.Rocca; "SAR data focusing using seismic migration techniques", *IEEE Trans. Aerosp. Electron. Syst.*, 27, 194, 1991.
- [5] F.Rocca; "Synthetic Aperture Radar: a New Application for Wave Equation Techniques", Stanford Exploration Project Report, SEP-56, 1987.
- [6] R.Bamler; "A comparison of range-Doppler and wavenumber domain SAR focusing algorithms", *IEEE Trans. Geosci. Remote Sens.*, 30, 706, 1992.
- [7] G.Franceschetti, R.Lanari and E.S.Marzouk; "Efficient and high precision space-variant processing of SAR data", *IEEE Trans. Aerosp. Electron. Syst.*, 31, 227, 1995.
- [8] R.K.Raney, H.Runge, R.Bamler, I.G.Cumming and F.Wong; "Precision SAR processing using chirp scaling", *IEEE Trans. Geosci. Remote Sens.*, 32, 786, 1994.
- [9] R.Lanari; "A new method for the compensation of the SAR range cell migration based on the chirp Z-transform", *IEEE Trans. Geosci. Remote Sens.*, 33, 1995.
- [10] R.Lanari and G.Fornaro; "A short discussion on the exact compensation of the SAR range-dependent range cell migration effect", *IEEE Trans. Geosci. Remote Sens.*, 35, 1446, 1997.
- [11] G.Fornaro, E.Sansosti, R.Lanari and M.Tesauro; "Role of Processing Geometry in SAR Raw Data Processing", *IEEE Trans. Aerosp. Electron. Syst.*, 38, 2002.
- [12] L.C.Graham; "Synthetic interferometer radar for topographic mapping", *Proc. IEEE*, 62, 763, 1974.
- [13] H.A.Zebker and R.M.Goldstein; "Topographic mapping from synthetic aperture radar observations", *J. Geophys. Res.*, 91, 4993, 1986.
- [14] S.Madsen, H.A.Zebker and J.Martin; "Topographic mapping using radar interferometry: processing techniques", *IEEE Trans. Geosci. Remote Sens.*, 34, 246, 1993.

- [15] J.C.Curlander and R.McDonough; Synthetic Aperture Radar – System and Signal Processing, New York, Wiley
- [16] G.Fornaro and G.Franceschetti; "Image registration in Interferometric SAR Processing", IEE Proc.-Radar, Sonar, Navig., 142, 1995.
- [17] R.Bamler and M.Einder; "Accuracy of Differential Shift Estimation by Correlation and Split-Bandwidth Interferometry for Wide Band and Delta-k SAR systems", IEEE Geosci. Remote Sens. Lett., 2, 2005.
- [18] Q.Lin , J.F.Vesecky and H.A.Zebker; "New approaches in interferometric SAR data processing", IEEE Trans. Geosci. Remote Sens., 30, 1992.
- [19] R.M.Goldstein, H.A.Zebker and C.L.Werner; "Satellite radar interferometry: two-dimensional phase unwrapping", Radio Sci., 23, 1988.
- [20] G.Fornaro, G.Franceschetti and R.Lanari; "Interferometric SAR Phase Unwrapping Using Green's Formulation", IEEE Trans. Geosci. Remote Sens., 34, 1996.
- [21] D.C.Ghiglia. and L.A.Romero; "Robust two-dimensional weighted and unweighted phase unwrapping that uses fast transform and iterative methods", J. Opt. Soc. Am. A, 11, 1994.
- [22] D.C.Ghiglia and M.D.Pritt; Two-Dimensional Phase Unwrapping: Theory, Algorithms and Software, John Wiley and Sons New York, 1998.
- [23] R.Bamler and D.Just; "Phase statistics of interferograms with application to synthetic aperture radars" Applied Optics, 33, 1994.
- [24] H.A.Zebker and J.Villasenor; "Decorrelation in Interferometric Radar Echoes", IEEE Trans. Geosci. Remote Sens., 30, 1992.
- [25] K.Gabriel, R.M. Goldstein and H.A.Zebker; "Mapping small elevation changes over large areas: Differential interferometry", J. Geophys. Res., 94, 1989.
- [26] D.Massonnet, P.Briole and A.Arnaud; "Deflation of Mount Etna monitored by spaceborne radar interferometry", Nature, London, 375, 567, 1995.
- [27] D.Massonnet, M.Rossi, C.Carmona, F.Ardagna, G.Peltzer, K.Feigl and T.Rabaute; "The displacement field of the Landers earthquake mapped by radar interferometry", Nature, 364, 138-142, 1993
- [28] A.Ferretti, C.Prati and F.Rocca; "Permanent scatterers in SAR interferometry", IEEE Trans. Geosci. Remote Sens., 39, 1, 2001.
- [29] P.Berardino, G.Fornaro, R.Lanari and E.Sansosti; "A new Algorithm for Surface Deformation Monitoring based on Small Baseline Differential SAR Interferograms", IEEE Trans. Geosci. Remote Sens., 40, 11, 2002.

Chapter 2

Airborne SAR Acquisition Model

SAR raw signal simulation is a useful tool for SAR system design, mission planning, processing algorithm testing, and inversion algorithm design. However, time domain simulation of extended scenes is enormously time consuming and therefore not easily viable.

In Chapter 1 the expression of the SAR raw data collected onboard has been shown, and evaluation, via the stationary phase method, of its spectrum has been presented. Based on such an analysis, a 2-D Fourier domain SAR raw signal simulator, exploiting the efficiency of FFT algorithms, has been presented some years ago [1]-[3] and is able to generate the raw signal corresponding to extended scenes in a few seconds.

Unfortunately, the efficient SAR simulator presented in [1]-[3] is based, similarly to the analysis shown in Chapter 1, on the assumption that the sensor flight path is a straight line. This is usually a good approximation for a short portion of the elliptical orbit of a spaceborne sensor. However, in the case of airborne sensors, significant deviations from the ideal trajectory may occur due to the presence of atmospheric turbulences. In the SAR jargon, raw data acquired in this condition are said to be affected by motion errors [4]-[10].

In this Chapter we extend the simulator [1]-[3] to include the effects of motion errors.

The “nominal trajectory” simulator of [1]-[3] employs a procedure that consists of two main stages. In the first stage, given the nominal orbit (or flight) data and the scene geometric and electromagnetic parameters, the scene reflectivity map is evaluated. In the second stage, the SAR raw signal is computed via a superposition integral in which the reflectivity map is weighted by the SAR system two-dimensional (2-D) pulse response (see Sect. 1.1). This superposition integral is efficiently evaluated in the Fourier domain via FFT codes. When we move to the case of trajectory deviations, the first stage, i.e., the reflectivity map generation, remains conceptually unchanged. With regard to the second stage, first of all the SAR system 2-D pulse response must be properly changed. In addition, the use of the Fourier domain formulation is not straightforward, because the overall SAR system transfer function turns out to depend on the azimuth and range coordinates of the ground point [5]-[10]. In order to deal with this more complex (and more realistic, for airborne systems) case, we first of all obtain, for the first time, a

general, i.e. without approximations, and compact Fourier Domain formulation of the SAR raw signal in the presence of arbitrary trajectory deviations, thus extending the SAR raw data analysis presented in Chapter 1 to the airborne case. Such an analysis allows us to show that in this general case no efficient simulation scheme can be devised.

However, in this Chapter it is shown that, if some reasonable assumptions on the sensor motion and on the SAR system features are made, an efficient simulation approach can be used: it consists of a 1-D azimuth Fourier domain processing followed by a range time domain integration. This approach turns out to be still much more efficient than the time domain ones presented in [11]-[14], so that airborne raw data acquired in the presence of track deviations and relative to extended scenes can be simulated, for the first time, in a few minutes. In addition, we show that if a narrow beam and slow deviation assumption is made, a full 2-D Fourier domain simulation can be used. This latter approach can be applied only to some SAR systems, but it has the advantage that processing time is practically unchanged with respect to the nominal trajectory case.

We finally underline that in this Chapter we only deal with sensor trajectory deviations, and not with airplane attitude variations: the inclusion of the effects of attitude variations in the simulation scheme is possible, and will be matter of future work.

2.1 Raw data spectrum

Let us refer to Fig. 1 in which the SAR system geometry in the presence of trajectory displacements from an ideal rectilinear track is shown: as usual, a cylindrical reference system, the axis of which coincides with the nominal, i.e., rectilinear, trajectory is considered. The position of the illuminating antenna is now completely described by the azimuth coordinate x' and by the vector $\vec{d}(x')$, the y and z components of which represent the horizontal and vertical platform displacements from the nominal track. As usual (see Table of Symbols) we denote with:

- (x,r) the azimuth and (slant) range coordinates of the scene generic scattering point P ;
- $\mathcal{A}(x,r)$ the soil surface equation in cylindrical coordinates, also referred to as *look angle*, which allows calculation of the local look angle from the range and azimuth position of the ground point (it can be derived from knowledge of the nominal sensor line of flight and of the scene topography [1], [2], [3]);

moreover, we denote with:

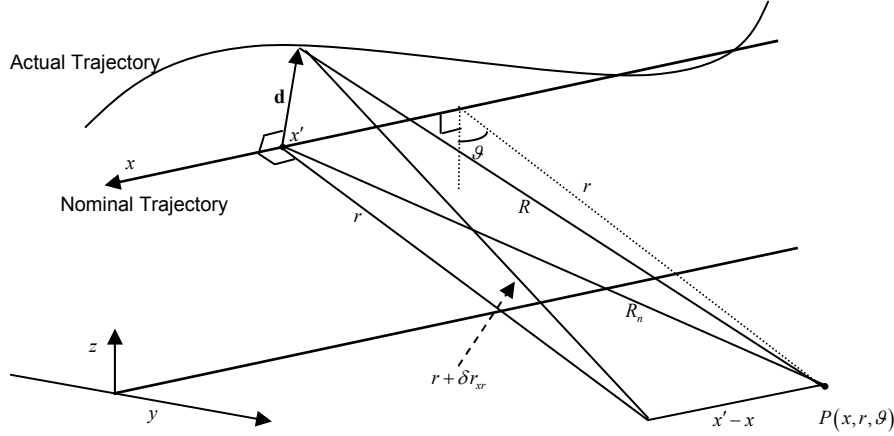


Figure 1 SAR system geometry in the presence of trajectory deviation.

- R and R_n the target-to-antenna distances in the generic antenna position for actual and nominal trajectories, respectively.

The absence of any squint angle is assumed in the following.

From Fig. 1 we have the following expression for R and R_n [5], [8]:

$$R = R(x', x, r) = \sqrt{(r + \delta_{xr}(x', x, r))^2 + (x' - x)^2} \quad (1)$$

$$R_n = R_n(x' - x, r) = \sqrt{r^2 + (x' - x)^2} = r + \Delta R(x' - x, r) \quad (2)$$

where eq.(2) corresponds to eq.(3) in Chapter 1. The $\delta_{xr}(\cdot)$ term can be evaluated by the application of the Carnot Theorem (see also Fig. 2) as follows:

$$\begin{aligned} \delta_{xr}(x', x, r) &= \sqrt{r^2 + d(x')^2 - 2d(x')r \sin(\mathcal{A}(x, r) - \beta(x'))} - r \approx \\ &\approx -d(x') \sin(\mathcal{A}(x, r) - \beta(x')); \end{aligned} \quad (3)$$

where $d(x') = |\vec{d}|$ and $\beta(x')$ are related to the platform displacements; the last approximation holds when displacements are small compared with the target slant range, as it is always the case; in this case $\delta_{xr}(\cdot)$ reduces to the displacement projection onto the target line of sight. It is recognized that $\delta_{xr}(\cdot)$ depends on both the sensor position, through $d(x')$ and $\beta(x')$, and on the topography, through $\mathcal{A}(x, r)$.

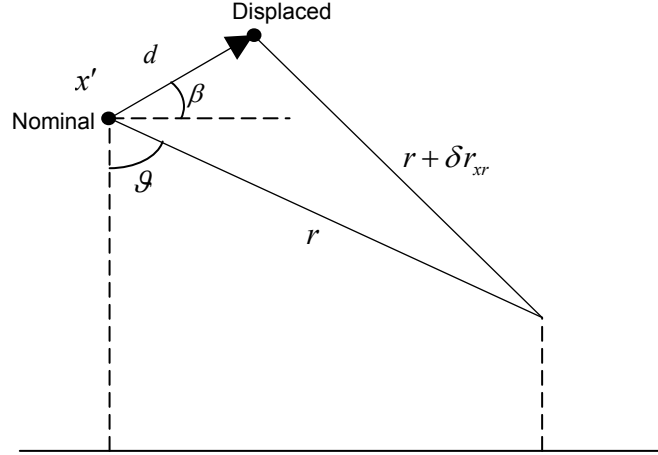


Figure 2 SAR system geometry in cross (nominal) track plane.

Let us assume, as usual, that the transmitted signal is a chirp pulse, the carrier frequency, chirp-rate and chirp duration of which are (see Table of Symbols) f , τ and α , respectively.

The expression of the received signal after the heterodyne step is the following, [1]:

$$h(x', r') = \iint dx dr \gamma(x, r) \text{rect} \left[\frac{r' - R}{c\tau/2} \right] w^2 \left(\frac{x' - x}{X} \right) \cdot \exp \left[-j \frac{4\pi}{\lambda} R - j \frac{2\alpha}{c^2} (r' - R)^2 \right]; \quad (4)$$

where, as usual (see Table of Symbols):

- $r' = ct/2$ is the range signal sampling coordinate (c being the speed of the light);
- λ is the carrier wavelength;
- $\gamma(x, r)$ is the surface reflectivity pattern;
- $w(\cdot)$ is the antenna ground illumination pattern, usually approximated to $\text{rect} \left[\frac{x' - x}{X} \right]$;
- $X = \lambda r/L$ is the azimuth footprint, coincident with the synthetic antenna length;
- L is the effective azimuth length of the physical antenna.

We observe that the expression of the raw data collected in the presence of sensor trajectory displacement is similar to the one obtained in the absence of motion errors (see eq.(23), Chapter 1). However, the expression of the term $R(\cdot)$ is different in the two cases (compare eq.(1) in this Chapter to eq.(3) in Chapter 1): the term $R(\cdot)$ now introduces azimuth space-variant effects in eq.(4) that must be accounted for. Letting:

$$R(x', x, r) = R_n(x' - x, r) + \delta R(x', x, r) \quad (5)$$

the Fourier Transform (FT) of eq.(4) along the range direction can be obtained by applying the stationary phase method, see Appendix I:

$$H(x', \eta) = \text{rect} \left[\frac{\eta}{\Omega_r} \right] \exp \left[j \frac{\eta^2}{4b} \right] \times \iint dx dr \gamma(x, r) \exp \left[-j \left(\eta + \frac{4\pi}{\lambda} \right) (r + \Delta R + \delta R) \right] w^2 \left(\frac{x' - x}{X} \right); \quad (6)$$

where b is defined in Chapter 1, see eq. (29). and Ω_r , as usual, is the SAR system range spatial bandwidth (rad/m), see eq. (31) in Chapter 1.

The expression of the FT of eq.(6) along the azimuth direction is the following (see Appendix II):

$$H(\xi, \eta) = \int dr \exp[-j\bar{\eta}r] \int dl G(\xi - l, \eta, r) F(\xi - l, l, \eta, r) \quad (7)$$

where:

$$F(\chi, l, \eta, r) = \iint dx dx' f(x, x', \eta, r) \exp(-jx\chi) \exp(-jx'l) \quad (8)$$

$$f(x, x', \eta, r) = \gamma(x, r) \exp \left[-j \left(\eta + \frac{4\pi}{\lambda} \right) \delta R(x', x, r) \right] \quad (9)$$

and

$$G(\xi, \eta, r) = \text{rect} \left[\frac{\eta}{\Omega_r} \right] w^2 \left(\frac{\xi}{\Omega_x} \right) \cdot \exp \left[j \frac{\eta^2}{4b} \right] \cdot \exp \left[-j \left(\sqrt{\bar{\eta}^2 - \xi^2} - \bar{\eta} \right) r \right] \quad (10)$$

Ω_x being, as usual, the SAR system azimuth spatial bandwidth (rad/m), see eq.(30) in Chapter 1, and $\bar{\eta} = \eta + 4\pi/\lambda$.

Some considerations about eq.(7) are now in order.

First of all, we underline that it represents the general expression of the SAR raw data spectrum in the presence of sensor trajectory displacements.

Furthermore, we observe that the trajectory deviation has no impact on the expression of $G(\cdot)$, which coincides with the standard, i.e., in the absence of motion errors, SAR System Transfer Function (STF) introduced in Chapter 1, see eq.(28). This is not the case for $F(\cdot)$, which strongly depends on the trajectory displacement, see eqs. (8), (9).

Finally, we note that in the absence of motion errors eqs. (9) and (8) simplify as:

$$f(x, x', \eta, r) = \gamma(x, r) \quad (11)$$

$$F(\chi, l, \eta, r) = \delta(l) \int dx \gamma(x, r) \exp[-jx\chi] \quad (12)$$

where $\delta(\cdot)$ represents the Dirac impulse. Accordingly, eq.(7) can be rearranged as follows:

$$\begin{aligned} H(\xi, \eta) &= \int dr \exp[-j\eta r] \int dl \delta(l) G(\xi - l, \eta, r) \int dx \gamma(x, r) \exp[-jx(\xi - l)] = \\ &= \iint dx dr \gamma(x, r) G(\xi, \eta, r) \exp[-j\eta r] \exp[-jx\xi] \\ &= \iint dx dr \bar{\gamma}(x, r) G(\xi, \eta, r) \exp[-j\eta r] \exp[-jx\xi] \end{aligned} \quad (13)$$

where, as usual, $\bar{\gamma}(x, r) = \gamma(x, r) \exp(-j4\pi r/\lambda)$ (see Table of Symbols): equation (13), in this case, is recognized to be coincident with the standard raw data spectrum expression in the absence of sensor deviation errors (see eq.(24), Chapter 1).

2.2 Raw data simulation

The integral of eq. (13), which is appropriate in the absence of motion errors, can be efficiently evaluated as the multiplication of $G(\xi, \eta, r=r_0)$ and a properly resampled version of the FT $\Gamma(\xi, \eta)$ of $\gamma(x, r)$, because, as shown in Section 1.3, the range dependence of $G(\cdot)$ can be accounted for by modifying the range Fourier kernel of eq.(13) [4].

Conversely, in the more general case, the $f(\cdot)$ term shows the involved azimuth and range space-variant effects of the displacement motion error, which strongly impair the computational efficiency of the evaluation of eq.(7) and, consequently, of the raw signal simulator. In the following we explore the possibility to rearrange the integral of eq.(7) in order to

efficiently evaluate its expression. To this end, let us consider eq.(5). We can first separate $\delta R(\cdot)$ into azimuth space invariant and variant contributions:

$$\delta R(x', x, r) = \delta R(x', x', r) + \varphi(x', x, r) = \delta r_r(x', r) + \varphi(x', x, r) \quad (14)$$

where $\delta r_r(x', r) = \delta r_{x'}(x', x', r)$, see also eqs.(1) and (2), can be in turn separated into its range space invariant (at the scene center) and variant contributions as follows:

$$\delta r_r(x', r) = \delta r(x') + \psi(x', r) \quad (15)$$

where $\delta r(x') = \delta r_r(x', r_0)$, r_0 being the range coordinate of the scene center. We underline that $\psi(x', r)$ is zero at the scene center ($r=r_0$), and increases as we move away from the scene center.

Accordingly, eq.(14) can be rearranged as follows:

$$\delta R(x', x, r) = \delta r(x') + \psi(x', r) + \varphi(x', x, r) . \quad (16)$$

Eq.(16) shows that the difference between $R(\cdot)$ and $R_n(\cdot)$ can be separated in three different terms: $\delta r(x')$, which represents the projection of the trajectory displacement onto the look direction at the scene center ($r=r_0$) and depends only on the sensor azimuth coordinate x' , thus not showing any space variant behavior; $\psi(x', r)$, which accounts for the variation of the projection of displacement onto the local look direction with respect to the scene center case, and depends also on the target range coordinate r , thus showing only a range-variant behavior; $\varphi(x', x, r)$, which includes also the azimuth-variant effects of the sensor displacement, as will be better clarified in Section 2.2.1.1 The different roles of these three terms in the computational efficiency of the simulator is related to their impact on eq.(8), and will be clarified in the following.

Let us now address our attention on the $\delta r(x')$ term. Since it does not depend on the (x, r) coordinates, it can be conveniently brought out from the integral of eq.(6) as follows:

$$H(x', \eta) = \exp\left[-j\left(\eta + \frac{4\pi}{\lambda}\right)\delta r(x')\right] \bar{H}(x', \eta) \quad (17)$$

where (see eqs. (16) and (6)):

$$\begin{aligned} \bar{H}(x', \eta) = & \text{rect}\left[\frac{\eta}{\Omega_r}\right] \exp\left[j\frac{\eta^2}{4b}\right] \iint dx dr \gamma(x, r) w^2\left(\frac{x' - x}{X}\right) \\ & \cdot \exp\left[-j\left(\eta + \frac{4\pi}{\lambda}\right)\left[r + \Delta R(x', x, r) + \psi(x', r) + \varphi(x', x, r)\right]\right] \end{aligned} \quad (18)$$

Some consideration about eq. (17) are now in order.

Let us suppose that, in some way, we are able to efficiently evaluate the azimuth FT $\bar{H}(\xi, \eta)$ of $\bar{H}(x', \eta)$: an inverse FT along ξ , a simple multiplication by the exponential term in eq. (17), and a subsequent inverse FT along η , would allow us to obtain the SAR raw data expression of eq.(4). This procedure is illustrated by the block scheme of Fig. 3. Accordingly, in the following we focus our attention on the $\bar{H}(x', \eta)$ term and we explore the possibility to efficiently evaluate its azimuth FT $\bar{H}(\xi, \eta)$. This approach, which allows us to separately and exactly account for the space-invariant component of the displacement term of eq.(16), presents computational advantages that will be clarified in the next Sections.

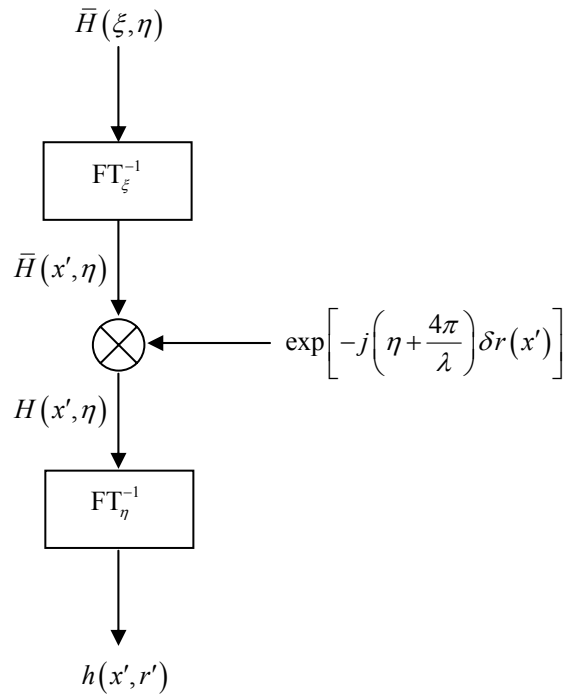


Figure 3 Block scheme of the proposed simulation approach.

The expression of the azimuth FT of eq. (18) can be simply obtained along the same lines shown in Appendix II. Accordingly:

$$\bar{H}(\xi, \eta) = \int dr \exp[-j\eta r] \int dl G(\xi - l, \eta, r) \bar{F}(\xi - l, l, \eta, r) \quad (19)$$

where:

$$\bar{F}(\chi, l, \eta, r) = \iint dx dx' \bar{f}(x, x', \eta, r) \exp(-jx\chi) \exp(-jx'l) \quad (20)$$

$$\bar{f}(x, x', \eta, r) = \gamma(x, r) \exp\left\{-j\left(\eta + \frac{4\pi}{\lambda}\right)[\psi(x', r) + \varphi(x', x, r)]\right\}. \quad (21)$$

Let us note that eqs. (19)-(20) are formally equal to eqs.(7)-(8), and eq.(21) differs from eq.(9) only for the absence of the $\exp[-j(4\pi/\lambda + \eta)\delta r(x')]$ term, which is accounted for in the multiplication of eq.(17).

In the following we make useful assumptions that allow us to properly modify eq.(21) and, accordingly, to rearrange and efficiently evaluate eq. (19). Then, the processing scheme shown in Fig. 3 can be used to simulate the collected SAR raw data in the presence of sensor trajectory displacements of eq. (4).

2.2.1 Narrow beam and slow track deviations

It is highly desirable to express eq.(19) in a form similar to eq. (13), so that a full 2-D Fourier domain efficient simulation can be used. This is possible if we consider the following approximation of eq.(21):

$$\bar{f}(x, x', \eta, r) \approx \gamma(x, r) \exp\left\{-j\frac{4\pi}{\lambda}\psi(x, r)\right\} = \bar{\gamma}(x, r) \quad (22)$$

which holds when:

$$\left|\left(1 + \frac{\lambda\eta}{4\pi}\right)\varphi(x, x', r) + \frac{\lambda\eta}{4\pi}\psi(x', r) + [\psi(x', r) - \psi(x, r)]\right| \ll \frac{\lambda}{4\pi} \quad (23)$$

Let us note that, see Chapter 1, eq.(107), we can write $\left|\frac{\eta\lambda}{4\pi}\right| = \frac{1}{2} \frac{\Delta f}{f} \ll 1, f$

and Δf being the carrier frequency and the transmitted bandwidth (Hz), respectively; accordingly relation (23) requires that the following three conditions are all satisfied:

$$|\varphi(x', x, r)| \ll \frac{\lambda}{4\pi} \quad (24)$$

$$|\psi(x', r)| \ll \frac{f}{\Delta f} \frac{\lambda}{2\pi} \quad (25)$$

$$|\psi(x', r) - \psi(x, r)| \ll \frac{\lambda}{4\pi} \quad (26)$$

where the last condition must be enforced inside a synthetic antenna length. Should the inequalities (24)-(26) be satisfied, the function $\bar{f}(\cdot)$ does not depend on the azimuth sensor position x' , nor on the range frequency η , so that eq.(20) simplifies as:

$$\bar{F}(\chi, l, \eta, r) = \delta(l) \int dx \bar{\gamma}(x, r) \exp(-j\chi x) = \bar{F}(\chi, l, r) \quad (27)$$

Accordingly:

$$\begin{aligned} \bar{H}(\xi, \eta) &= \int dr \exp[-j\bar{\eta}r] \int dl \delta(l) G(\xi - l, \eta, r) \int dx \bar{\gamma}(x, r) \exp[-j(\xi - l)x] = \\ &= \iiint dx dr \bar{\gamma}(x, r) G(\xi, \eta, r) \exp[-j\bar{\eta}r] \exp[-j\xi x] \end{aligned} \quad (28)$$

The expression of eq.(28) is formally equal to eq.(13); accordingly, it can be efficiently evaluated as the multiplication of $G(\xi, \eta, r=r_0)$ and a proper re-sampled version of the FT $\bar{\Gamma}(\xi, \eta)$ of $\bar{\gamma}(x, r)$ along the lines shown in [1]. The final evaluation of the SAR raw data in the presence of sensor trajectory displacements can now simply be performed according to the scheme shown in Fig. 3. Equation (28) can be also obtained by using eq. (23) directly in eq.(18), and asymptotically evaluating its azimuth FT as in [4] or [1].

2.2.1.1 Validity limits

A discussion on the approximations employed in the proposed approach is now appropriate. Condition (24) requires that the azimuth space variant term $\varphi(x', x, r)$ of the displacement is much smaller than the wavelength. Physically, this approximation, often referred to as center-beam approximation in the literature [15], corresponds to assuming that the topography is smooth enough to let $\mathcal{A}(x, r) = \mathcal{A}(x', r)$ within the azimuth beam, so that $\delta r_{x'}(x', x, r) \approx \delta r_r(x', r)$, see eq.(3), and that the azimuth beam is narrow enough to consider, for a generic sensor position x' , the displacement error δR for all the targets within the beam (in azimuth direction) equal the one of the center beam target ($x'=x$) [5],[8], [15] so that:

$$\delta R(x', x, r) \approx \delta r_r(x', r) \quad (29)$$

see eq.(14). In Appendix III it is shown that the following condition,

$$d_{\max} \ll \frac{L}{\lambda} \cdot \frac{L}{2} = \frac{\text{azimuth resolution}}{\text{azimuth beam width}} \quad (30)$$

ensures that inequality (24) is satisfied. In eq.(30) d_{\max} is the maximum value of the trajectory deviation. For a typical X-band airborne SAR sensor, the system parameters of which are reported in Table I, eq.(30) requires that $d_{\max} \ll 15$ m.

Let us now move to consider relations (25) and (26). Condition (25) requires that the range space variant term $\psi(x', r)$ of the displacement is much smaller than the range resolution. Since this term is zero at the scene center ($r=r_0$), and increases as we move away from the scene center, it is clear that conditions (25) is more easily satisfied if the range beam is narrow. In Appendix III it is shown that the following condition

$$d_{\max} \ll \frac{L_r}{\lambda} \cdot \frac{c}{2\Delta f} = \frac{\text{range resolution}}{\text{range beam width}} \quad (31)$$

ensures that inequality (25) is satisfied. In eq.(31) L_r is the effective range length of the physical antenna. For the typical X-band airborne SAR sensor of Table I, eq.(31) requires that $d_{\max} \ll 8$ m.

Condition (26) requires that the variations of the range space variant term $\psi(x', r)$ within a synthetic aperture length are much smaller than the wavelength, so that we can let $\psi(x', r) \approx \psi(x, r)$. It is clear that condition (26) is more easily satisfied if the trajectory deviations are slow. In fact, as shown in Appendix III, for flat or gently sloped terrains inequality (26) is certainly satisfied if the following condition is verified:

$$d_{\max} \ll \frac{L_r}{\pi \Omega_d X} \quad (32)$$

where Ω_d is the spatial bandwidth of the trajectory displacement. For the typical X-band airborne SAR sensor of Table I, eq.(33) requires that $d_{\max} \ll 3$ cm for $\Omega_d = 1/X = 7 \cdot 10^{-3} \text{ m}^{-1}$ (fast deviations), and $d_{\max} \ll 3$ m for $\Omega_d = 1/(100 \cdot X) = 7 \cdot 10^{-5} \text{ m}^{-1}$ (slow deviations). Accordingly, we can conclude that for typical SAR systems condition (33) is the most stringent, and that the presented approach can be used to account for fast (high frequency), very small (sub-centimetric) deviations (“antenna vibrations”) or for slow, larger (up to the meter) deviations (slow platform trajectory displacement).

Equations (30)-(32) allow, given the SAR system and the maximum trajectory deviation and bandwidth, to readily decide if the proposed approach can be safely used.

2.2.1.2 Simulation results

In this Section we present some examples aimed at assessing the validity of the proposed simulation approach. We consider a typical X-band airborne SAR system, the main parameters of which are listed in Table I. The platform is supposed to move along a trajectory that differs from the nominal straight line one by a time varying amount, the horizontal and vertical components of which are plotted in Fig. 4. We consider a portion of the sensor flight that corresponds to about two azimuth footprints, i.e., about 300 meters, corresponding to about 3 seconds at the sensor velocity of 100 m/s. This trajectory displacement satisfies conditions (30)-(32) and hence (24)-(26).

As a first example, we consider a scene consisting of a single pointlike scatterer placed at midrange ($r=5140$ m) over a completely absorbing background. For such a scene, consisting of a single scatterer, the SAR raw signal can be exactly computed directly in time domain using eq.(4). Accordingly, it is possible to compare the raw signal simulated via the proposed approach, described in Section 2.2.1, to the exact one. Range and azimuth cuts of the phase difference between simulated and exact raw signals are plotted in Figs. 5a and 5b, respectively (oscillating lines). This phase error is limited to a few degrees for most part of the raw signal, and reaches 18 degrees (i.e., $\pi/10$ radians) only at its very edge. It must be noted that most of the phase error of Figs. 5a and 5b is not due to the approximations involved in the simulation of the trajectory displacement effects, but it is simply caused by the asymptotic evaluation of the SAR system transfer function via the stationary phase method, so that it would be present also in the ideal trajectory case. To better emphasize this point, we can consider the phase difference between the raw signal simulated in the presence of trajectory deviations and the raw signal simulated in the case of ideal trajectory: this difference can be then compared to the difference between the correspondent exact raw signals. In this way, we can evaluate the phase error “depurated” from the term due to the stationary phase approximation. Range and azimuth cuts of this “depurated” phase error are also plotted in Figs. 5a and 5b, respectively (smooth lines). It turns out that this error is always below one degree: this is not surprising, considering that the target is placed at midrange, where the approximations made in the simulation procedure are expected to be negligible.

TABLE I Simulated Sensor Parameters

Nominal height	4000 m	Range pixel dimension	3 m
Midrange coordinate	5140 m	Chirp bandwidth	45 MHz
Wavelength	3.14 cm	Chirp duration	5 μ s
Platform velocity	100 m/s	Azimuth antenna dimension	1 m
Pulse Repetition Frequency	400 Hz	Range antenna dimension	8 cm
Sampling Frequency	50 MHz	Number of azimuth samples of the raw signal	1941
Azimuth pixel dimension	25 cm	Number of range samples of the raw signal	830

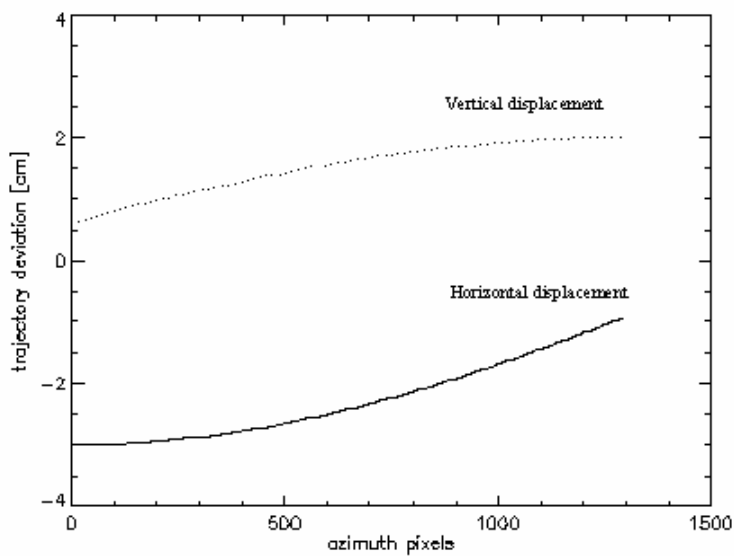


Figure 4 Simulated trajectory deviations relative to Figs. 5-8.

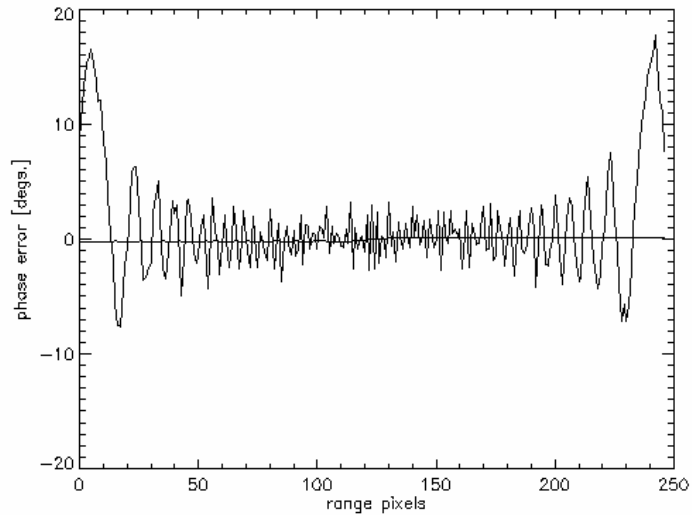


Figure 5a

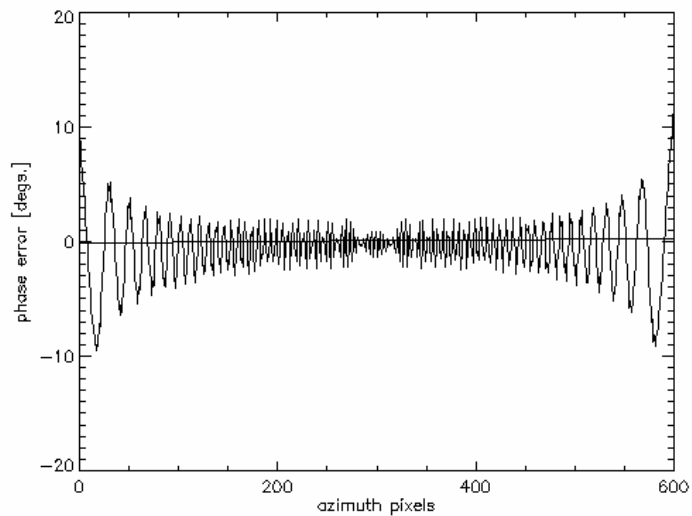
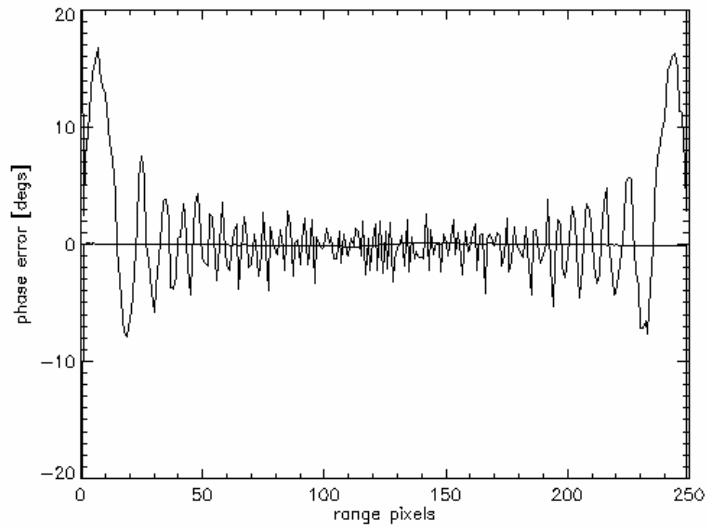
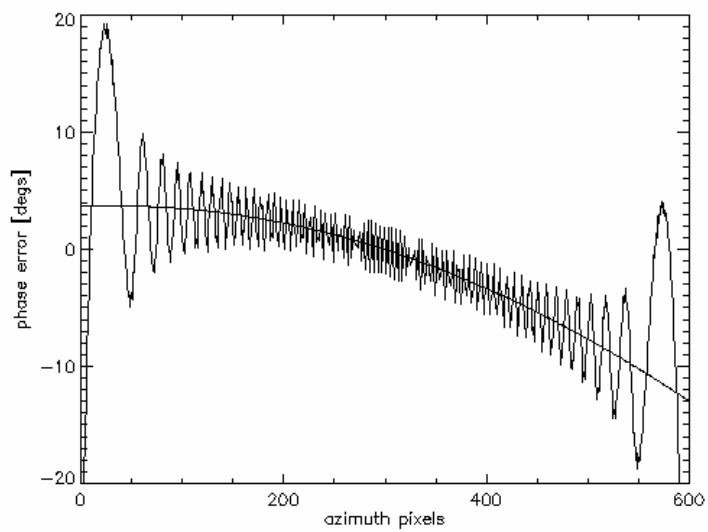


Figure 5b

Simulation method of Sect. 2.2.1 in the presence of the track deviations of Fig. 4. Range (a) and azimuth (b) cuts of the overall phase error for a target located at the midrange, i.e., at $r=5140$ m, before (oscillating line) and after (smooth line) removing the aberrations induced by the stationary phase method (see the body of the paper). The Figure refers to a window, centered around the target location pixel, the range size of which is equal to the spatial length of the simulated transmitted chirp pulse (750 m according to Table I), and the azimuth size of which is equal to the length of the simulated azimuth footprint (about 150 m according to Table I).

The presented situation changes if we move to consider a new scene consisting of a pointlike target placed at near range ($r=4600$ m). Range and azimuth cuts of the corresponding overall phase error are reported in Figs. 6a and 6b, respectively (oscillating lines). While the range cut is very similar to the one obtained in the midrange target case, the azimuth cut shows a larger error (however, it is always confined between -20 and $+20$ degrees). This situation is more clearly shown by observing range and azimuth cuts of the “depurated” phase error, also plotted in Figs. 6a and 6b (smooth lines). It is evident that the phase error due to the approximated way used to account for trajectory deviations varies from $+4$ to -16 degrees as we move along the azimuth direction. This is certainly expected, considering that the approximations made in the simulation procedure are stronger when the target is farther from midrange. However, even in this more critical situation, the phase error is limited to about $\pm\pi/10$ radians, which is certainly an acceptable value, especially considering that the error is much smaller than that for most part of the raw signal. It must also be noted that this error is almost completely due to the approximation of eq.(26), whereas conditions (24) and (25) are very well satisfied. To verify this, in Fig. 7 we plot the graph of $[4\pi/\lambda] \cdot [\psi(x',r) - \psi(x,r)]$ for $r=4600$ m and for the system parameters of Table I and deviation of Fig. 4. This plot is practically coincident with Fig. 6d, and this confirms that the obtained phase error is due to the approximation of eq.(26).

Finally, in order to give an example of the simulation scheme efficiency, we simulated (by using the same SAR system parameters of Table I and the same trajectory displacement of Fig. 4) the raw signal corresponding to an extended scene, the height profile of which is a pyramid. Simulation of this 830 by 1941 pixel raw signal took about 3 seconds on a 1 GHz Pentium IV PC. The final image obtained by processing the simulated raw signal is reported in Fig. 8.

**Figure 6a****Figure 6b**

As Fig. 5, but considering a target located at near range, at $r=4600$ m.

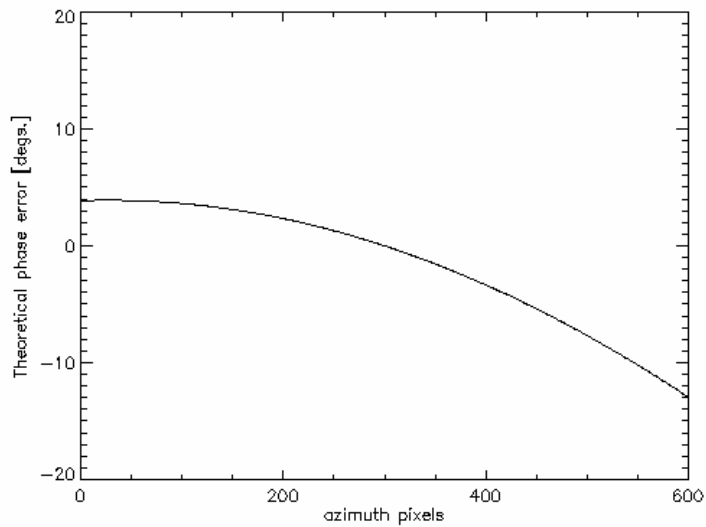


Figure 7 Expected phase error along the azimuth direction for a near range target located at $r=4600$ m, according to eq.(26). To be compared to Fig. 6b.

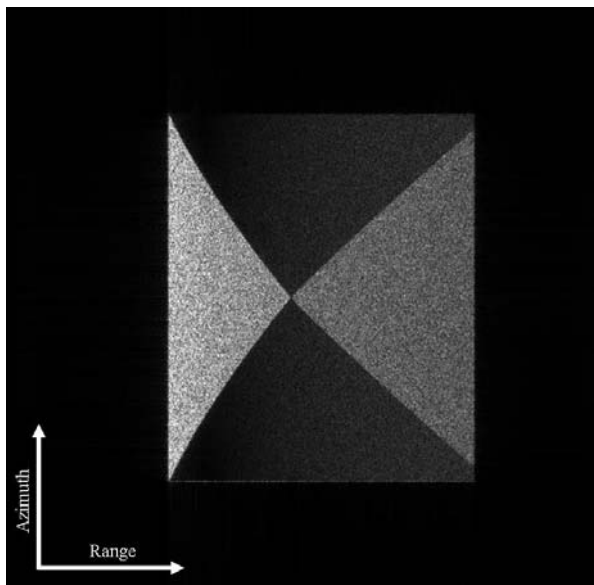


Figure 8 Multi-look image of a pyramid, obtained by processing the simulated SAR raw signal acquired by the sensor of Table I in the presence of the trajectory deviations of Fig. 4. A 8 azimuth x 4 range pixel averaging window has been used to perform the multi-look operation.

2.2.2 Narrow azimuth beam and arbitrary track deviations

By summarizing the results of sect. 2.2.1, we can say that, if conditions (24)-(26), equivalent to conditions (30)-(32), are satisfied, a full 2-D Fourier domain approach can be used to evaluate the raw SAR signal of eq.(4) collected in the presence of trajectory deviations, with practically no computational time increase with respect to the nominal trajectory case [1]. In particular, condition (31) sets an upper limit on the range beam size (and/or a lower limit on the resolution cell range size), and condition (32) poses an upper limit on the displacement rapidity.

In the following we will relax conditions (31) and (32), and will retain only condition (30).

If condition (30) is satisfied, then eq.(21) can be expressed as:

$$\bar{f}(x, x', \eta, r) \approx \gamma(x, r) \exp \left\{ -j \left(\eta + \frac{4\pi}{\lambda} \right) \psi(x', r) \right\}. \quad (33)$$

The $\bar{f}(\cdot)$ function can now be factorized in two terms which depend separately on the x and x' variables; accordingly, eq.(20) can be written as follows:

$$\bar{F}(\chi, l, \eta, r) = \Gamma(\chi, r) Q_\eta(l, \eta, r) \quad (34)$$

where:

$$Q_\eta(l, \eta, r) = \text{FT}_{x'} \left\{ \exp \left[-j \left(\eta + \frac{4\pi}{\lambda} \right) \psi(x', r) \right] \right\} \quad (35)$$

thus allowing us to obtain:

$$\begin{aligned} \bar{H}(\xi, \eta) &= \int dr \exp[-j\eta r] \int dl G(\xi - l, \eta, r) \Gamma(\xi - l, r) Q_\eta(l, \eta, r) = \\ &= \int dr \exp[-j\eta r] \left\{ Q_\eta(\xi, \eta, r) \otimes_\xi [G(\xi, \eta, r) \Gamma(\xi, r)] \right\}, \end{aligned} \quad (36)$$

where \otimes_ξ denotes the convolution along ξ . The second integral of eq.(36)

now shows the attractive feature to be a convolution which can be efficiently performed via standard multiplications in the non-transformed domain, see Fig. 9. However, we note (see again Fig. 9) that the η dependence of $Q_\eta(\cdot)$

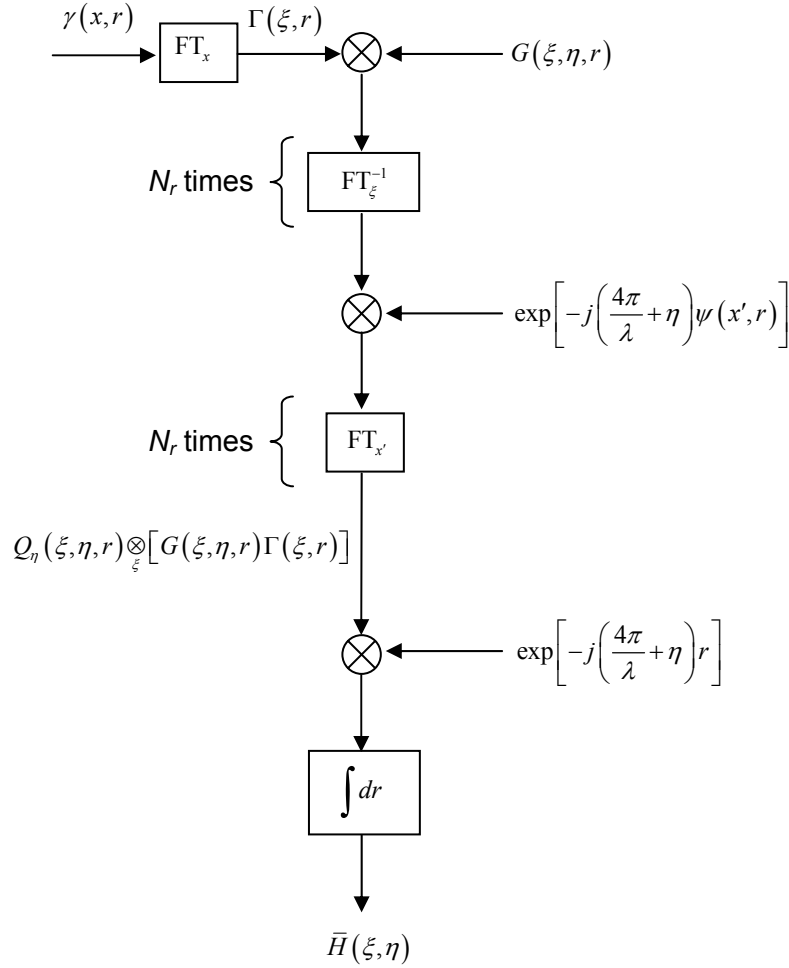


Figure 9 Block scheme of the method of Sect. 2.2.2 for the evaluation of $\bar{H}(\xi, \eta)$.

and $G(\cdot)$ implies that both the FT_ξ^{-1} and the $FT_{x'}$ steps, applied efficiently via FFT codes to $N_x \times N_r$ matrixes (N_x and N_r being the number of azimuth and range lines, respectively), must be performed N_r times. Evaluation of eq.(36) requires, at this stage, a multiplication by $\exp(-j\bar{\eta}r)$ and an additional integration along the r coordinate (see again Fig. 9) which cannot be efficiently carried out. Final evaluation of the SAR raw data in the presence of sensor trajectory displacements can now simply be performed along the scheme shown in Fig. 3.

We finally note that approximations made here are by far less stringent than those made in all the algorithms of motion compensation (see, e.g., [5], [6], [7]), so that the proposed simulation can be used to test such algorithms.

2.2.2.1 Simulation results

In this Section we present some examples aimed at assessing the validity of the approach proposed in the previous sub-Section and shown in Fig. 9. We consider the same typical X-band airborne SAR system of Sect.2.2.1.2, the main parameters of which are listed in Table I.

The platform is supposed to move along a trajectory that differs from the nominal straight line one by a time varying amount: its horizontal and vertical components are plotted in Fig. 10. We consider a portion of the sensor flight that corresponds to about two azimuth footprints, i.e., about 300 meters, corresponding to about 3 seconds at the sensor velocity of 100 m/s. We must note that this trajectory displacement is much more severe than the one analyzed in Fig. 4; in particular, the amplitude of the displacement is two orders of magnitude larger, and the frequency of the oscillations is considerably higher (four-five oscillations in 3 seconds of flight in this case, versus a fraction of oscillation considered in Fig. 4). Moreover, the track deviation of Fig. 10 is recognized also to be more severe than typical realistic airborne sensor displacements, especially with regard to the frequency of the oscillations. In any case, although so severe, such a track deviation satisfies condition (30) (which requires that $d_{\max} \ll 15$ m for the X-band SAR system of Table I) and, accordingly, it can be accounted for by the simulation approach of Fig. 9.

As an example, we consider a scene consisting of a single pointlike scatterer placed at near range ($r=4600$ m) over a completely absorbing background. For such a scene, consisting of a single scatterer, the SAR raw signal can be exactly computed directly in time domain, see Sect. 2.2.1.2. Accordingly, it is possible to compare the raw signal simulated via the approach described in Fig. 9 to the exact one. Range and azimuth cuts of the phase difference between simulated and exact raw signals are plotted in Figs. 11a and 11b, respectively. This phase error is limited to a few degrees for most part of the raw signal, and reaches 18 degrees (i.e., $\pi/10$ radians) only at its very edge. Additional considerations on Figs. 11a and 11b are now in order.

First of all, it must be noted that, similarly to the phase plots shown in Figs. 6a and 6b, most of the phase error of Figs. 11a and 11b is not due to the approximations involved in the simulation of the trajectory displacement effects, but it is simply caused by the asymptotic evaluation of the SAR

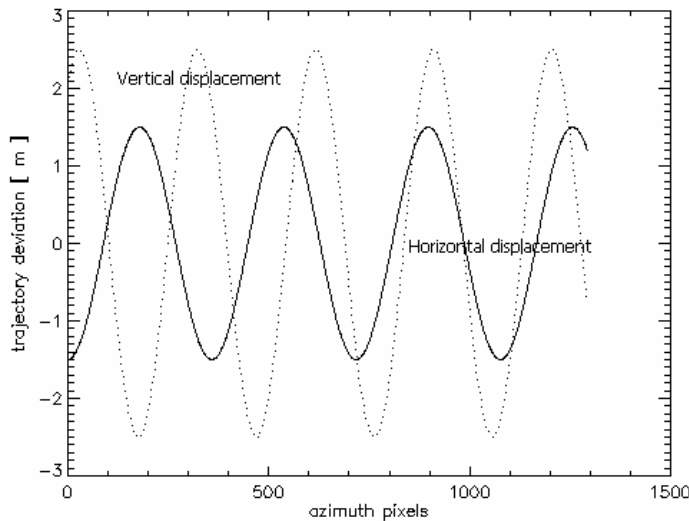
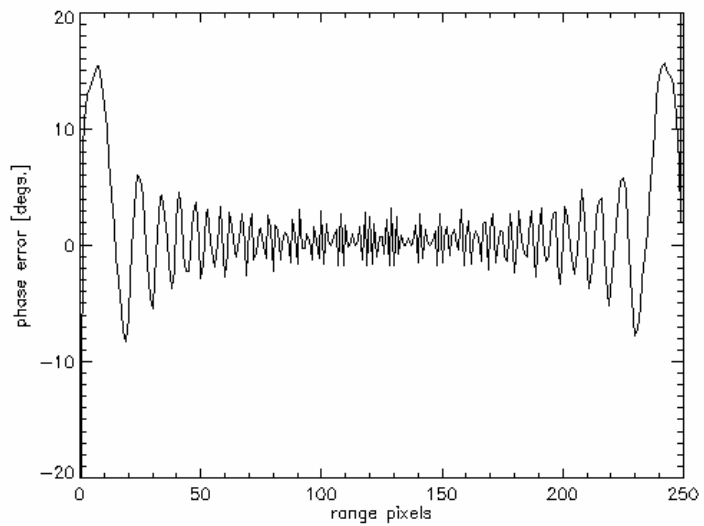
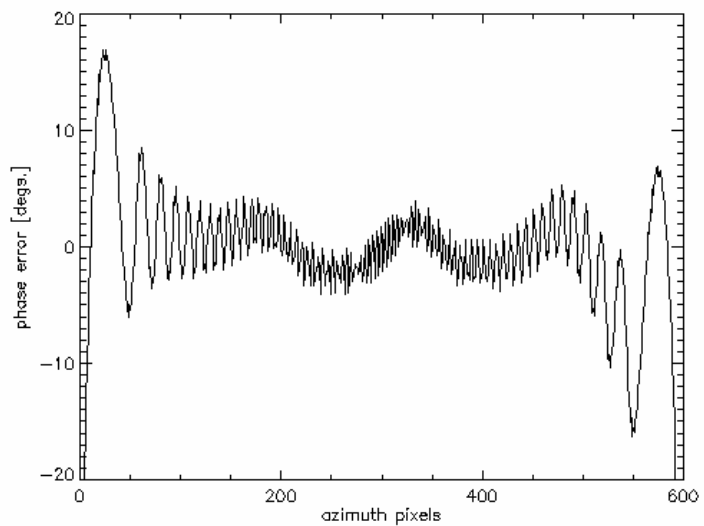


Figure 10 Simulated trajectory deviations relative to Figs. 11-13.

system transfer function via the stationary phase method, so that it would be present also in the ideal trajectory case. To better emphasize this point, we can consider, along the line shown in Sect. 2.2.1.2., the phase difference between the raw signal simulated in the presence of trajectory deviations and the raw signal simulated in the case of ideal trajectory: this difference can be then compared to the difference between the correspondent exact raw signals. In this way, we may evaluate the phase error almost completely “depurated” from the term due to the stationary phase approximation.

The range cut of this “depurated” phase error is confined between -1 and $+1$ degree, and the relative plot is not reported here for brevity. Conversely, the azimuth cut of this “depurated” phase error, plotted in Fig. 12a, shows an error larger than the one measured along the range direction. However, even in this more critical situation, the phase error is confined between -10 and $+1$ degree, which is certainly an acceptable value, especially considering that the error is much smaller than that for most part of the raw signal. It must also be noted that this error is due to the approximation of eq.(30). To verify this, in Fig. 12b we plot the graph of $[4\pi/\lambda]\varphi(x',x,r)$ for r and x coincident with the target location coordinates, for the system parameters of Table I and deviation of Fig. 10. Comparison of this plot with Fig. 12a confirms that the azimuth phase error plotted in Fig. 12a is due to the approximation of eq. (30).

**Figure 11a****Figure 11b**

Simulation method of Fig. 9 in the presence of the track deviations of Fig. 10: range (a) and azimuth (b) cuts of the overall phase error for a target located at the near range, at $r=4600$ m. The Figures refers to the same window considered in Fig. 5.

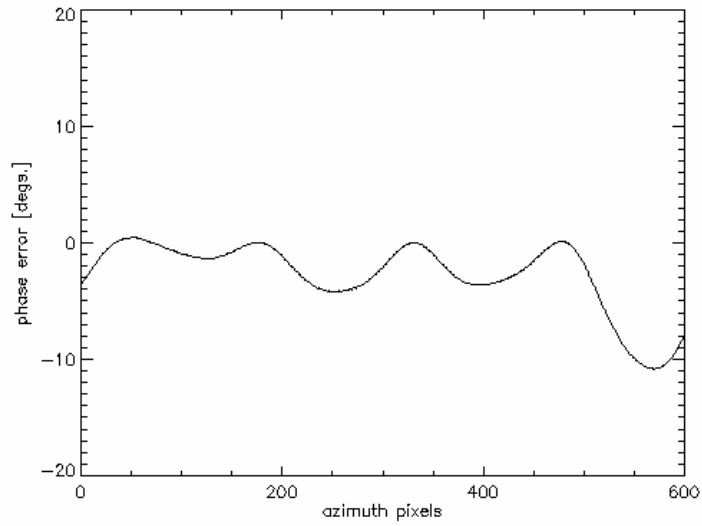


Figure 12a As Fig. 6b, but after removing the aberrations induced by the stationary phase method (see the body of the paper).

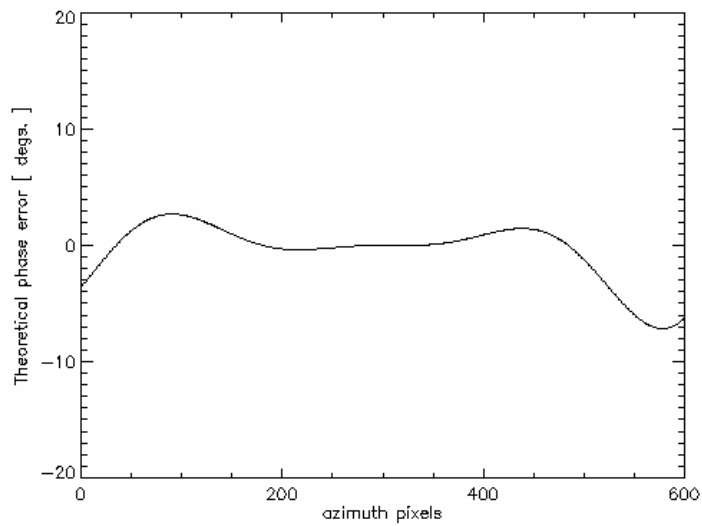


Figure 12b Expected phase error along the azimuth direction for the target considered in Fig. 12a according to eq.(30).

As a final remark, we note that, differently from the validation experiments shown in Sect. 2.2.1.2., results similar to those shown in Fig. 11 are obtained also when targets located at different range coordinate (included the midrange) are considered: this is due to the fact that the simulation scheme described in Section 2.2.2, and shown in Fig. 9, properly accounts for the range variance of displacement effects; accordingly, the accuracy of the obtained SAR raw data does not change along the range direction.

2.2.3 Narrow azimuth beam and moderate deviation velocity

In order to improve the computational efficiency of the simulation algorithm discussed in section 2.2.2. and shown in Fig. 9, we explore in the following the possibility to remove the η dependence from the terms involved in the FT operations of Fig. 9. To this end, let us now consider the following approximation of eq.(33):

$$\bar{f}(x, x', \eta, r) \approx \gamma(x, r) \exp \left\{ -j \frac{4\pi}{\lambda} \psi(x', r) \right\} \quad (37)$$

which holds when:

$$\left| \left(\eta + \frac{4\pi}{\lambda} \right) \varphi(x, x', r) + \eta \psi(x', r) \right| \ll 1 \quad (38)$$

that, in addition to the condition of eq. (30) (equivalent to eq. (24)), requires that we enforce also condition (31) (equivalent to eq.(25)).

Similarly to the case discussed in Sect. 2.2.2, again the $\bar{f}(\cdot)$ function can be factorized in two terms which depend separately by the x and x' variables so that eq.(34) can be rearranged as follows:

$$\bar{F}(\chi, l, \eta, r) = \Gamma(\chi, r) Q(l, r) \quad (39)$$

where $Q(\cdot)$ is now given by:

$$Q(l, r) = \text{FT}_{x'} \left\{ \exp \left[-j \frac{4\pi}{\lambda} \psi(x', r) \right] \right\} \quad (40)$$

thus not showing any dependence on η differently from eq.(35). Accordingly:

$$\begin{aligned}\bar{H}(\xi, \eta) &= \int dr \exp[-j\bar{\eta}r] \int dl G(\xi-l, \eta, r) \Gamma(\xi-l, r) Q(l, r) = \\ &= \int dr \exp[-j\bar{\eta}r] \left\{ Q(\xi, r) \otimes_{\xi} [G(\xi, \eta, r) \Gamma(\xi, r)] \right\}.\end{aligned}\quad (41)$$

We observe that, at this point, the efficiency of the simulation procedure has not been improved, because of the η dependence of the $G(\cdot)$ function inside the convolution product of eq.(41); accordingly no advantages, in terms of computational efficiency, seem to be related to the approximation (37). However, we can separate the SAR STF in two different contributions:

$$G(\xi, \eta, r) = G_A(\xi, r) \cdot G_B(\xi, \eta, r) \quad (42)$$

where:

$$G_A(\xi, r) = w\left(\frac{\xi}{\Omega_x}\right) \cdot \exp\left[-j\left(\sqrt{\left(\frac{4\pi}{\lambda}\right)^2 - \xi^2} - \frac{4\pi}{\lambda}\right)r\right] \quad (43)$$

accounts for the azimuth frequency modulation including the focus depth effect and:

$$\begin{aligned}G_B(\xi, \eta, r) &= \text{rect}\left[\frac{\eta}{\Omega_r}\right] w\left(\frac{\xi}{\Omega_x}\right) \cdot \exp\left[j\frac{\eta^2}{4b}\right] \cdot \\ &\cdot \exp\left[-j\left(\sqrt{\bar{\eta}^2 - \xi^2} - \bar{\eta}\right)r\right] \exp\left[j\left(\sqrt{\left(\frac{4\pi}{\lambda}\right)^2 - \xi^2} - \frac{4\pi}{\lambda}\right)r\right]\end{aligned}\quad (44)$$

describes the Range Cell Migration effect. Let us observe that the spectral convolution of eq.(41) can be rendered not dependent on η when the spectral extension of $Q(\xi, r)$ along the ξ coordinate is small enough to consider the η -dependent $G_B(\cdot)$ function constant inside the azimuth band of $Q(\xi, r)$; in this case eq.(41) simplifies as follows [5]:

$$\begin{aligned}\bar{H}(\xi, \eta) &= \int dr \exp[-j\bar{\eta}r] \int dl G_A(\xi-l, r) G_B(\xi-l, \eta, r) \Gamma(\xi-l, r) Q(l, r) \\ &\approx \int dr \exp[-j\bar{\eta}r] G_B(\xi, \eta, r) \int dl G_A(\xi-l, r) \Gamma(\xi-l, r) Q(l, r) = \\ &= \int dr \exp[-j\bar{\eta}r] G_B(\xi, \eta, r) \left\{ Q(\xi, r) \otimes_{\xi} [G_A(\xi, r) \Gamma(\xi, r)] \right\}.\end{aligned}\quad (45)$$

Evaluation of eq.(45) again requires a convolution to be performed: this can be efficiently carried out, as in the previous Section, via standard multiplications in the non-transformed domain (see Fig. 13). However, we note that the elimination of the η dependence on both the $Q(\cdot)$ and the $G_A(\cdot)$ functions implies that both the FT_ξ^{-1} and the $FT_{x'}$ steps have to be performed only once (differently from the procedure described in the previous Section and shown in Fig. 9). Evaluation of eq. (45) requires, in addition, a multiplication by $G_B(\xi, \eta, r) \exp(-j\eta r)$ and an integration along the r coordinate (see again Fig. 13) which, similarly to the case analyzed in the previous Section, cannot be efficiently carried out. Final evaluation of the SAR raw data in the presence of sensor trajectory displacements can now be simply performed along the scheme shown in Fig. 3.

Some considerations about eq. (45) and its validity limits are now in order.

First of all we underline that the adopted approximation for $G_B(\cdot)$ cannot be easily extended to $G_A(\cdot)$, which oscillates much more rapidly. In order to clarify this point let us analyze the spectral behavior of the terms (43) and (44) using, but only for the sake of simplicity, their second order expansion around $\xi=0$ and first order expansion around $\eta=0$ (see TF approximations shown in Chapter 1, eqs. (46) and (52)):

$$G_A(\xi, r) \approx w\left(\frac{\xi}{\Omega_x}\right) \cdot \exp\left[j\frac{\xi^2}{2} \frac{\lambda r}{4\pi}\right], \quad (46)$$

$$G_B(\xi, \eta, r) \approx \text{rect}\left[\frac{\eta}{\Omega_r}\right] w\left(\frac{\xi}{\Omega_x}\right) \cdot \exp\left[j\frac{\eta^2}{4b}\right] \exp\left[-j\frac{\xi^2}{2} \frac{\lambda r}{4\pi} \frac{\eta\lambda}{4\pi}\right]. \quad (47)$$

Since $|\eta\lambda/4\pi| \ll 1$, see Chapter 1, eq.(107), it is clear that $G_B(\cdot)$ shows a slower variant behavior along ξ with respect to $G_A(\cdot)$; accordingly, it is more difficult to consider $G_A(\cdot)$ constant within the azimuth bandwidth of $Q(\xi, r)$.

We also stress that the simulation approach described in Fig. 3 is of fundamental importance for the applicability of the efficient simulation scheme of Fig. 13. In order to clarify this point, let us note that the absence of the term $\exp[-j(4\pi/\lambda + \eta)\delta r(x')]$ in eq.(21) and, accordingly, in eqs.(37) and (40), on one side allows us to obtain an η independent $Q(\cdot)$ function, and on the other side causes a reduction of the azimuth bandwidth Ω_Q , thus rendering less critical the approximation (45).

With regard to the azimuth bandwidth Ω_Q of $Q(\xi, r)$, we underline that its extension has a great impact on the approximation (45): the smaller the

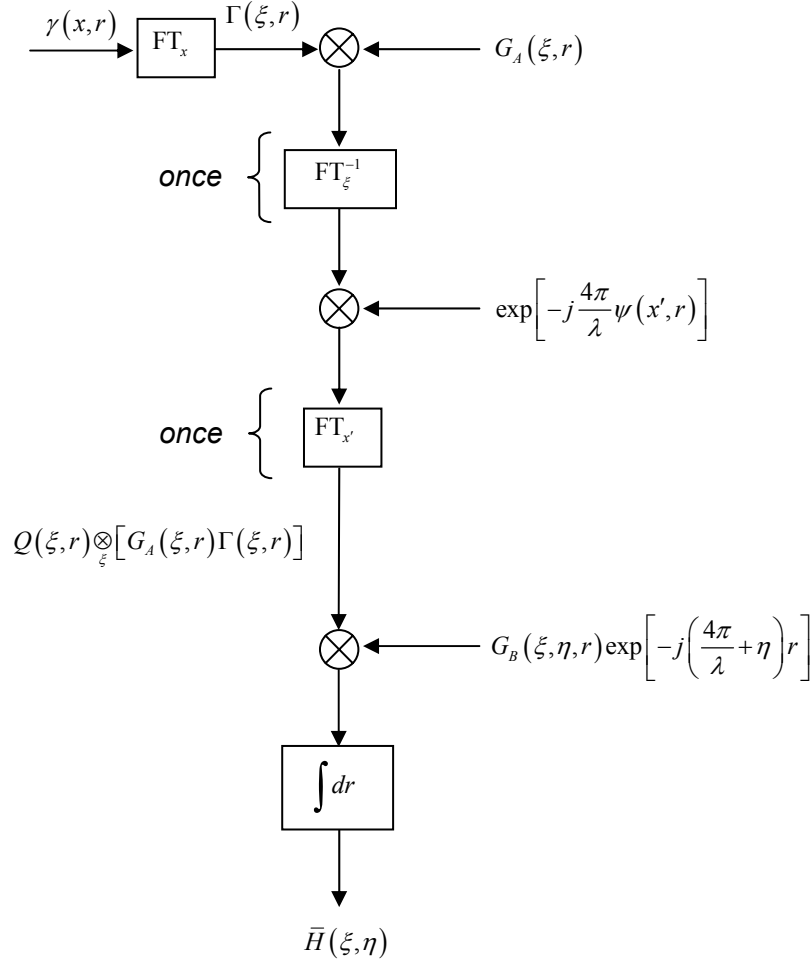


Figure 13 Block scheme of the method of Sect.2.2.3 for the evaluation of $\bar{H}(\xi, \eta)$.

bandwidth the sounder the approximation. According to the *Carson's rule* [16] we have:

$$\Omega_Q(r) = \Omega_\psi \left[\frac{4\pi}{\lambda} |\psi(x', r)|_{\max} + 1 \right] \quad (48)$$

where Ω_ψ is the azimuth bandwidth of $\psi(x', r)$ (which is approximately coincident with the spatial bandwidth Ω_d of the sensor displacement) and $|\psi(x', r)|_{\max}$ represents the maximum amplitude of $\psi(x', r)$ with respect to x' . Accordingly, we observe that approximation (45) holds both for low

frequency airborne deviations, i.e, for small values of Ω_ψ , and for moderate residual range variant amplitude deviation, i.e, for small values of $|\psi(\cdot)|_{\max}$. Furthermore, we observe that $|\psi(x',r)|$ is 0 for $r=r_0$ and increases when the difference $|r-r_0|$ grows up; accordingly, we can state that the approximation (45) is less critical for narrow range beam systems. These qualitative considerations are quantitatively supported by the analysis of Appendix IV, which shows that eq.(45) can be safely used if

$$d_{\max} \ll \frac{2L_r}{\Omega_d X} \frac{f}{\Delta f} . \quad (49)$$

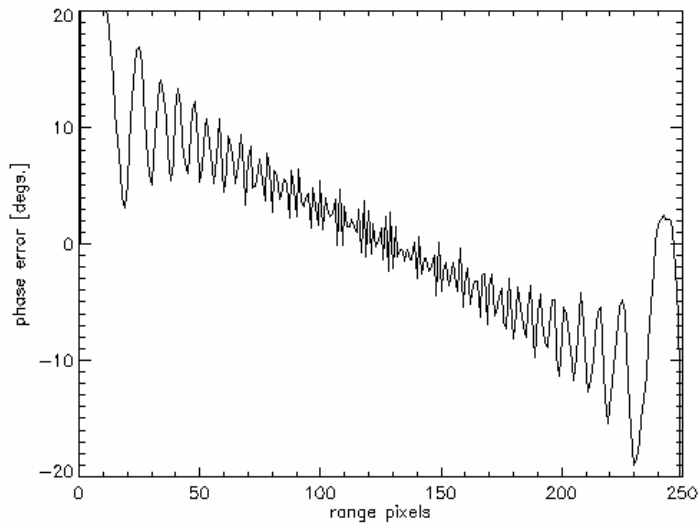
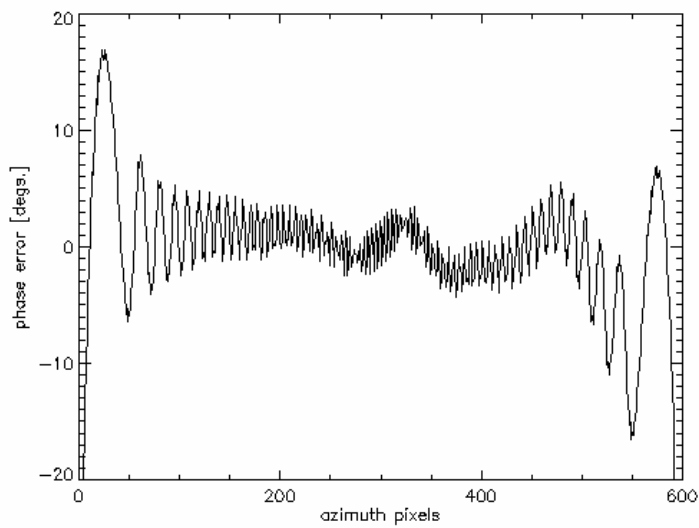
Condition (49) is less stringent, by a factor of about $f/\Delta f$, than condition (32): this means that the present method, although less general than the method of Sect. 2.2.2, has a much wider range of validity than the one described in Sect. 2.2.1.

2.2.3.1 Simulation results

In this Section we present some examples aimed at assessing the validity of the approach proposed in the previous sub-Section and shown in Fig. 13. As usual, we consider the same typical X-band airborne SAR system of Table I. Same scene and track deviation of Figs. 10-12 are considered, but the simulation approach of Fig. 13 is now implemented.

Range and azimuth cuts of the corresponding overall phase error are reported in Figs. 14a and 14b, respectively. While the azimuth cut is very similar to that plotted in Fig. 11b, the range cut in this case clearly shows the presence of a non-negligible phase ramp, the origin of which is now discussed.

As already noted, correct implementation of the simulation scheme described in Sect. 2.2.3 requires conditions (31) (equivalent to eq.(25)), and (49) to be fulfilled, that is, for the X-band SAR sensor of Table I, $d_{\max} \ll 8\text{m}$ and $\Omega_d \cdot d_{\max} \ll 0.24$. It is clear that such conditions are not well satisfied by the sensor track deviation considered in Fig. 10. In particular, when condition (31) is not fulfilled, the term $\eta \cdot \psi(x',r)$ becomes not negligible in eq.(21), which, accordingly, cannot be well approximated by (37). It is easy to show that the presence of such an η -dependent phase term in the (x',η) domain corresponds, in the spatial (x',r') domain, to a range shift of the SAR raw data equal to $\psi(x',r)$. As a consequence, when the simulation scheme described in Sect 2.2.3 is applied, a range shift between simulated and exact raw signals is expected; moreover, since the range-variant term $\psi(x',r)$ of the displacement is zero at the scene center, and increases as we move away from the scene center, see considerations in connection with eq.(15), it is

**Figure 14a****Figure 14b**

As Fig. 11, but when the simulation method of Fig. 13 is applied.

clear that this effect becomes stronger as we move away from the midrange. In the case of the trajectory displacement of Fig. 10, such a range shift is not negligible for the considered target (located at near range), and it produces the range phase ramp of Fig. 14a. Obviously, this effect vanishes when a track deviation fulfilling conditions (31) and (49) is considered.

To show this, let us apply the simulation scheme described in Sect. 2.2.3 and shown in Fig. 13 to the same scene considered above, consisting of a single pointlike scatterer placed at near range ($r=4600$ m) over a completely absorbing background, but in the presence of the track deviation depicted in Fig. 15. Range and azimuth cuts of the corresponding overall phase error are reported in Figs. 16a and 16b, respectively. In this case, the range phase ramp is almost completely vanished, and this is certainly not surprising, since condition (31) is satisfied, so that $\psi(x',r)$ is now much smaller than the range resolution also for the considered target located at near range. Moreover, also the azimuth cut shows an error smaller than that shown in Fig. 14b. This is certainly expected, since such an azimuth phase error is almost completely due, as already noted, to the approximation of eq.(30), satisfied by the track deviation of Fig. 15 better than by that of Fig. 10. To better emphasize this, we plot in Fig. 17a the azimuth cut of the “depurated” phase error, and in Fig. 17b the graph of $[4\pi/\lambda]\varphi(x',x,r)$ calculated for r and

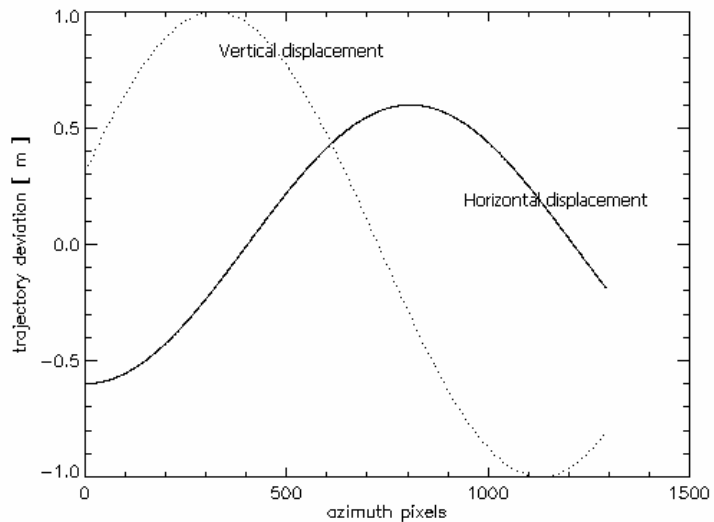
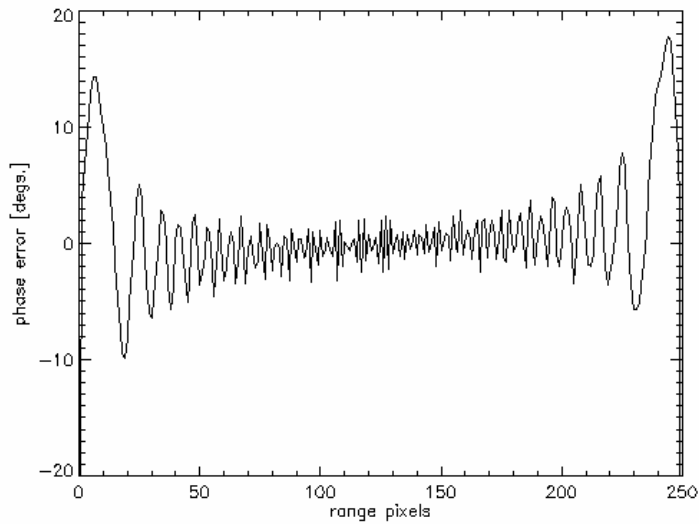
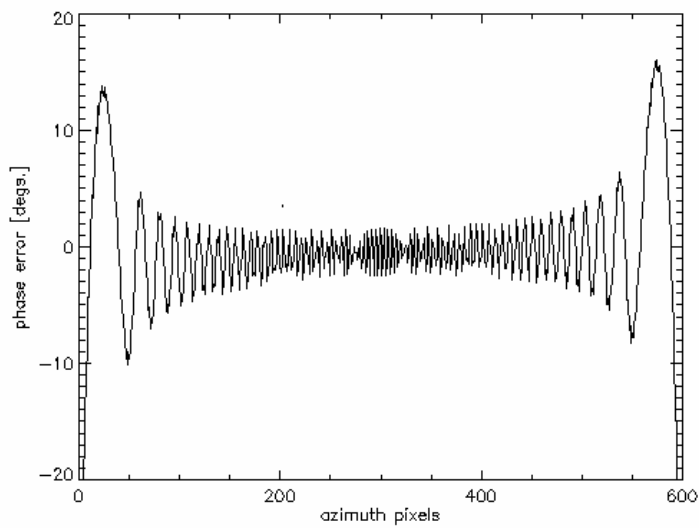


Figure 15 Simulated trajectory deviations relative to Figs. 16-18.

**Figure 16a****Figure 16b**

Simulation method of Fig. 13 in the presence of the track deviations of Fig. 15: range (a) and azimuth (b) cuts of the overall phase error for a target located at the near range, at $r=4600$ m. As usual, the Figure refers to the same window considered in Fig. 5.

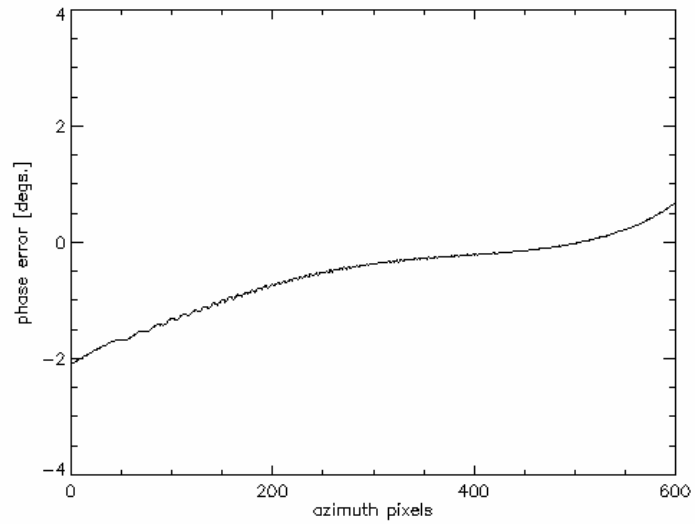


Figure 17a As Fig. 16b, but after removing the aberrations induced by the stationary phase method (see the body of the paper).

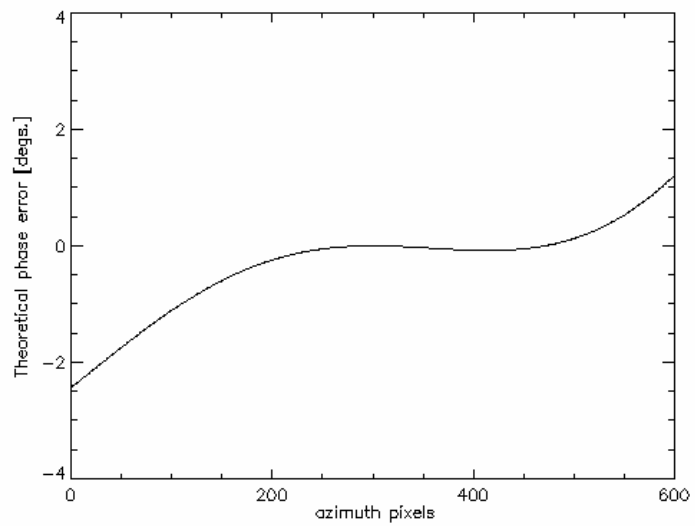


Figure 17b Expected phase error along the azimuth direction for the target considered in Fig. 17a according to eq.(30).

x coincident with the target location coordinates, for the system parameters of Table I and for the deviation of Fig. 15. Comparison of Figs. 17a and 17b confirms that the azimuth phase error plotted in Fig. 17a is due to the approximation of eq. (30); moreover, comparison of Figs. 12b and 17b (note that a different scale is adopted in two plots) shows how much the approximation of eq. (30) is better satisfied by the track deviation of Fig. 15 than by that of Fig. 10.

Finally, in order to give an example of the simulation scheme efficiency, we simulated, via the approach described in 2.2.3, the raw signal corresponding to an extended scene, the height profile of which is a pyramid, acquired by the SAR system of Table I in the presence of the trajectory displacement of Fig. 15. Simulation of this 830 by 1941 pixel raw signal took 5 minutes on a 1 GHz Pentium IV PC. Final images obtained by processing the simulated raw signal, without and with the motion compensation procedure of [5], are reported in Figs. 18a and 18b, respectively. It is clear that in this case proper motion compensation procedure is required to avoid appearance of strong azimuth focusing losses, in total agreement with the analysis of [5].

Finally we observe that similar results are obtained, but not reported here for brevity, by considering the simulation scheme described in 2.2.2 and shown in Fig. 9: in this case simulation of this 830 by 1941 pixel raw signal took 30 minutes on a 1 GHz Pentium IV PC.

2.2.4 Computational efficiency

Let us now evaluate the computational complexity of the methods described above. We assume that N_x and N_r are the azimuth and range dimensions (in pixels) of the final raw signal, and recall that the computational complexity of the evaluation of the reflectivity function $\chi(x,r)$ is of the order of $N_x \cdot N_r$ and is the same for all the simulation methods. By analyzing Figs. 3 and 9 it is easy to realize that the number N_1 of complex multiplications needed to simulate the raw signal by the method of Sect.2.2.2 is:

$$\begin{aligned} N_1 &\approx N_x N_r^2 (2 + \log_2 N_x) + N_x N_r \left(1 + \log_2 N_x + \frac{1}{2} \log_2 N_r \right) \approx \\ &\approx N_x N_r^2 (2 + \log_2 N_x) \end{aligned} \quad (50)$$

whereas, by analyzing Figs. 3 and 13, the number N_2 of complex multiplications needed to simulate the raw signal by the method of Sect.2.2.3 turns out to be:

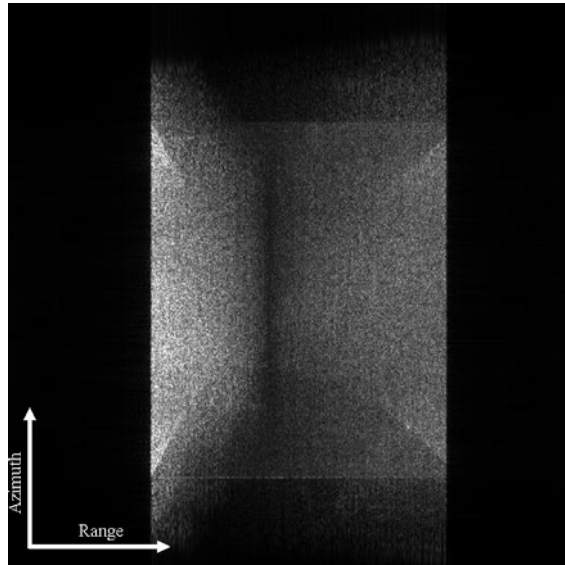


Figure 18a

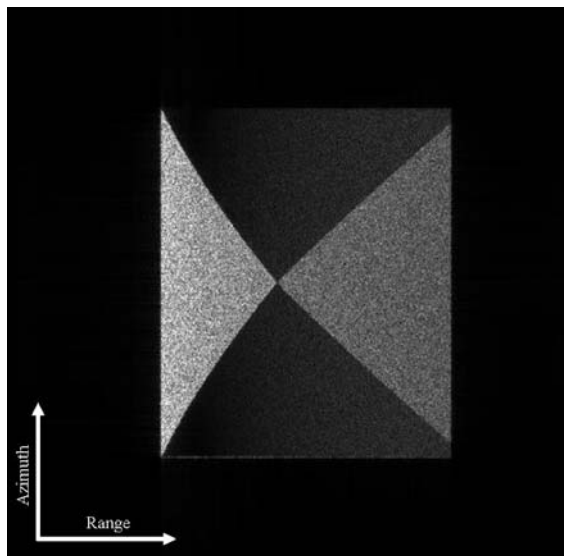


Figure 18b Simulation method of Fig. 13 in the presence of the track deviations of Fig. 15: multi-look image of a pyramid, obtained by processing the SAR raw signal acquired by the sensor of Table I. A 8 azimuth x 4 range pixel averaging window has been used to perform the multilook operation. (a) No motion compensation has been applied. (b) Proper motion compensation has been applied.

$$N_2 \approx N_x N_r^2 + N_x N_r \left(3 + 2 \log_2 N_x + \frac{1}{2} \log_2 N_r \right) \approx N_x N_r^2 \quad . \quad (51)$$

Accordingly, a computational time saving of the order of $2 + \log_2 N_x$ can be obtained by using the method of Sect.2.2.3 with respect to using the method of Sect.2.2.2.

It is instructive to compare N_1 and N_2 to the number of complex multiplications needed by a full 2-D time domain approach, N_{TD} , and a full 2-D Fourier domain approach, N_{FD} . It is not difficult to verify that [1]:

$$N_{TD} \approx N_x^2 N_r^2 \quad (52)$$

and

$$N_{FD} \approx N_x N_r (1 + \log_2 N_x N_r) \quad . \quad (53)$$

It is then clear that the methods shown in Sects. 2.2.2-3 are much more time consuming than the full 2-D Fourier domain one of Sects. 2.2.1, but they are still much more computationally efficient than the time domain one: the computational time saving is of the order of N_x , i.e., of the order of thousands, and this makes the simulation of extended scenes possible in a reasonable time. Note that the methods of Sects. 2.2.2-3 have a much larger range of validity with respect to the full 2-D Fourier domain one of Sect. 2.2.1

2.3 Summary

In this Chapter the problem of efficient extended scene SAR raw signal simulation accounting for sensor deviations from the ideal, straight line trajectory is addressed. Use of a Fourier Domain approach exploiting the efficiency of FFT codes is explored. To this aim, a general and compact Fourier Domain formulation of the SAR raw signal in the presence of arbitrary trajectory deviations is obtained.

However, it is shown that such a formulation cannot be efficiently implemented unless a narrow beam and slow trajectory deviation assumption is made. In the latter case, a full 2-D Fourier domain simulation can be used. This approach can be applied only to some SAR systems and/or trajectory deviations, but it has the advantage that processing time is practically not increased with respect to the nominal trajectory case.

This range of validity can be extended, at the expense of processing time, via a 1-D azimuth Fourier domain processing followed by a range time domain integration. This approach is less efficient than the 2-D Fourier domain one, but it only requires some reasonable assumptions on the sensor motion and on the SAR system features, so that, at variance with the 2-D Fourier domain one, it can be safely used for most airborne SAR systems. In addition, it turns out to be still much more efficient than the time domain one, so that extended scenes can still be considered.

Validity limits of the proposed approaches are analytically evaluated, and the effectiveness of the proposed simulation schemes is verified by some simulation examples.

Effectiveness of the simulator is verified by comparing simulated raw signal corresponding to a single scattering point to the corresponding available time domain exact expression. Examples of extended scene simulation in the presence of trajectory deviations are also provided.

APPENDIX I

Let us consider the Fourier transform of eq.(4) along r' :

$$H(x', \eta) = \iint dx dr \gamma(x, r) w^2 \left(\frac{x' - x}{X} \right) \exp \left[-j \frac{4\pi}{\lambda} R \right] \int dr' \text{rect} \left[\frac{r' - R}{\tau c / 2} \right] \exp \left[-j \frac{2\alpha}{c^2} (r' - R)^2 \right] \exp[-j\eta r'] \quad (54)$$

Letting $r' - R = q$, we obtain:

$$H(x', \eta) = \iint dx dr \gamma(x, r) w^2 \left(\frac{x' - x}{X} \right) \exp \left[-j \left(\eta + \frac{4\pi}{\lambda} \right) R \right] \int dr' \text{rect} \left[\frac{q}{\tau c / 2} \right] \exp \left[-j \frac{2\alpha}{c^2} (q)^2 \right] \exp[-j\eta q] \quad (55)$$

Solution of the last integral in eq.(55) has been addressed in Chapter 1 (see eq.(99) in Appendix I and consider the following substitution: $\bar{q} = 2q/c\tau$) and easily leads to the expression (6).

APPENDIX II

Let us consider eq. (6). The expression of its FT along the azimuth direction is the following:

$$H(\xi, \eta) = \text{rect} \left[\frac{\eta}{\Omega_r} \right] \exp \left[j \frac{\eta^2}{4b} \right] \cdot \int dr \exp[-j\bar{\eta}r] \times \iint dx dx' \gamma(x, r) w^2(x' - x) \cdot \exp[-j\xi x'] \times \exp \left[-j\bar{\eta} (\Delta R(x' - x, r) + \delta R(x', x, r)) \right] \quad (56)$$

where, as usual $\bar{\eta} = \eta + 4\pi/\lambda$, The last double integral can be rearranged as follows:

$$\int dx \int dx' f(x, x', \eta, r) \cdot g_1(x' - x, \eta, r) \exp[-j\xi x'] = \int dx \left[F_1(x, \xi, \eta, r) \otimes_{\xi} \{ G_1(\xi, \eta, r) \exp[-j\xi x] \} \right], \quad (57)$$

where \otimes_{ξ} denotes the convolution along ξ , $f(x, x', \eta, r)$ is given by eq. (9) and:

$$F_1(x, \xi, \eta, r) = \int dx' f(x, x', \eta, r) \cdot \exp(-j\xi x') = FT_{x'} [f(x, x', \eta, r)] \quad (58)$$

$$g_1(x' - x, \eta, r) = w^2 \left(\frac{x' - x}{X} \right) \exp \left[-j \left(\eta + \frac{4\pi}{\lambda} \right) \Delta R(x' - x, r) \right] \quad (59)$$

$$G_1(\xi, \eta, r) = \int dx' g_1(x', \eta, r) \cdot \exp(-j\xi x') = FT_{x'} [g_1(x', \eta, r)] \quad (60)$$

The expression of $G_1(\cdot)$ coincides (after proper variable changes) to the integral (104) in Chapter 1, Appendix I, the solution of which is given by:

$$G_1(\xi, \eta, r) = w^2 \left(\frac{\xi}{\Omega_x} \right) \cdot \exp \left[-j \left(\sqrt{\eta^2 - \xi^2} - \bar{\eta} \right) r \right] \quad (61)$$

where, as usual, Ω_x is the SAR system azimuth bandwidth (see Chapter 1, eq. (30)).

Eq.(57) can be rewritten as follows:

$$\begin{aligned} \iint dx dl F_1(x, l, \eta, r) G_1(\xi - l, \eta, r) \exp[-j(\xi - l)x] = \\ \int dl G_1(\xi - l, \eta, r) \int dx F_1(x, l, \eta, r) \exp[-j(\xi - l)x] = \\ \int dl G_1(\xi - l, \eta, r) F(\xi - l, l, \eta, r) \end{aligned} \quad (62)$$

where:

$$F(\chi, l, \eta, r) = FT_x [F_1(x, l, \eta, r)] = \int dx F_1(x, l, \eta, r) \cdot \exp(-j\chi x) \quad (63)$$

which, by using eq.(58) with the variable change $l \rightarrow \xi$, gives eq.(8).

Accordingly, replacing the last double integral of eq.(56) with eq.(62), we obtain the general expression, eq.(7), of the raw data spectrum in the presence of sensor trajectory displacements, that we report here again:

$$H(\xi, \eta) = \int dr \exp[-j\bar{\eta}r] \int dl G(\xi - l, \eta, r) F(\xi - l, l, \eta, r) \quad (64)$$

where:

$$G(\xi, \eta, r) = \text{rect} \left[\frac{\eta}{\Omega_r} \right] \exp \left[j \frac{\eta^2}{4b} \right] \cdot G_1(\xi, \eta, r) \quad (65)$$

which is coincident with eq.(10).

APPENDIX III

In this Appendix we express $\varphi(x', x, r)$ and $\psi(x', r)$ in terms of SAR system parameters, in order to express conditions (24)-(26) in a more convenient form, i.e., in the form of eqs.(30)-(32).

By comparing eq.(14) with the following relation

$$\begin{aligned} \delta R(x', x, r) &\approx \left. \frac{\partial R}{\partial \delta r_{xr}} \right|_{\delta r_{xr}=0} \delta r_{xr} = \frac{r}{R_n} \delta r_{xr} \approx \delta r_{xr}(x', x, r) - \frac{(x' - x)^2}{2r^2} \delta r_{xr}(x', x, r) = \\ &= \delta r_r(x', r) + \delta r_{xr}(x', x, r) - \delta r_r(x', r) - \frac{(x' - x)^2}{2r^2} \delta r_{xr}(x', x, r) \end{aligned} \quad (66)$$

we get

$$\varphi(x', x, r) \approx \delta r_{xr}(x', x, r) - \delta r_r(x', r) - \frac{(x' - x)^2}{2r^2} \delta r_{xr}(x', x, r) \quad (67)$$

in addition, we can write

$$\begin{aligned} \delta r_{xr}(x', x, r) - \delta r_r(x', r) &\approx \left. \frac{\partial \delta r_{xr}}{\partial \vartheta} \right|_{\vartheta=\vartheta(x', r)} [\vartheta(x, r) - \vartheta(x', r)] = \\ &= -d(x') \cos[\vartheta(x', r) - \beta(x')] [\vartheta(x, r) - \vartheta(x', r)] \end{aligned} \quad (68)$$

and

$$\vartheta(x, r) - \vartheta(x', r) \approx \left. \frac{\partial \vartheta(x, r)}{\partial z} \right|_{z=z(x', r)} \cdot [z(x, r) - z(x', r)] \quad (69)$$

with

$$\cos[\vartheta(x, r)] = \frac{h - z(x, r)}{r} \Rightarrow \left. \frac{\partial \vartheta(x, r)}{\partial z} \right|_{z=z(x', r)} = \frac{1}{r \sin[\vartheta(x', r)]} \quad (70)$$

so that

$$\delta r_{xr}(x', x, r) - \delta r_r(x', r) \approx \frac{-d(x') \cos[\vartheta(x', r) - \beta(x')]}{r \sin[\vartheta(x', r)]} [z(x, r) - z(x', r)] \quad (71)$$

Accordingly, we have:

$$|\varphi(x', x, r)| < \frac{d_{\max} |\cos[\vartheta(x', r) - \beta(x')]|}{r \sin[\vartheta(x', r)]} \Delta z_{\max} + \frac{X^2}{8r^2} d_{\max} \quad (72)$$

where Δz_{\max} is the maximum terrain height variation within an azimuth footprint, the estimate of which may be taken equal to the height macroscopic profile mean slope (α_i) times the azimuth half footprint $X/2$; hence, condition (24) becomes:

$$d_{\max} \ll \frac{\lambda r}{2\pi X \alpha_i} \approx \frac{L}{2\pi \alpha_i} \quad \text{and} \quad d_{\max} \ll \frac{2L^2}{\pi \lambda} \approx \frac{L}{\lambda} \cdot \frac{L}{2} \quad (73)$$

where the first condition is dominant for mountainous areas, while the second is dominant for flat or gently sloped areas and is coincident with inequality (30).

Let us now move to consider the term $\psi(x', r)$. From (15) and (3) we have

$$\begin{aligned} \psi(x', r) &= \delta r_r(x', r) - \delta r(x') \approx -d(x') \sin[\vartheta(x', r) - \beta(x')] + \\ &\quad + d(x') \sin[\vartheta(x', r_0) - \beta(x')] \approx \\ &\quad \approx -d(x') \cos[\vartheta(x', r_0) - \beta(x')] [\vartheta(x, r) - \vartheta(x', r_0)] \end{aligned} \quad (74)$$

Accordingly,

$$|\psi(x', r)| < d_{\max} \frac{\Delta \vartheta_{\max}}{2} = d_{\max} \frac{\lambda}{2L_r} = \psi_{\max} \quad (75)$$

so that condition (25) becomes eq.(31).

With regard to condition (26), we have to separately analyze the cases of fast and slow trajectory deviations. In the former case, the displacement spatial bandwidth Ω_d is of the same order of the inverse of the azimuth footprint ($\Omega_d \approx 1/X$) and more than one oscillation is completed within a synthetic aperture length, so that condition (26) implies that $|\psi(x', r)| \ll \lambda/4\pi$, i.e.:

$$d_{\max} \ll \frac{L_r}{2\pi} \quad . \quad (76)$$

In the slow deviation case, the displacement spatial bandwidth Ω_d is much smaller than the inverse of the azimuth footprint ($\Omega_d \ll 1/X$), and we can write:

$$|\psi(x', r) - \psi(x, r)| \cong \left| \frac{\partial \psi}{\partial x'} \right|_{x'=x} (x' - x) < \Omega_d \psi_{\max} \frac{X}{2} \quad . \quad (77)$$

Using eqs.(77) and (75), condition (26) becomes

$$d_{\max} \ll \frac{L_r}{\pi \Omega_d X} \quad . \quad (78)$$

By summarizing the last results, we have that condition (26) is verified for

$$\begin{cases} d_{\max} \ll \frac{L_r}{2\pi} & \text{if } \Omega_d \approx \frac{1}{X} \\ d_{\max} \ll \frac{L_r}{\pi \Omega_d X} & \text{if } \Omega_d \ll \frac{1}{X} \end{cases} \quad . \quad (79)$$

It is clear that conditions reported in (79) can be merged in a single condition, i.e., eq.(32).

APPENDIX IV

Equation (45) holds if the minimum period T_ξ of the oscillations of $G_B(\xi, \eta, r)$ (with ξ varying and r and η fixed), i.e., see (47), of

$$w\left(\frac{\xi}{\Omega_x}\right) \cdot \exp\left[-j \frac{\xi^2}{2} \frac{\lambda r}{4\pi} \frac{\eta \lambda}{4\pi}\right] \quad , \quad (80)$$

is much larger than the azimuth bandwidth Ω_Q of $Q(\cdot)$:

$$T_\xi \gg \Omega_Q \quad , \quad \text{i.e.,} \quad \frac{2\pi}{\Omega_\xi} \gg \Omega_Q \quad , \quad \text{i.e.,} \quad \Omega_Q \Omega_\xi \ll 2\pi \quad . \quad (81)$$

In the relations above, Ω_ξ is the maximum angular frequency of the oscillations of $G_B(\xi, \eta, r)$, and can be evaluated as follows:

$$\Omega_\xi = \frac{\lambda r}{4\pi} \frac{\eta\lambda}{4\pi} \Omega_x < \frac{\lambda r}{4\pi} \frac{\lambda}{4\pi} \frac{bc\tau}{2} \frac{4\pi}{L} = \frac{\lambda r}{2L} \frac{\Delta f}{f} = \frac{X}{2} \frac{\Delta f}{f} \quad (82)$$

where use has been made of (47).

With regard to the azimuth bandwidth Ω_Q of $Q(\cdot)$, it can be evaluated by using the Carson's rule [16]; and using eq.(53)

$$\Omega_Q = \Omega_\psi \left[\frac{4\pi}{\lambda} \psi_{\max} + 1 \right] = \Omega_d \left[2\pi \frac{d_{\max}}{L_r} + 1 \right] . \quad (83)$$

Use of (82) and (83) in (81) leads to the condition

$$\frac{X}{2} \frac{\Delta f}{f} \Omega_d \left[2\pi \frac{d_{\max}}{L_r} + 1 \right] \ll 2\pi . \quad (84)$$

It is easy to verify that condition (84) is certainly verified if at least one of the two following conditions is satisfied:

$$\left\{ \begin{array}{l} d_{\max} \ll L_r \\ X\Omega_d \ll 4\pi \frac{f}{\Delta f} \end{array} \right. , \quad (85)$$

$$d_{\max} \ll \frac{2L_r}{\Omega_d X} \frac{f}{\Delta f} . \quad (86)$$

For usual airborne SAR systems, condition (86) is less restrictive than condition (85), so that in practice it is sufficient to check only the validity of condition (86).

References

- [1] G.Franceschetti, M.Migliaccio, D.Riccio and G.Schirinzi; "SARAS: a SAR raw signal simulator", IEEE Trans. Geosci. Remote Sens., 30, 1992.
- [2] G.Franceschetti, M.Migliaccio and D.Riccio; "SAR simulation of actual ground sites described in terms of sparse input data", IEEE Trans. Geosci. Remote Sens., 32, 1994.
- [3] G.Franceschetti, A.Iodice, M.Migliaccio and D.Riccio, "A Novel Across-Track SAR Interferometry Simulator", IEEE Trans. Geosci. Remote Sens., 36, 1998.
- [4] G. Franceschetti and R.Lanari; Synthetic Aperture Radar Processing, CRC PRESS, New York, 1999
- [5] G.Fornaro; "Trajectory Deviations in Airborne SAR: Analysis and Compensation", IEEE Trans. Aerosp. Electron. Syst., 35, 1999.
- [6] A.Moreira and Y.Huang; "Airborne SAR Processing of highly squinted data using a chirp scaling approach with integrated motion compensation", IEEE Trans. Geosci. Remote Sens., 32, 1994.
- [7] E. Alivizatos, A. Potsis, A. Reigber, A. Moreira and N. Uzunoglu; "SAR Processing with motion compensation using the extended wavenumber algorithm", Proc. EUSAR, Ulm, 2004.
- [8] D.Blacknell, A.Freeman, S.Quegan, I.A.Ward, I.P.Finley, C.J.Oliver, R.G.White and J.W.Wood; "Geometric accuracy in airborne SAR images", IEEE Trans. Aerosp. Electron. Syst., 25, 1989.
- [9] S.Buckreuss; "Motion errors in airborne synthetic aperture radar system", European Trans. Telecommunications, 2, 1991.
- [10] S.Madsen; "Motion Compensation for Ultra Wide Band SAR", Proc. IGARSS'01, Sydney, 2002.
- [11] A.Mori and F.De Vita, "A time-domain raw signal Simulator for interferometric SAR", IEEE Trans. Geosci. Remote Sens., 42, 2004.
- [12] H.J.Song, M.H.Zhu and Y.T.Bai; "Design of general purpose simulation package of SAR system", Proc. Radar 97, 697-699, 1997
- [13] L.de Salvador, P.Bemad, A.Fidalgo, G.Ilundain, J.M.Dominguez and L.Ojalvo; "IFSAR: an airborne interferometric SAR simulator", Proc. IGARSS'04, Anchorage, 2004.
- [14] E.Boerner, R.Lord, J.Mittermayer and R.Bamler; "Evaluation of TerraSAR-X Spotlight processing accuracy based on a new Spotlight raw data simulator", Proc. IGARSS'03, Toulouse 2003.

- [15] G.Fornaro, G.Franceschetti and S.Perna; “On Center Beam Approximation in SAR Motion Compensation”, in press on IEEE Geosci. Remote Sensing Lett.
- [16] J.G.Proakis and M.Salehi; Communication Systems Engineering, Prentice-Hall International Inc., Englewood Cliffs, New Jersey, 1994.

Chapter 3

Accuracy of Airborne SAR Images

As shown in Chapter 1, SAR processing of data acquired by satellite platforms is a well established technique for generation of both high resolution amplitude images and interferometric products.

On the other side, airborne SAR processing comes not straightforward from the analysis of Chapter 1 performed for the satellite case. Indeed, as shown in Chapter 2, problems arise due to the presence of atmospheric turbulences, that introduce aircraft trajectory deviations from the nominal straight flight track, as well as attitude (roll, pitch and yaw angles) and forward velocity variations. In the SAR jargon, raw data acquired in this condition are said to be affected by motion errors.

For what concerns forward velocity variations, it can be shown that, under non critical circumstances, they may be easily accounted for via standard re-sampling procedures [1], [2].

Turning to attitude variations, their impact on the focusing operation is shortly introduced at the end of this Chapter, because addressed in next Chapter.

Only trajectory deviations are examined in the following.

As shown in Chapter 2, trajectory deviations have a strong impact on the expression of the raw data; in particular, they introduce space variant effects accounted for by the simulation schemes proposed in Chapter 2.

As far as amplitude SAR image generation is concerned, such effects may strongly impair the final image quality: geometrical inaccuracies in terms of target locations are expected, as well as geometric and radiometric resolution losses [1], [2]. To account for such errors, flight parameters are measured onboard with Global Positioning Systems (GPS) and Inertial Navigation Units (INU) [2]. Then, Motion Compensation (MOCO) procedures [1]-[5] are implemented at the raw data processing stage; note that at least a rough knowledge of the scene Digital Elevation Model (DEM) is required. The compensation algorithms must preserve the efficiency of recent SAR focusing algorithms [3], [6] shown in Chapter 1, and either eliminate or reduce to an acceptable level the image focusing losses, even in the presence of residual errors due to INU, GPS and DEM inaccuracies.

For what concerns the generation of interferometric products (interferograms), the residual uncompensated trajectory deviations in single pass airborne SAR Interferometry (IFSAR) are mostly mitigated intrinsically by the system. Indeed, even in the presence of residual image defocusing,

most of the absolute residual phase errors present in the two images tend to cancel each other at the signal beating stage of the two interferometric channels. This is not the case for residual uncompensated roll angle variations that generate residual baseline tilt angle changes and thus introduce different residual errors on the trajectories followed by the antenna phase centers. Anyway, as shown in this Chapter, typical uncompensated roll angle variations associated with modern measuring systems, mainly generate phase errors in the acquired data that are not affected by subsequent processing. Proper post-focusing phase calibration steps can be applied to compensate for this effect.

Major problems arise when repeat pass airborne IFSAR is addressed: this is of key interest in differential interferometry where, in order to detect slow time scene deformations, data are not acquired simultaneously, see Chapter 1. In this case uncompensated trajectory deviations due to positioning measurement instruments or DEM inaccuracies may be significantly different in the two channels and may lead to major problems in terms of the phase accuracy of the final interferograms. These problems have been highlighted in [7], and a possible solution based only on geometric considerations and on the measurement of relative azimuth shifts associated with the differential uncompensated deviations has been proposed. A key assumption in this compensation procedure is that, but for the introduction of an azimuth shift of the SAR image, residual errors are not altered by subsequent SAR processing step, in the sense that the residual phase errors on the raw data are equal to those on the final focused image. From the phase accuracy viewpoint hereafter we refer to this particular situation as the case where only geometric phase calibration losses are introduced on the final image, thus emphasizing the absence of any additional phase artifacts resulting from the focusing operation.

In this Chapter we perform a detailed study of the interaction between uncompensated trajectory deviations and the SAR processing procedure, and we deeply analyze their effects on the focused SAR images. Such an analysis, not available in the literature, is one of the original contributions of this thesis.

We show that uncompensated trajectory deviations, occurring at raw data level, not only introduce range and azimuth target location errors and phase calibration losses in the focused images [7], but also generate additional phase artifacts. These artifacts are introduced by the SAR focusing operation and play an important role in interferometric applications. As a matter of fact, in repeat pass airborne IFSAR different uncompensated trajectory deviations occurring for the two passes introduce different phase artifacts on the two focused images, thus impairing the phase accuracy of the final interferogram. In particular, we address the case of linear and quadratic

residual errors to show that, even at small levels, they may significantly impair the phase accuracy of the processed image and therefore of the interferometric phase.

The performed analysis allows, on one side, quantifying the repeat pass interferogram phase accuracy in terms of the expected motion measurement system accuracy.

On the other side, it allows also carrying out a detailed study of the approximation commonly introduced in efficient 2D-frequency SAR processing algorithms with integrated MOCO, and referred to as Center Beam (CB) approximation in the literature. Indeed, when center beam approximation is carried out, image aberrations, similar to those caused by flight position inaccuracies, occur if data are acquired in “squinted” geometries [5], i.e., with the radar beam directed with an offset angle (squint angle) from the broadside direction [3]. Similar problems arise also when CB approximation is carried out in the absence of squint, but in the presence of steep topography [8].

In particular, we discuss in detail effects of CB approximation in terms of final image accuracy. The concept of *isomoco lines* is also introduced to explain how squint angle and track deviations introduce defocusing in the final image when use of CB approximation is made.

The Chapter is organized as follows. In Sect. 3.1 we briefly review the structure of the efficient SAR focusing algorithms with integrated MOCO. In Sect. 3.2 we investigate the mechanisms which generate residual errors on airborne processed data. In Sect. 3.3 we derive the spectral characteristics of the received data in the presence of residual errors. In Sects. 3.4 and 3.5 we analyze the effects of residual linear and quadratic errors on the final processed signal. In Sect. 3.6 we discuss the obtained results, according to the characteristics of modern available measurement positioning instruments. In Sect. 3.7, based on the results of Sects. 3.4 and 3.5, we discuss effects of Center Beam approximation in terms of final image accuracy.

3.1 Airborne SAR focusing: motion compensation procedure

Let us refer to Figs. 1 and 2, where the SAR system geometry in the presence of trajectory displacement is depicted. As usual, azimuth and (slant) range coordinates of the generic scene scattering point are $P(x,r)$ in the usual cylindrical reference system, the axis of which coincides with the nominal trajectory; $\mathcal{A}(x,r)$ is the look angle associated to the generic target

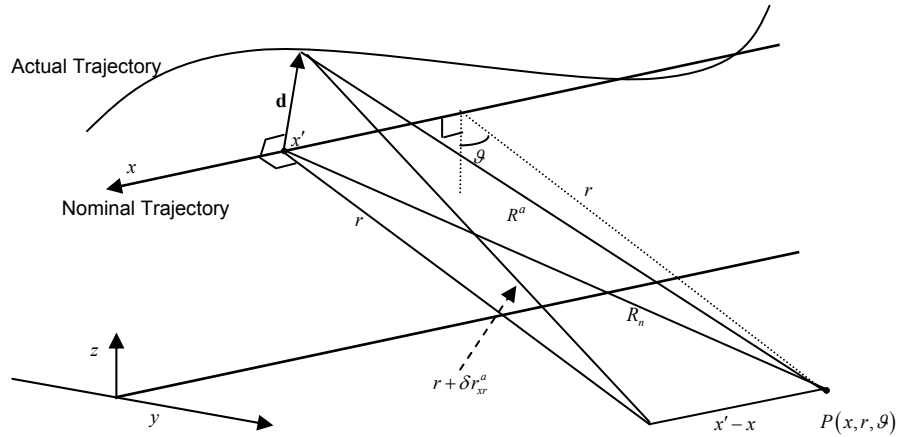


Figure 1 SAR system geometry in the presence of trajectory deviation.

$P(x, r)$. Hereafter, we make use of the same notation introduced in Chapter 2, since the acquisition geometry considered in Figs. 1 and 2 has been already analyzed there. However, in this Chapter, use of apices is introduced to distinguish actual from measured distances (“ a ” in the former case and “ m ” in the latter case). Moreover, as usual, primed variables are associated with the discrete coordinates of the signal sampling grid; on the other side, unprimed variables are associated with the (real) continuous domain.

Accordingly, $(x', 0)$ is the nominal position of the illuminating antenna; $|\vec{d}(x')|$ is the displacement vector, the amplitude and angle of which are

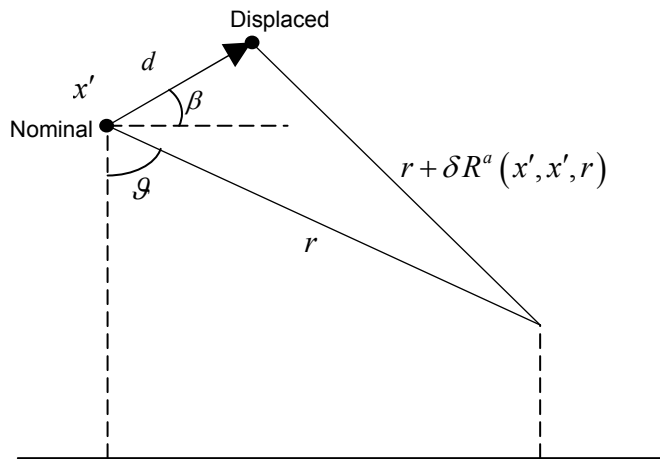


Figure 2 SAR system geometry in cross (nominal) track plane.

$d(x')$ and $\beta(x')$, respectively; the y and z components of $|\vec{\mathbf{d}}(x')|$ are the horizontal and the vertical platform displacements (the x component is supposed to be null or compensated [9]); $R^a(x',x,r)$ and $R_n(x',x,r)$ are the target-to-antenna distances in the generic azimuth position with respect to actual and nominal trajectory, respectively; $\delta R^a(x',x,r)$ is given by $R^a(\cdot) - R_n(\cdot)$ and represents the motion error *for* the target $P(x,r)$ *at* the sensor azimuth position x' ; in particular, according to the analysis of Sect 2.2, we have:

$$\delta R^a(x',x,r) = \delta r^a(x') + \psi^a(x',r) + \varphi^a(x',x,r) \quad (1)$$

As already noted, eq.(1) shows that the difference between $R^a(\cdot)$ and $R_n(\cdot)$ can be separated in three different terms: $\delta r^a(x') = \delta R^a(x',x',r_0)$, which represents the projection of the trajectory displacement onto the look direction at the scene center ($r=r_0$) and depends only on the sensor azimuth coordinate x' , thus not showing any space variant behavior; $\psi^a(x',r) = \delta R^a(x',x',r) - \delta r^a(x')$, which accounts for the variation of the projection of displacement onto the local look direction with respect to the scene center case, and depends also on the target range coordinate r , thus showing only a range-variant behavior; $\varphi^a(x',x,r)$, which includes also the azimuth-variant effects of the sensor displacement (see Sect. 2.2).

The presence of the motion error (1), as already shown in Sect. 2.1, has a strong impact on the acquired raw data: it introduces space variant effects both in range and azimuth direction. Accordingly, such effects must be accounted for during the focusing step procedure by proper Motion Compensation (MOCO) algorithms, aimed at compensating the $\delta R^a(x',x,r)$ term which corrupts the received raw data (see eqs. (4) and (7) in Sect. 2.1).

The block diagram of a general SAR focusing procedure with integrated MOCO is shown in Fig.3. The main structure of the processor, without motion compensation steps, has been shown in Sect. 1.3 and consists of a range filtering to focus the transmitted dispersed signal; a compensation of the Range Cell Migration (RCM) in both its range dependent and independent components, and the final azimuth compression, including the focus depth compensation (see Chapter 1, Fig. 5). As a matter of fact, we note that implementation of this general scheme involves a two-dimensional space variant correlation of the received echo with the point scatterer response of the SAR data acquisition system, which can be carried out via different approaches (see again Sect. 1.3) all equivalent for the subsequent discussion.

The presence of the motion error δR can be accounted for in different ways [1]-[5]; hereafter we focus on the so-called two-step MOCO

algorithms [1], [4], [5]. In this case, inclusion of MOCO appears in Fig. 3 with two additional steps.

First of all, compensation of the middle range motion error, usually referred to as *first order* MOCO, is carried out after the range compression step.

Then, a phase compensation of the range-variant motion error, usually termed *second order* MOCO, is accomplished after the RCM compensation, just before the azimuth compression.

A more detailed analysis of two-step MOCO procedure is now in order.

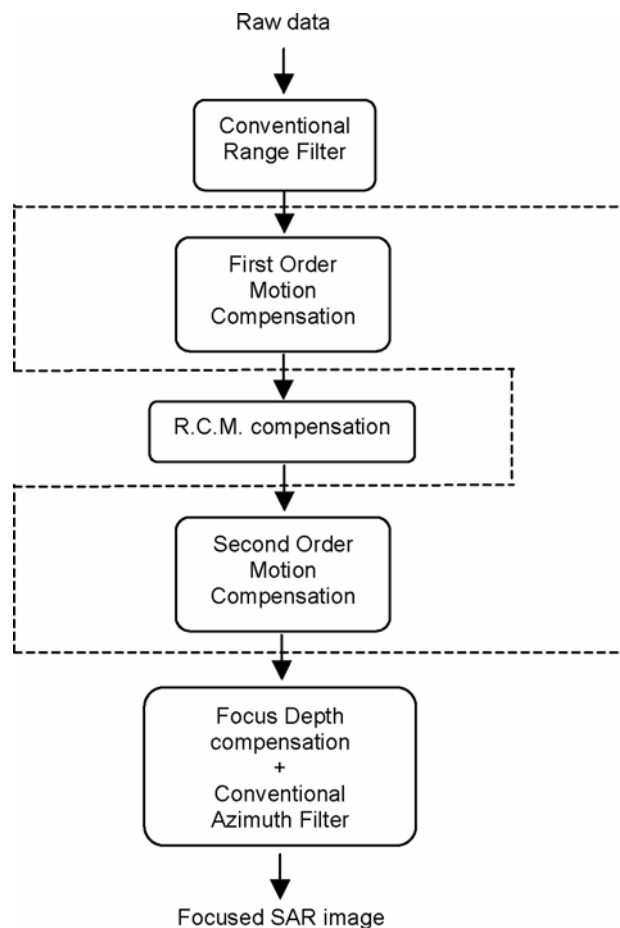


Figure 3 Block diagram of SAR processor with integrated Motion Compensation. Additive Motion Compensation terms with respect to the conventional SAR processor are highlighted with the dashed box.

First order MOCO compensates for the target-independent motion error $\delta r^a(x') = \delta R^a(x', x', r_0)$, r_0 being the midrange, both in phase, via the multiplication by the phase factor $(4\pi/\lambda)\delta R^m(x', x', r_0) = (4\pi/\lambda)\delta r^m(x')$ (λ being the carrier wavelength) and position. Let us underline that, as we are unable to use the actual $\delta R^a(\cdot)$ term (which depends on both the sensor position and the height profile of the illuminated scene, see eq.(1)) because of INU and GPS inaccuracies or DEM errors, the adopted compensation term is the measured $\delta R^m(\cdot)$.

It can be shown [1] that first order MOCO allows reliable separation of the RCM effect from the residual motion error $\delta R^a - \delta r^m$. Accordingly, after standard RCM compensation we have the following signal [1]:

$$h(x', r') \approx \iint dx dr \gamma(x, r) f_{nom}(x' - x, r' - r, r) \times \exp\left[-j \frac{4\pi}{\lambda} (\delta R^a(x', x, r) - \delta r^m(x'))\right], \quad (2)$$

where $f_{nom}(\cdot)$ is given by:

$$f_{nom}(x' - x, r' - r, r) = \text{sinc}\left[\frac{\Omega_r}{2}(r' - r)\right] w^2\left(\frac{x' - x}{X}\right) \exp\left[-j \frac{4\pi}{\lambda} R_n(x' - x, r)\right] \quad (3)$$

where, as usual, $\gamma(\cdot)$ is the ground reflectivity, $w(\cdot)$ is the antenna ground illumination pattern and Ω_r is the range bandwidth of the SAR TF. The function in (3), according to the analysis of Sect. 1.3 (see Fig.5 in Chapter 1), is compressed in range and dispersed in azimuth, its phase follows the nominal target-to-antenna distance $R_n(x' - x, r)$.

In the absence of trajectory deviations, i.e., when $\delta r^m = \delta R^a = 0$, a simple azimuth-invariant filtering carries out the final azimuth focusing, see Sect. 1.3. Conversely, in the presence of deviations, the term:

$$\exp\left[-j \frac{4\pi}{\lambda} (\delta R^a(x', x, r) - \delta r^m(x'))\right] \quad (4)$$

depending on both the sensor displacement and the generic illuminated target position, corrupts the phase in (2): the compensation of which is thus necessary before standard azimuth compression.

Note that this operation requires, in principle, a space variant processing tailored to each target; a more efficient approach, although less precise, is hence desirable [1], [4], [5]. To this end, a target independent compensation of the phase error term (4), i.e., the *second order* MOCO (see Fig.3), is carried out by multiplying (2) by the following target independent term:

$$\exp\left[j\frac{4\pi}{\lambda}(\delta R^m(x',x',r')-\delta r^m(x'))\right]=\exp\left[j\frac{4\pi}{\lambda}\psi^m(x',r')\right] \quad (5)$$

We must observe that the multiplication of (2) by (5) to compensate for (4) leads to the following phase error term:

$$\frac{4\pi}{\lambda}\delta e(x',x,r,r')=\frac{4\pi}{\lambda}[\delta R^a(x',x,r)-\delta R^m(x',x',r')] \quad (6)$$

which corrupts the signal before the final azimuth compression.

The analysis of the impact of the error (6) in terms of the final image accuracy is addressed in the following.

3.2 Residual error sources

The multiplication of (2) by (5) fully compensates for (4) when phase error of eq.(6) is negligible, that is:

$$\delta R^m(x',x',r')\approx\delta R^a(x',x,r) \quad (7)$$

As a matter of fact, we observe that eq. (7) implies three approximations, which are now addressed.

The first one:

$$\delta R^a(x',x,r)\approx\delta R^a(x',x',r) \quad (8)$$

referred to as Center-Beam (CB) approximation in the literature, assumes motion errors related to all targets within the azimuth beam to be equal to that at center beam, i.e., $\phi^a(\cdot)$ negligible in eq.(1). As a matter of fact we observe that, as shown in Chapter 2, such an approximation plays a crucial role also in the airborne raw data simulator (see conditions (24) and (30) in Chapter 2).

The second one

$$\delta R^a(x',x',r)\approx\delta R^m(x',x',r) \quad (9)$$

requires perfect knowledge of sensor position and altitude profile of the illuminated scene.

The third one:

$$\delta R^m(x',x',r)\approx\delta R^m(x',x',r') \quad (10)$$

can be considered well satisfied after RCM compensation thanks to the range shape of f_{nom} in (3), which allows reliably approximating r to r' .

Additional considerations on the approximation (9) are now in order.

Let us suppose approximation (8) and (10) perfectly satisfied; in this case, eq.(6) simplifies as follows:

$$\delta e = \delta e(x', r) = \delta R^a(x', x', r) - \delta R^m(x', x', r). \quad (11)$$

In eq.(11) we have, see Chapter 2, eqs.(14) and (74):

$$\delta R^a(x', x', r) = \delta r_r^a(x', r) \approx -d(x') \sin(\mathcal{G}(x', r) - \beta(x')); \quad (12)$$

where $\mathcal{G}(x', r)$ is the actual look angle associated to the generic target $P(x', r)$, and where the last approximation holds, as usual, when displacements are small compared with the target slant range: $\delta r_r^a(\cdot)$ reduces in this case to the displacement projection onto the target look direction. On the other hand, the measured $\delta r_r^m(\cdot)$ term is the following:

$$\begin{aligned} \delta R^m(x', x', r) = \delta r_r^m(x', r) = \\ -[d(x') + \Delta d(x')] \cdot \sin[\mathcal{G}(x', r) + \Delta \mathcal{G}(x', r) - \beta(x') - \Delta \beta(x')] \end{aligned} \quad (13)$$

where the $\Delta d(\cdot)$ and $\Delta \beta(\cdot)$ terms are related to errors in evaluation of airborne position and the $\Delta \mathcal{G}(\cdot)$ term is related to errors in evaluation of topographic height (see Fig. 4).

As it is evident from eqs.(12), (13) and Fig. 4, the contributions to the residual error $\delta e(\cdot)$ in eq.(11) are due to two different error sources: inaccuracies in the evaluation of the airborne position and of the reference DEM errors. We first expand eq.(13) for small values of $\Delta d(\cdot)$, $\Delta \beta(\cdot)$ and $\Delta \mathcal{G}(\cdot)$ and then substitute eqs. (12), (13) in eq. (11). Neglecting the exact expression of the resulting terms, which are straightforward from (13), but inessential for the following analysis, we have:

$$\delta e(x', r) = \delta e_t(x', r) + \delta e_p(x') + \delta e_{pt}(x', r) \quad (14)$$

where $\delta e_t(\cdot)$, $\delta e_p(\cdot)$ are associated exclusively to errors in the evaluation of airborne position and topographic height, respectively. The additional $\delta e_{pt}(\cdot)$ term is the mixed contribution that depends on both topographic and position errors. It can be shown that, to the first order approximation, topographic and trajectory errors are not coupled ($\delta e_{pt}(\cdot)=0$).

We note that, although generated by different mechanisms, $\delta e_t(\cdot)$, $\delta e_p(\cdot)$ and $\delta e_{pt}(\cdot)$, as well as errors induced by the center beam approximation (8)

play essentially the same role in terms of phase accuracy of the collected data and are hereafter all referred to as residual (uncompensated) errors.

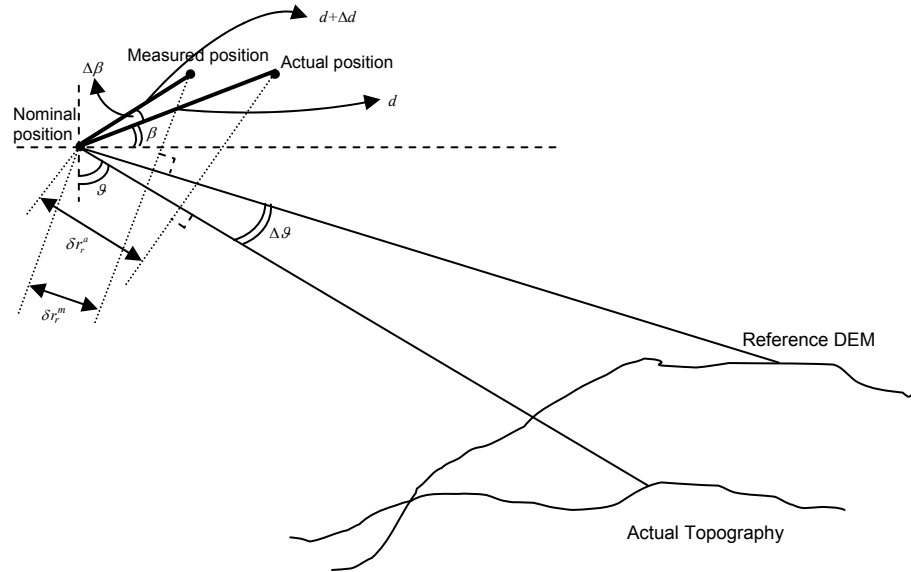


Figure 4. SAR system geometry in cross (nominal) track plane: residual errors due to incorrect airborne position and topographic height evaluation.

3.3 Spectral analysis in the presence of residual errors

Let us assume that the transmitted signal is a chirp pulse, the duration and rate of which are τ and α respectively. The expression of the received signal after the heterodyne, already shown in Sect. 2.1 is now reported for the sake of clearness:

$$h(x', r') = \iint dx dr \gamma(x, r) \text{rect} \left[\frac{r' - R^a(\cdot)}{\frac{\tau c}{2}} \right] w^2 \left(\frac{x' - x}{X} \right) \times \exp \left[-j \frac{4\pi}{\lambda} R(\cdot) - j \frac{2\alpha}{c^2} (r' - R^a(\cdot))^2 \right] \quad (15)$$

where, as usual, c is the light speed and X the azimuth footprint. For the sake of simplicity we analyze in the following the processing behavior with respect to a single point target at a fixed range, for instance at the middle-range. Note that this assumption does not imply any loss of generality, as far as use of space variant compensation steps of Fig. 3 does not introduce additional aberrations [3], [6] on the point target response, see Sect. 1.3. Accordingly, in the following we assume $\gamma(x, r) = \delta(x - x_0, r - r_0)$, and perform an analysis tailored to the point target under investigation.

Let us denote, as usual, with (ξ, η) the Fourier mates of (x', r') ; with reference to Fig. 3, first order MOCO operates after the range-filtering of the signal of eq. (15), and compensates for the term $\delta r^m(x') = \delta R^m(x', x', r_0)$ both in phase and position, so that we are left with the following signal in the (x', η) domain:

$$\begin{aligned} \hat{H}(x', \eta) = & \text{rect}\left[\frac{\eta}{\Omega_r}\right] \text{rect}\left(\frac{x' - x_0}{X}\right) \cdot \exp\left(-j\eta \frac{(x' - x_0)^2}{2r_0}\right) \times \\ & \times \exp\left(-j \frac{4\pi}{\lambda} \frac{(x' - x_0)^2}{2r_0}\right) \exp[-j\bar{\eta}(r_0 + \delta e_0(x'))]. \end{aligned} \quad (16)$$

where $\delta e_0(x') = \delta R^a(x', x_0, r_0) - \delta R^m(x', x', r_0)$ and where, as usual, see Chapter 1, $\bar{\eta} = [\eta + (4\pi/\lambda)]$, and Ω_r is the range bandwidth of the SAR TF. We have expanded the nominal target-to-antenna distance R_n at the second order, so that eq. (16) exhibits the presence of $\eta(x'-x)^2/2r_0$, i.e., the range migration term, and of $4\pi(x'-x)^2/2\lambda r_0$, which accounts for the focus depth, see Chapter 1. This expansion, introduced here for the sake of simplicity, could be easily relaxed without impairing the following analysis.

Let expand $\delta e_0(x')$ around x_0 :

$$\delta e_0(x') \approx \delta e_0(x_0) + \dot{\delta e}_0(x_0) \cdot (x' - x_0) + \frac{1}{2} \ddot{\delta e}_0(x_0) \cdot (x' - x_0)^2 \quad (17)$$

Implementation of the azimuthal FT of eq.(16) (see Appendix I) allows us to obtain the following expression of the signal spectrum:

$$\begin{aligned}
\hat{H}(\xi, \eta) = & \text{rect} \left[\frac{\eta}{\Omega_r} \right] \cdot \text{rect} \left[\frac{\xi + \dot{\delta}e_0(x_0) \cdot \bar{\eta}}{\Omega_x \cdot (r_0 \ddot{\delta}e_0(x_0) + 1)} \right] \times \\
& \times \exp \left[-j\bar{\eta} \left(r_0 + \delta e_0(x_0) - \frac{r_0 \dot{\delta}e_0^2(x_0)}{2 \cdot (r_0 \ddot{\delta}e_0(x_0) + 1)} \right) \right] \times \\
& \times \exp \left\{ j \left[\frac{r_0}{2 \cdot \bar{\eta} \cdot (r_0 \ddot{\delta}e_0(x_0) + 1)} \xi^2 + \left(\frac{r_0 \dot{\delta}e_0(x_0)}{r_0 \ddot{\delta}e_0(x_0) + 1} - x_0 \right) \xi \right] \right\}
\end{aligned} \tag{18}$$

where, as usual, Ω_x is the SAR system azimuth bandwidth, see Chapter 1.

Eq. (18) exhibits the signal spectrum in the presence of linear and quadratic residual errors before the RCM compensation, see Fig. 3.

A comment is in now order. Examination of the second factor in eq. (18) shows the presence of a spectral shift along the azimuth direction (somewhat equivalent to the presence of a Doppler Centroid) and a variation of the azimuth bandwidth generated by the first and the second derivative of $\delta e_0(\cdot)$, respectively.

The third factor exhibits the residual error $\delta e_0(\cdot)$, which appears as an additional range term, as expected by geometric considerations. In addition to this geometric term we note also the presence of another term which depends on the first and the second derivative of the residual error $\delta e_0(\cdot)$.

The last factor shows a Doppler rate variation which depends on $\ddot{\delta}e_0(\cdot)$, as well as an additional ξ -dependent phase term, related to the first and to the second derivative of the residual error $\delta e_0(\cdot)$.

We underline that the performed analysis allows showing the effects of residual errors on the received signal spectrum that couldn't be explained by simple geometric considerations. The role of these spectral effects on the final focused image is shown in the next Sections.

3.4 Effect of residual linear errors

3.4.1 Analysis

Let us suppose that the expansion for $\delta e_0(x')$, see eq.(17), can be truncated to the linear term. Then, eq. (18) simplifies as:

$$\hat{H}(\xi, \eta) = \text{rect}\left[\frac{\eta}{\Omega_r}\right] \cdot \exp[-j\eta(r_0 + \delta e_0(x_0))] \cdot \text{rect}\left[\frac{\xi + \dot{\delta}e_0(x_0) \cdot \bar{\eta}}{\Omega_x}\right] \cdot \exp\left\{j\left[\frac{r_0}{2\bar{\eta}}\xi^2 + (\delta e_0(x_0)r_0 - x_0)\xi + \frac{r_0}{2}\dot{\delta}e_0^2(x_0) \cdot \bar{\eta}\right]\right\}. \quad (19)$$

After the processing has been completed (see Appendix II), we get the image expression:

$$h(x', r') = \text{sinc}\left[\frac{\bar{\Omega}_x}{2}(x' - x_0 + \dot{\delta}e_0(x_0) \cdot r_0)\right] \cdot \text{sinc}\left[\frac{\Omega_r}{2}\left(r' - \left(r_0 + \delta e_0(x_0) - \frac{r_0}{2}\dot{\delta}e_0^2(x_0)\right)\right)\right] \times \exp\left[-j\frac{4\pi}{\lambda}\rho(x' - x_0 + \dot{\delta}e_0(x_0) \cdot r_0)\right] \cdot \exp\left[-j\frac{4\pi}{\lambda}\left(r_0 + \delta e_0(x_0) - \frac{r_0}{2}\dot{\delta}e_0^2(x_0)\right)\right] \quad (20)$$

where the bandwidth $\bar{\Omega}_x$ and the phase ramp slope coefficient ρ depend on the processed azimuth bandwidth Ω_p (see Appendix II).

Some considerations about eq. (20) are now in order.

First of all we note that, but for a resolution loss associated with the processed bandwidth and the trajectory deviations, the target is shifted in azimuth with respect to its true position by the displacement:

$$D_a = -\dot{\delta}e_0(x_0) \cdot r_0 = \tan \varepsilon \cdot r_0 \quad (21)$$

where ε is the angle between the actual and measured trajectories (see Fig. 5). This azimuth shift is well known in the literature [7] and, in agreement with the analysis in [10], it is a direct consequence of the difference between the acquisition and the processing geometry: the target is translated to its zero Doppler (ZD) position in the real trajectory which differs by an angle ε with respect to the ZD position of the processing trajectory (see Fig. 5).

Let us move now to the range analysis. Again we observe a range shift of the target with respect to its true position. To better clarify this point let us rewrite the argument of the range sinc(\cdot) function as follows:

$$\begin{aligned} r_0 - \frac{r_0}{2}\dot{\delta}e_0^2(x_0) + \delta e_0(x_0) &= r_0 - \frac{r_0}{2}\tan^2(\varepsilon) + \delta e_0(x_0) \\ &\approx r_0 - \frac{r_0}{2}\varepsilon^2 + \delta e_0(x_0) \approx r_0 \cos(\varepsilon) + \delta e_0(x_0) \end{aligned} \quad (22)$$

where the last approximation holds for little values of ε . According to Fig. 5, again the SAR processing operates a transformation between the acquisition

and the processing geometry, in agreement with [10]. In particular, due to the quoted displacement from processing (nominal) and acquisition (real) ZD position, the range is transformed as:

$$r_0 \rightarrow r_0 \left(1 - \frac{1}{2} \tan^2(\varepsilon) \right) \approx r_0 \cos(\varepsilon) \quad (23)$$

In other words SAR processing *corrects* the range coordinate from the acquisition geometry to the output geometry as well.

Further considerations about the remaining exponential term in eq. (20) are needed.

At the maximum amplitude response point, i.e., where the two sinc(\cdot) functions are equal to unity, the phase of the processed signal is $-(4\pi/\lambda)$

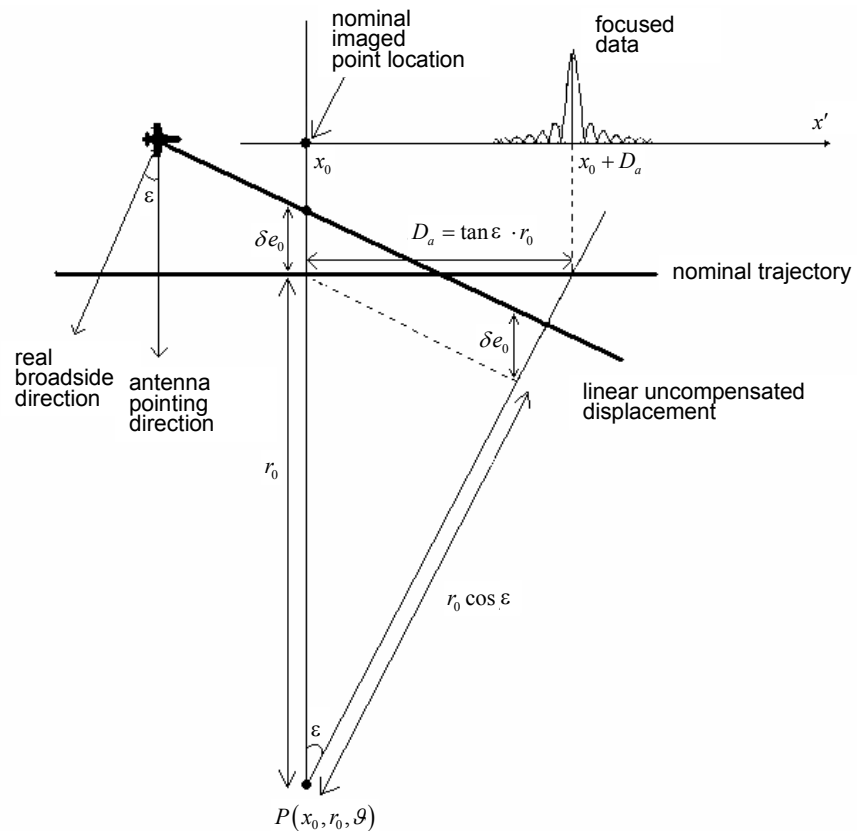


Figure 5 Slant range geometry. Processed data along the azimuth direction are overlaid to highlight the geometry change.

times the range value given by eq. (22). At variance to what is usually assumed in literature, the phase of the focused image not only shows a phase calibration loss associated with the path difference $\delta e_0(x_0)$ (geometric phase error), but it also encapsulates a $\delta \dot{e}_0(x_0)^2$ dependent term that appears as an additional phase artifact. Note that the value of this phase artifact is generated by the interaction between the SAR processing procedure and the residual motion errors, and is of paramount importance in interferometric applications, where the phase preservation is a key goal.

3.4.2 Simulation results

Geometric aberrations and phase artifacts arising from processing airborne SAR raw data in the presence of uncompensated phase errors are investigated in this Section by using simulated data: sensor parameters are

TABLE I Simulated Sensor Parameters

Nominal height	3000 m	Range resolution	1.66 m
Midrange coordinate	4984 m	Chirp bandwidth	90 MHz
Wavelength	3.14 cm	Chirp duration	5 μ s
Platform velocity	80 m/s	Azimuth resolution	43 cm
Pulse Repetition Frequency	1471 Hz	Synthetic aperture length	180 m
Sampling Frequency	100 MHz	Number of azimuth samples	16481

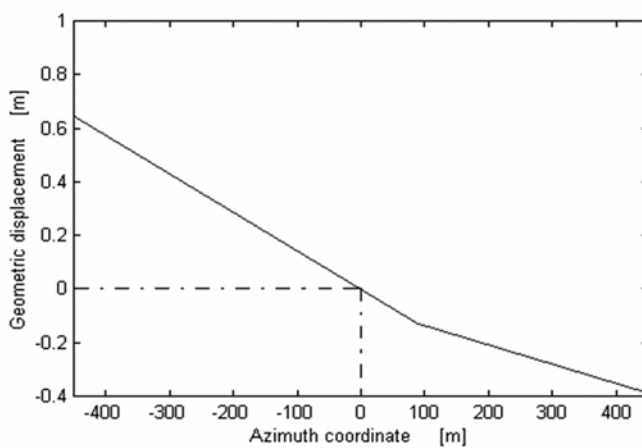


Figure 6 Linear residual error not constant over the acquisition

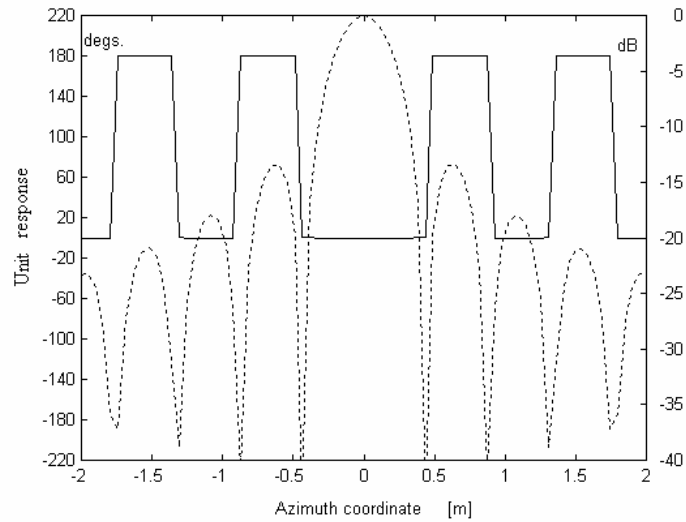


Figure 7a Phase (continuous) and amplitude (dotted) response of PT0 in the absence of residual errors (upsampled by 8). Constant phase factor corresponding to midrange has been subtracted in the phase plot.

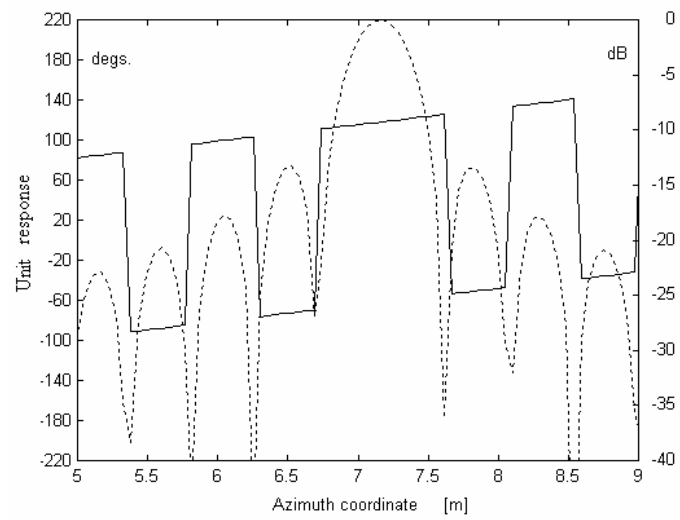


Figure 7b Phase (continuous) and amplitude (dotted) response of PT0 in the presence of the linear residual error of Fig. 6 (upsampled by 8). Constant phase factor corresponding to midrange has been subtracted in the phase plot.

collected under Table I. We underline that raw data simulations have been carried out in the space domain, whereas the processing has been performed with a frequency domain SAR focusing, independent of the simulation procedure. Figs. 6 and 7 refer to a simple scattering point (PT0) located in $x=x_0=0$ and $r=r_0=4984$ m.

Two different cases have been considered: the geometrical displacement $\delta e_0(\cdot)$ equal to zero, i.e., absence of uncompensated trajectory displacement, and $\delta e_0(\cdot)$ linearly varying with x' (Fig. 6). The corresponding azimuthal cuts of the imaged point are represented in Figs. 7a and 7b, respectively. The constant phase factor corresponding to midrange, i.e. $4\pi r_0/\lambda$, has been subtracted in all phase plots. In addition, we assumed $\delta e_0(x_0)=0$, thus rendering equal to zero the geometric phase error $4\pi\delta e_0(x_0)/\lambda$. In Fig. 7a it is recognized that no phase ramp and no phase artifacts are present. Moreover, the amplitude target response is centered in $x'=0$ at the true position. This is at variance with Fig. 7b, where both a phase deviation (artifact) along with a phase ramp is present and the amplitude target response is shifted in azimuth, in total agreement with eq. (20).

Phase artifacts and amplitude shift are both related to the first derivative of the uncompensated displacement: the higher the uncompensated trajectory slope, the higher the artifacts. Additional numerical experiments are performed with reference to two additional point targets centered in $x = x_1 = -268$ m (PT1) and $x = x_2 = 268$ m (PT2), respectively, and referring to the same uncompensated error of Fig. 6. Results of all experiments are collected in Tables II, III and IV. Table II numerically reports the expected values obtained by eqs. (20) (21) (22) for the targets PT0, PT1 and PT2. Note that the $4\pi\delta e_0/\lambda$ phase term is expressed in wrapped form. Table III reports the resulting phase and azimuth position obtained via simulation. Table IV reports the difference between theoretical and simulated results: the validity of the presented theory is evident.

Phase artifacts are azimuth dependent; to show this, we processed raw data relative to an extended uniform scene along the azimuth direction. The uncompensated trajectory deviation is again the one of Fig. 6. To highlight the phase artifact, the expected geometric phase error, i.e. $4\pi\delta e_0(x')/\lambda$, has been removed. Two plots relative to azimuth cuts of the processed and calibrated image taken on the imaged midrange are shown in fig. 8a and 8b for the amplitude and phase, respectively. The constant phase factor corresponding to midrange, i.e. $4\pi r_0/\lambda$, has been subtracted in the phase plot. We observe that the measured phase, that now coincides with the phase artifact generated by the data processing, see eq. (20), is not constant along the azimuth coordinate if the first derivative of the uncompensated displacement changes during the acquisition. The phase ramp present on the target point response in Fig. 7b is intrinsically compensated by the distributed

nature of the observed scene. To quantify the effects of the aberration arising during the SAR processing in the presence of uncompensated errors, Fig. 9 plots the phase artifact versus the total variation $\dot{\delta}e_0(x_0) \cdot X$ of the uncompensated trajectory over the synthetic antenna aperture and gives an indication of the amount of the phase artifact as function of the error between measured and real trajectories. It is recognized that even small uncompensated trajectory errors leads to non-negligible phase artifacts. For

TABLE II
Theoretical results

	x	r	δe_0	$\dot{\delta}e_0$	D_a	\hat{x}	$\frac{4\pi}{\lambda} \delta e_0$	$\frac{4\pi}{\lambda} \frac{r_0}{2} \dot{\delta}e_0^2$	Ph.
	m	m	m		m	m	degs.	degs	degs.
PT0	0	4984.187	0	0.00144	7.162	7.162	0	117.94	117.94
PT1	-268.835	4984.187	0.386	0.00144	7.162	-261.673	-146.01	117.94	-96.05
PT2	268.726	4984.187	-0.257	0.00072	3.581	272.307	-138.78	29.48	168.26

Theoretical values for the simulation: azimuth position (x), range position (r), geometric displacement (δe_0) and its first derivative ($\dot{\delta}e_0$), azimuth shift operated by data processing (D_a), azimuth imaged position (\hat{x}), geometric phase error ($4\pi\delta e_0/\lambda$), phase artifact ($2\pi r_0 \dot{\delta}e_0^2/\lambda$), phase(Ph). The constant phase factor $4\pi r_0/\lambda$ corresponding to midrange has been subtracted from the phase.

TABLE III
Simulated results

\hat{x}	Ph.
m	degs.
7.176	118.17
-261.659	-95.82
272.314	168.32

TABLE IV
Difference between theoretical and simulated results

\hat{x}	Ph.
m	degs.
0.0140	0.23
0.0140	0.23
0.007	0.06

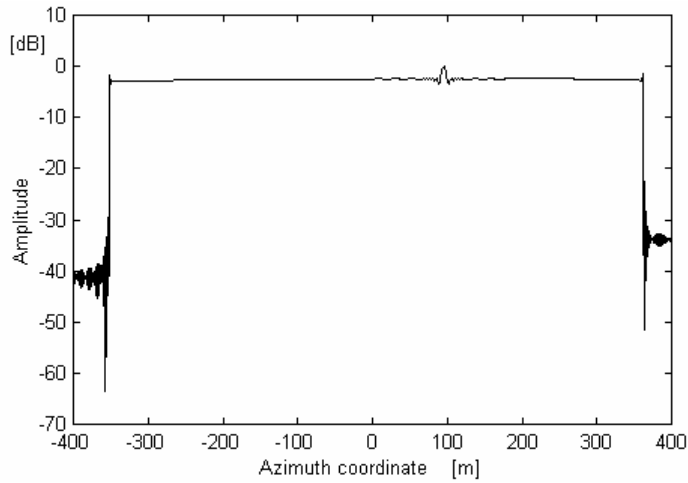


Figure 8a. Amplitude response of an extended scene in the presence of the residual error of Fig. 6.

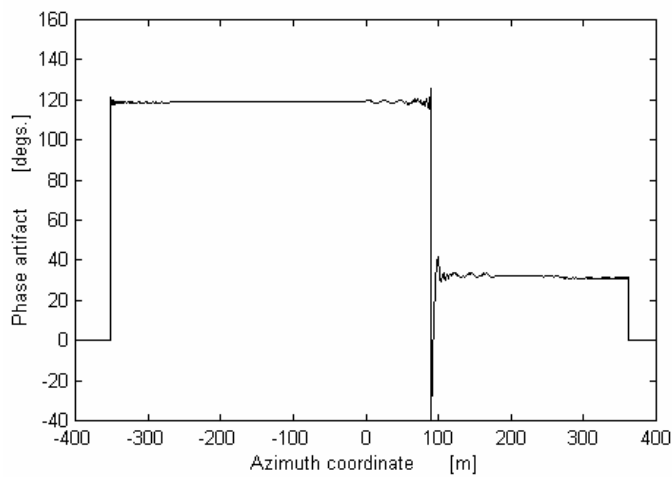


Figure 8b. Phase artifact associated with Fig. 8a., following the compensation of the geometric phase error. Constant phase factor corresponding to midrange has been subtracted as in Figs. 7.

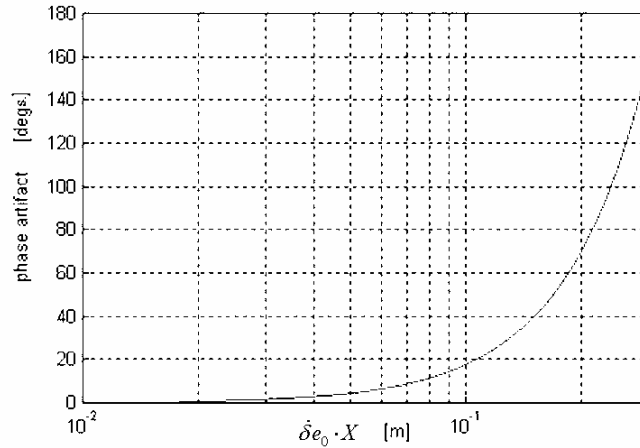


Figure 9. Residual linear errors: phase artifact vs. the uncompensated trajectory change over the synthetic antenna aperture. Sensor parameters are collected in Table I.

instance, to have an absolute phase accuracy of $\pi/8$ (about 22 degs.) on the final image, uncompensated trajectories must be limited to 10 cm over the synthetic aperture (see Fig. 9).

3.4.3 Phase accuracy and extension to the interferometric case

In the previous sub-Sections we have shown that trajectory linear residual errors generate on the final focused image phase calibration losses which could be explained by geometric considerations, and additional artifacts introduced by the SAR focusing operations. In this Section we want to highlight the effect of these aberrations on the interferometric phase.

Let us consider repeat pass airborne IFSAR. In this case data are not acquired simultaneously, in order to detect slow time scene deformations. As stated in Sect. 3.1, uncompensated trajectory deviations may be significantly different in the two channels, thus generating in the two focused images not only different phase calibration losses, but also different artifacts. This implies that the final interferogram is corrupted by differential phase errors resulting from the image pair beat. In order to understand this point, let us consider the phase of the master and slave images (at the maximum amplitude response point) in the presence of different residual error $\delta e_{01}(\cdot)$ and $\delta e_{02}(\cdot)$. According to eq. (20), these are given by:

$$\varphi_m = \frac{4\pi}{\lambda} \left[r_0 - \frac{r_0}{2} \dot{\delta}e_{01}^2(x_0) + \delta e_{01}(x_0) \right] \quad (24)$$

$$\varphi_s = \frac{4\pi}{\lambda} \left[r_0 + \delta s - \frac{r_0}{2} \dot{\delta}e_{02}^2(x_0) + \delta e_{02}(x_0) \right] \quad (25)$$

where we have assumed that the nominal trajectory is the same for the two flights and where δs is the investigated (and searched) path difference due to the displacement of the considered point target between the two passes. Accordingly, the interferometric phase, given by:

$$\varphi = \frac{4\pi}{\lambda} \left[\delta s + (\delta e_{02}(x_0) - \delta e_{01}(x_0)) - \frac{r_0}{2} (\dot{\delta}e_{02}^2(x_0) - \dot{\delta}e_{01}^2(x_0)) \right] \quad (26)$$

is corrupted by terms related to different residual errors which, obviously, do not cancel each other. Let us assume, now, that one is able to estimate the difference $[\delta e_{02}(\cdot) - \delta e_{01}(\cdot)]$: for example by measuring and integrating the azimuth-shift of the scene in the two interferometric channels [7]. Should we calibrate the output data by subtracting $4\pi[\delta e_{02}(\cdot) - \delta e_{01}(\cdot)]/\lambda$ from the interferometric phase, the output signal would still show the residual differential error associated with the different phase artifacts registered on the two channels. We underline that in [7] we are not able to measure independently the $\delta e_{02}(\cdot)$ and the $\delta e_{01}(\cdot)$ terms, but we can measure only their difference. Accordingly, the differential $2\pi r_0 [\dot{\delta}e_{02}^2(\cdot) - \dot{\delta}e_{01}^2(\cdot)]/\lambda$ artifact, which varies over the scene, cannot be estimated by the knowledge of the $[\delta e_{02}(\cdot) - \delta e_{01}(\cdot)]$ term and cannot be compensated. Note that significant variations of $\dot{\delta}e_{01}(\cdot)$ and $\dot{\delta}e_{02}(\cdot)$ may be present in real cases (see Sect. 3.6).

In conclusion, we can state that in repeat pass interferometry the final interferogram is corrupted by a differential phase error which can be compensated as in [7]. On the other hand, it is also affected by a differential phase artifact peculiar to the interaction between the SAR processing step and the different residual errors at the two channels. To date, this differential phase artifact cannot be compensated by using methods available in literature. Techniques that allow to evaluate and to eliminate this differential phase artifact are under investigation. Nevertheless, starting from the expected accuracy of a measurement positioning system mounted onboard the aircraft and of a DEM that would be used, we can estimate their differential effects on single as well as repeat pass interferometry.

In the following we quantify effects, in terms of final image accuracy, of residual errors sources introduced in Sect. 3.2. In particular, in this Section

we assume eqs.(8) and (10) always well satisfied, and focus our attention on the residual error sources of eq.(11). The errors induced by the approximation (8), i.e., by center beam approximation, are deeply investigated in Sect. 3.7.

Accordingly, the impact of error (14) on final image accuracy is now in order.

In the following we first quantify effects of DEM errors by assuming a perfect knowledge of the airborne position ($\delta e_p(\cdot)=\delta e_{pt}(\cdot)=0$ in eq. (14)) and ($\delta e_t(\cdot)$ linearly varying with x' in eq.(14). Let us address the case of a perfectly known linear trajectory deviation and of imperfect topography knowledge. We assume the worst case for the deviations direction, that is the displacement is orthogonal to the target line of sight ($\mathcal{G}=\beta$); for each acquisition we have thus (see eqs. (13) and (14)):

$$\delta e_t(x') \approx d_0 \Delta \mathcal{G} + qx' \Delta \mathcal{G}, \quad (27)$$

where $d=d_0+q \cdot x'$ is the known linear trajectory displacement and $\Delta \mathcal{G}=\Delta z/(r \cdot \sin \mathcal{G})$ is the look angle error associated to the DEM error.

Two different cases are then possible: a constant or a linear DEM error. In the first case, assuming $\Delta z = \Delta z_0$ and letting $d_0=0$, by using eq. (27) and the graph of Fig. 9, it is easy to show that DEM offsets up to 20 m introduce on the single image artifacts on a single image limited to $\pi/8$ rad (that in the worst case leads to a differential phase artifact of $\pi/8$ rad too, see eq.(26)) when the known trajectory deviations $q \cdot X$ are below 19 m. Accordingly, such errors do not introduce significant phase artifacts, whereas with 70 cm of deviation over the synthetic aperture ($q \cdot X$) we observe an azimuth shift of one fourth of the azimuth resolution cell with the same DEM offset, see eq.(21). Let us now move to the case of a constant, perfectly known, trajectory displacement $d=d_0$ ($q=0$), coupled to a linear DEM error $\Delta z=x' \cdot \tan \Omega_{tx}$, Ω_{tx} being the azimuth DEM error slope. In this case a phase error of $\pi/8$ rads is observed on the single image when $\tan \Omega_{tx}=r \cdot \sin \mathcal{G}/(10d_0X)$ (see Fig.9): for instance a value of Ω_{tx} as large as 29 degs for a trajectory displacement of 4 m.

Let us now quantify the effects of measurement positioning system inaccuracies by assuming a perfect knowledge of the topography ($\delta e_t(\cdot)=\delta e_{pt}(\cdot)=0$ in in eq. (14)) and $\delta e_p(\cdot)$ linearly varying with x' in eq.(14). In the hypothesis of Gaussian distribution of aircraft positioning instruments drifts (linear position errors), starting from eq. (26) it is easy [11] to show that the rms interferometric phase artifact σ_φ is given by:

$$\sigma_\varphi = \frac{2\pi}{\lambda} \sqrt{6} \cdot r_0 \sigma_{\delta e}^2 \quad (28)$$

where $\sigma_{\dot{\delta}_e}$ is the rms value of the positioning instrument drift.

Fig. 10 plots the rms interferometric phase artifact σ_φ versus the rms value of the positioning instrument drift $\sigma_{\dot{\delta}_e}$ for the acquisition SAR geometry of Table I. It is recognized that even small linear position errors lead to non-negligible phase artifacts. For instance, to have an absolute phase accuracy of $\pi/8$ (about 22 degs.) on the final image, the rms value of the positioning instrument drift must be limited, for the SAR acquisition geometry of Table I, to $\sigma_{\dot{\delta}_e} = 4 \cdot 10^{-4}$ (see Fig. 10).

Above considered differential phase errors are present in principle also in the interferograms obtained by single pass interferometry. Indeed, uncompensated roll angle variations may generate different residual errors on the two antennas trajectories, whereas most of the aircraft position error measurements cancel each other in the two signals beating. However, we note that modern measurement positioning systems mounted onboard the aircraft achieve an absolute roll angle accuracy ranging between 0.005 and 0.015 degs. (see Sect. 3.6), which allows us to obtain a sub-millimetric accuracy on the evaluation of the position of one antenna with respect to the other. This leads to an irrelevant phase error in the final interferogram, see Fig. 9 and eq. (26).

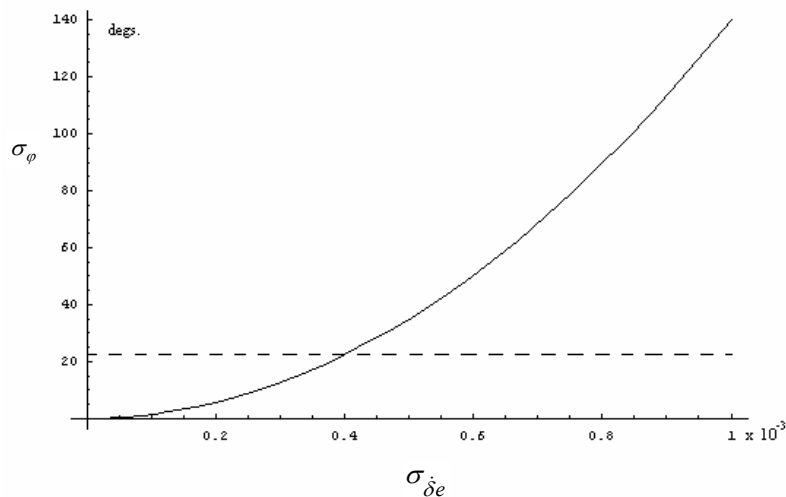


Figure 10 Interferometric residual linear errors: rms phase artifact σ_φ versus the rms value of the positioning instrument drift $\sigma_{\dot{\delta}_e}$. Sensor parameters are collected in Table I.

3.5 Effect of residual quadratic errors

Let us suppose $\delta e_0(x')$ to be purely quadratic: then eq. (18) becomes:

$$\begin{aligned} \hat{H}(\xi, \eta) = & \text{rect}\left[\frac{\eta}{\Omega_r}\right] \cdot \text{rect}\left[\frac{\xi}{\hat{\Omega}_x}\right] \cdot \exp[-j\eta \cdot (r_0 + \delta e_0(x_0))] \\ & \cdot \exp\left\{j\left[\frac{r_0}{2\bar{\eta} \cdot (1 + r_0 \cdot \ddot{\delta}e_0(x_0))} \xi^2 - x_0\xi\right]\right\}, \end{aligned} \quad (29)$$

where $\hat{\Omega}_x = \Omega_x (r_0 \cdot \ddot{\delta}e_0(x_0) + 1)$. After the processing has been completed (see Appendix IV), we get the image expression:

$$\begin{aligned} h(x', r') \approx & \exp\left[-j\frac{4\pi}{\lambda}(r_0 + \delta e_0(x_0))\right] \cdot \text{sinc}\left[\frac{\Omega_r}{2} \cdot (r' - r_0 - \delta e_0(x_0))\right] \times \\ & \times \int \text{rect}\left[\frac{\xi}{\hat{\Omega}_x}\right] \cdot \exp[j\xi^2 b(x_0)] \cdot \exp[j\xi \cdot (x' - x_0)] d\xi, \end{aligned} \quad (30)$$

where

$$b(x_0) = -\frac{1}{2} \cdot \frac{\lambda \cdot r_0}{4\pi} \cdot \frac{r_0 \cdot \ddot{\delta}e_0(x_0)}{(r_0 \cdot \ddot{\delta}e_0(x_0) + 1)} \quad (31)$$

and

$$\tilde{\Omega}_x = \min[\hat{\Omega}_x, \Omega_p], \quad (32)$$

Ω_p being the processed bandwidth.

Some considerations on eq.(30) are now in order.

In the absence of any residual quadratic error, solution of the integral of eq.(30) gives the standard SAR PSF in azimuth of Sect.1.3.

Conversely, in the presence of a residual quadratic error, i.e. $b(x_0) \neq 0$ in eq.(31), phase and geometric aberrations appear on the final image.

Let us now observe that:

$$\left| b(x_0) \cdot \left(\frac{\tilde{\Omega}_x}{2}\right)^2 \right| \approx \left| \frac{4\pi}{\lambda} \delta e_{\tilde{x}} \right| \quad (33)$$

where

$$\delta e_{\tilde{X}} = \delta e_0 \left(x_0 + \frac{\tilde{X}}{2} \right) = \frac{1}{2} \ddot{\delta} e_0 \cdot \left(\frac{\tilde{X}}{2} \right)^2 \quad (34)$$

is the quadratic residual uncompensated error at the border of the processed azimuth aperture $\tilde{X} = \lambda r \tilde{\Omega}_x / 4\pi$, and the approximation in eq. (33) holds when $r_0 \cdot \ddot{\delta} e_0(x_0) \ll 1$, see eq.(31). We must note that, since small quadratic uncompensated errors are addressed, we do not have, in general, $(4\pi/\lambda)\delta e_{\tilde{X}} \gg \pi$. Accordingly, the integral in eq.(30) represents the Fourier Transform of a chirp, the time-bandwidth product of which, see eq.(33), is not large in general; hence it cannot be solved by applying the stationary phase method and we must proceed along a different line.

Let us first suppose:

$$|\delta e_{\tilde{X}}| < \frac{\lambda}{4\pi}; \quad (35)$$

in this case, see also eq.(33), we have:

$$\left| b(x_0) \cdot \left(\frac{\tilde{\Omega}_x}{2} \right)^2 \right| < 1 \quad (36)$$

so that we can let:

$$\exp\{j\xi^2 b(x_0)\} \approx 1 + j\xi^2 b(x_0), \quad (37)$$

and from eq. (30) we obtain:

$$\begin{aligned} h(x', r') \approx & \exp\left[-j\frac{4\pi}{\lambda}(r_0 + \delta e_0(x_0))\right] \cdot \text{sinc}\left[\frac{\Omega_r}{2}(r' - r_0 - \delta e_0(x_0))\right] \times \\ & \times \left\{ \text{sinc}\left[\frac{\tilde{\Omega}_x}{2}(x' - x_0)\right] + \right. \\ & \left. + j b(x_0) \left[\left(\frac{\tilde{\Omega}_x^2}{4} - \frac{2}{(x' - x_0)^2} \right) \cdot \frac{\sin\left[\frac{\tilde{\Omega}_x}{2}(x' - x_0)\right]}{\frac{\tilde{\Omega}_x}{2}(x' - x_0)} + 2 \frac{\cos\left[\frac{\tilde{\Omega}_x}{2}(x' - x_0)\right]}{(x' - x_0)^2} \right] \right\} \end{aligned} \quad (38)$$

Some considerations about eq. (38) are now in order.

Letting $x' = x_0$ and $r' = r_0$, we obtain:

$$\begin{aligned} h(x' = x_0, r' = r_0) &\approx \exp\left[-j\frac{4\pi}{\lambda}(r_0 + \delta e_0(x_0))\right] \cdot \left[1 + j\frac{b(x_0)}{3} \cdot \frac{\tilde{\Omega}_x^2}{4}\right] \\ &\approx \exp\left[-j\frac{4\pi}{\lambda}(r_0 + \delta e_0(x_0))\right] \cdot \exp\left[j\frac{b(x_0)}{3} \cdot \frac{\tilde{\Omega}_x^2}{4}\right] \end{aligned} \quad (39)$$

Accordingly, the phase of the received signal is corrupted by the term:

$$\frac{4\pi}{\lambda}\delta e_0(x_0) - \frac{b(x_0)}{3} \cdot \frac{\tilde{\Omega}_x^2}{4} = \frac{4\pi}{\lambda}\delta e_0(x_0) - \frac{4\pi}{\lambda} \frac{\delta e_{\tilde{x}}}{3}, \quad (40)$$

where $b(x_0)$ is related to the second derivative of the uncompensated deviation term, see eq. (31), and $\tilde{\Omega}_x$ is related to the bandwidth of the processing filter, see eq. (32).

We observe that, similarly to the linear case, the phase of the focused image is corrupted not only by the regular term associated with the path difference $\delta e_0(\cdot)$ (geometric phase error), but also by the additional term $b(\cdot) \cdot \tilde{\Omega}_x^2/12 \approx (4\pi/\lambda)(\delta e_{\tilde{x}}/3)$. This again represents a phase artifact generated by the data processing and should be accounted for along with the $\delta e_0(\cdot)$ dependent term, when compensating the phase artifacts on the final image. For instance, we could process the signal at different bandwidths and check for the phase variations on the final phase image according to eq.(40).

In order to clarify this point we report in Fig. 11 the phase artifact, i.e., the term associated with $b(x_0)$ in eq. (39), for two different processing bandwidths and for the exact (continuous lines) and approximated (dashed lines) relations, versus the trajectory displacement at the border of the synthetic aperture, i.e., $\delta e_{\tilde{x}} = \ddot{\delta e}X^2/8$. Note that Fig. 11, in agreement with eq.(35), shows that the approximation in (37) holds either for small deviations or for small processed bandwidths (see continuous and dashed lines). The used SAR parameters are again those collected in Table I. This figure shows that the larger the bandwidth, the higher the phase aberration.

Effects of the above phase artifacts in differential interferometric applications can be carried out along the same lines of Sect. 3.4.3 by proper substitutions of $b(x_0) \cdot \tilde{\Omega}_x^2/12$ at the first and the second passes in place of the $\delta e_{01}(\cdot)$ and $\delta e_{02}(\cdot)$ dependent terms in eqs. (24) and (25), respectively.

Phase artifacts arising from processing airborne SAR raw data in the presence of quadratic uncompensated phase errors have been tested by using simulated data. The sensor parameters are the same collected in Table I.

Raw data relative to PT0 (see Sect. 3.4.2) have been simulated by introducing a purely quadratic uncompensated error with $\delta e_0(0) = 0$ and $\ddot{\delta e}_0(0) = 2.5 \cdot 10^{-6} \text{ m}^{-1}$, which gives an uncompensated trajectory deviation of about 1 cm at the end of the synthetic aperture (90 m equivalent to 1.1 sec of flight). The measured phase for $x' = x_0 = 0$ and $r' = r_0$ is equal to -60.22° ; the artifact calculated by using eq. (39) is equal to -53.13° ; the artifact calculated by numerically solving integral of eq. (30) is equal to -60.72° . This confirms the validity of the presented theory and provides an idea of the range validity of the approximation considered in eqs. (35) and (37).

In order to show the behavior of the target response obtained by using different processing bandwidths, we have processed raw data in the presence of the above considered error, with half-bandwidth and a quarter-bandwidth filter. The measured phase for $x' = x_0 = 0$ and $r' = r_0$ reduces now to -18.44° and to -4.80° , respectively; the artifact calculated by using eq. (39) is now -19.02° ; and -4.76° , respectively.

A last comment on the effects introduced by quadratic uncompensated errors in the final airborne SAR image is now in order.

Let us relax condition (35), and suppose:

$$\left| b(x_0) \cdot \left(\frac{\tilde{\Omega}_x}{2} \right)^2 \right| \approx \left| \frac{4\pi}{\lambda} \delta e_{\tilde{x}} \right| > 1 \quad (41)$$

In this case, we cannot use approximation (37) leading to eq.(39). By numerically solving the integral of eq.(30), we can observe that in this case, besides a phase artifact greater than $1/3$ rads (about 20 degs), a dispersion in azimuth of the final PSF appears as well.

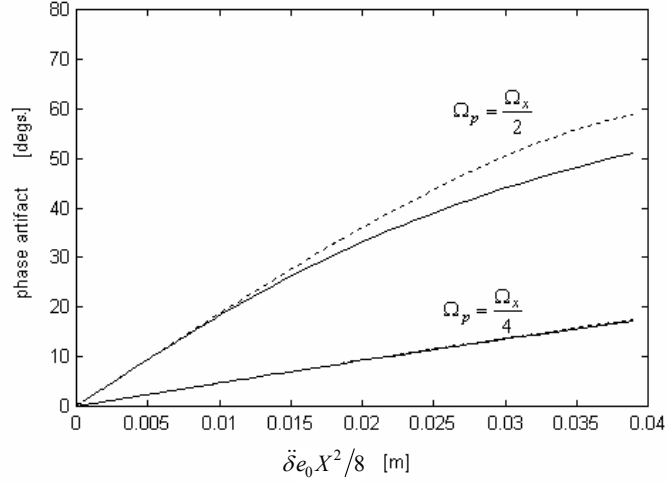


Figure 11 Residual quadratic errors: exact (dashed lines) and approximated (continuous lines) phase artifact for two different processing bandwidths vs. the trajectory displacement at the border of the synthetic aperture. Sensor parameters are collected in Table I.

3.6 Accuracy of modern aircraft motion sensing systems

In this Section we discuss the obtained results, according to the characteristics of modern available measurement positioning instruments.

Accordingly, in the following analysis, we assume eq.(8) well satisfied and also a perfect knowledge of topography ($\delta e_i(\cdot) = \delta e_{pt}(\cdot) = 0$ in eq. (14))

An appropriate first order expression for the error in the measured relative phase centre displacement along the radar line of sight is given in [12] for a general INU-based motion sensing system (MSS). Based on this expression, $\sigma_{\dot{\delta e}}$ and $\sigma_{\ddot{\delta e}}$ can be shown to be related to MSS errors as follows:

$$\sigma_{\dot{\delta e}}^2 = \frac{1}{v^2} \sigma_{\delta v}^2 + \left(\sin^2 \vartheta \right) \sigma_{\delta h}^2 \quad (42)$$

$$\sigma_{\ddot{\delta e}}^2 = \frac{1}{v^4} \sigma_{\delta b}^2 + \left(\frac{g \sin \vartheta}{v^2} \right)^2 \sigma_{\delta roll}^2 \quad (43)$$

where v is platform velocity, $g = 9.8 \text{ m/s}^2$ is the magnitude of gravity, $\sigma_{\delta b}$ is the rms value of MSS accelerometer biases, $\sigma_{\delta v}$, $\sigma_{\delta h}$, and $\sigma_{\delta roll}$ are the rms values of the initial MSS velocity, heading and roll angle respectively at the beginning of the synthetic aperture. The equations above assume that the MSS error types are uncorrelated. For modern embedded GPS/INU systems [13] [14] [15] typical values of the above quantities, after a proper post-processing operation carried out to optimally integrate INU and GPS raw data, are:

$$\begin{aligned}\sigma_{\delta v} &= 0.005 \div 0.075 \text{ m/s} \\ \sigma_{\delta h} &= 0.008 \div 0.035 \text{ deg} \\ \sigma_{\delta roll} &= 0.005 \div 0.015 \text{ deg} \\ \sigma_{\delta b} &= 10^{-3} \text{ m/s}^2\end{aligned}\tag{44}$$

Accordingly, using the sensor parameters of Table I, the values of $\sigma_{\dot{\delta e}}$ and $\sigma_{\ddot{\delta e}}$ are found to be:

$$\begin{aligned}\sigma_{\dot{\delta e}} &= 1.3 \times 10^{-4} \div 1.1 \times 10^{-3} \\ \sigma_{\ddot{\delta e}} &\leq 3.6 \times 10^{-7} \text{ m}^{-1}.\end{aligned}\tag{45}$$

Some considerations about eqs. (45) are now in order.

The rms value of modern positioning instruments drift $\sigma_{\dot{\delta e}}$ does not allow always fulfilling the requirements listed in Sect. 3.4, where the threshold of $\sigma_{\dot{\delta e}} < 4 \times 10^{-4}$ has been fixed (see Fig.10).

On the other side, the $\sigma_{\ddot{\delta e}}$ rms value of modern MSS allows us to have an uncompensated quadratic trajectory deviation less than 1.5 mm at the end of the synthetic aperture (90 m, equivalent to 1.1 sec of flight) thus achieving (see Fig. 11) negligible phase artifacts related to residual quadratic errors.

Accordingly, we can state that the effects of linear uncompensated residual errors on airborne SAR images may be critical even for modern positioning instruments; on the contrary, quadratic residual errors generate phase artifacts which can be considered negligible when modern MSS are used.

3.7 Center beam approximation in motion compensation

Based on the analysis performed in Sects. 3.4 and 3.5, in this Section we analyze effects, in terms of final image accuracy, induced by approximation (8). To this end, in the following we relax approximation (9) by assuming perfect knowledge of both sensor position and topography.

Accordingly, the corrupting phase error of eq.(6) can be rewritten as follows:

$$\frac{4\pi}{\lambda} \delta e(x', x, r) = \frac{4\pi}{\lambda} [\delta R(x', x, r) - \delta R(x', x', r)] \quad (46)$$

where the apexes “ a ” and “ m ” have been removed since, as noted above, we suppose measured and actual distances to be coincident. Moreover, hereafter we adopt a vector notation for the derivation of all the formulas.

Let us refer to Figure 12, where the usual airborne SAR system geometry is depicted. As usual, the actual position of the illuminating antenna (A) is described by its azimuth coordinate x' and by the vector $\vec{d}(x')$, lying in the plane orthogonal to nominal flight track, that accounts for platform displacements from the nominal position (N). The actual target-to-antenna distance $R(x', x, r)$ (see eq.(1) in Sect. 2.1) can be rewritten in vector form as follows:

$$R = \sqrt{R_n^2 + \vec{d} \cdot \vec{d} - 2R_n \vec{d} \cdot \hat{\mathbf{i}}} \quad (47)$$

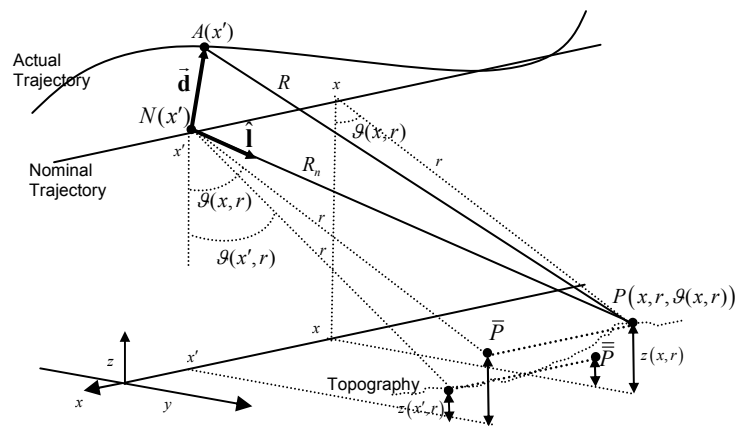


Figure 12 SAR geometry in the presence of trajectory deviations.

where $\hat{\mathbf{I}}(x-x', \mathcal{G}(x, r))$ is the unit line-of-sight vector and ‘ \cdot ’ denotes the vector inner product. Similarly:

$$\delta R(x', x, r) = R_n \left[\sqrt{1 + \frac{\bar{\mathbf{d}} \cdot \bar{\mathbf{d}}}{R_n^2} - 2 \frac{\bar{\mathbf{d}} \cdot \hat{\mathbf{I}}}{R_n}} - 1 \right] \quad (48)$$

As noted above, δR depends on both the sensor position, through $\bar{\mathbf{d}}(x')$, and on the target location, through $\hat{\mathbf{I}}(x-x', \mathcal{G}(x, r))$: it represents the motion error for the target $P(x, r)$ at the sensor azimuth position x' .

The approximation (8), which is now reported for the sake of clearness:

$$\delta R(x', x, r) \approx \delta R(x', x', r) = \delta r_r(x', r); \quad (49)$$

usually referred to as Center Beam approximation, corresponds to the assumption that, at the generic sensor position x' , the motion errors for all targets $P(x, r)$ within the beam, i.e., $\delta R(x', x, r)$, coincides with that for the center beam target $P(x', r)$, i.e., with $\delta R(x', x', r)$. This is equivalent to neglect $\varphi(x', x, r)$ in eq.(1).

Equation (49), indeed, implies approximations of the product $\bar{\mathbf{d}} \cdot \hat{\mathbf{I}}$ in (48). To explain this, we first observe that $\bar{\mathbf{d}}$ lies in the cross (nominal) track plane; accordingly $\bar{\mathbf{d}} \cdot \hat{\mathbf{I}} = \bar{\mathbf{d}} \cdot \bar{\mathbf{I}}_c$ where $\bar{\mathbf{I}}_c$ is the cross track component of $\hat{\mathbf{I}}$

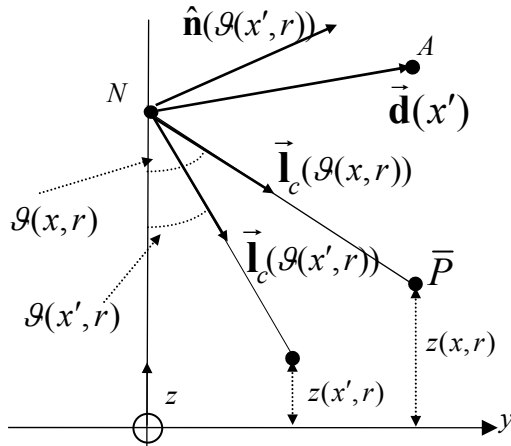


Figure 13 Topography approximation. Geometry in fig.12 is projected onto the cross (nominal) track plane. The x - x' dependence of $\bar{\mathbf{I}}_c$ has been omitted to simplify the notation.

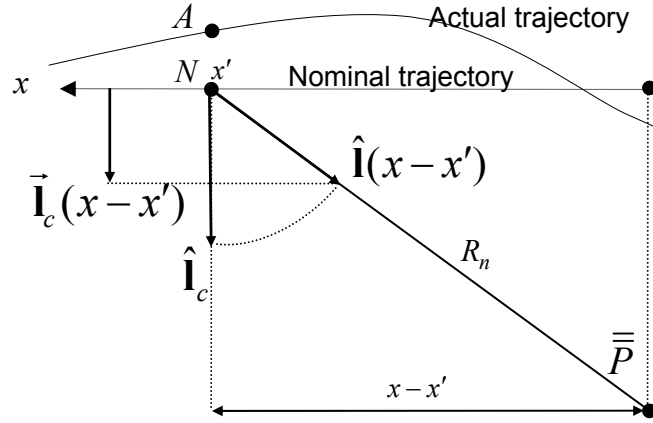


Figure 14 *Los* approximation. Geometry in fig.12 is projected onto the slant range plane at $\mathcal{G}(x',r)$. The \mathcal{G} -dependence of $\bar{\mathbf{I}}_c$ has been omitted to simplify the notation.

and thus depends on $x'-x$ and $\mathcal{G}(x,r)$. Then, we observe that (49) is the result of two steps; the first one leads to (Fig.13):

$$\bar{\mathbf{I}}_c(x-x', \mathcal{G}(x,r)) \approx \bar{\mathbf{I}}_c(x-x', \mathcal{G}(x',r)), \quad (50)$$

hereafter, called topography approximation; the second one (Fig.14) to:

$$\bar{\mathbf{I}}_c(x-x', \mathcal{G}(x',r)) \approx \bar{\mathbf{I}}_c(0, \mathcal{G}(x',r)) = \hat{\mathbf{I}}_c(\cdot, \mathcal{G}(x',r)), \quad (51)$$

referred to as *los* approximation in the following. These equations are further analyzed in the next sub-Sections.

3.7.1 Topography approximation

Approximation (50) requires the topography to be smooth enough (see figs.11-13) to let $\mathcal{G}(x,r) = \mathcal{G}(x',r)$ within the beam, or equivalently to let $\bar{\mathbf{P}} = P$ in Fig.12. As shown in Chapter 2, (see eq.(71) in Appendix III), this approximation introduces the following error in $\delta R(x',x,r)$ evaluation:

$$\delta e(x',x,r) = -\frac{\bar{\mathbf{d}}(x') \cdot \hat{\mathbf{n}}(\mathcal{G}(x',r))}{r \sin[\mathcal{G}(x',r)]} [z(x,r) - z(x',r)], \quad (52)$$

where $\hat{\mathbf{n}}(\mathcal{G}(x',r))$ is the unit vector orthogonal to $\hat{\mathbf{I}}_c(\cdot, \mathcal{G}(x',r))$ in the cross (nominal) track plane (see Fig.13), and, for each range r , $z(x',r)$ and $z(x,r)$ are the heights of the CB target $P(x',r)$ and of a generic target $P(x,r)$ inside the beam, respectively.

Let us first suppose the error (52) to be purely linear; according to the analysis of Sect. 3.4, the final point spread function (PSF) for the point target $P(x,r)$ after azimuth compression is, first of all, shifted along the azimuth direction by $D_a = \dot{\delta}e \cdot r$ ($\dot{\delta}e$ is the derivative of δe calculated for $x'=x$), see eq.(21); moreover, the phase calculated at the maximum amplitude response, is given, see eq.(24), by:

$$\varphi = \frac{4\pi}{\lambda} \left[r - \frac{r}{2} \dot{\delta}e^2 + \delta e(x,x,r) \right] = \frac{4\pi}{\lambda} r - \frac{4\pi}{\lambda} \frac{r}{2} \dot{\delta}e^2 \quad (53)$$

Accordingly, although the error in (52), induced by the topography approximation in (50), is null when $x'=x$, it generates phase and amplitude aberrations on the final focused image.

To quantify such aberrations, let us suppose such a linear error to be associated to a linear (known) topographic profile coupled with a constant (known) track deviation. In this case, from (52) we have:

$$\frac{4\pi}{\lambda} \frac{r}{2} \dot{\delta}e^2 = \frac{2\pi}{\lambda r} \left(\frac{d_{\perp}}{\sin \vartheta} \tan \alpha_t \right)^2, \quad (54)$$

where α_t is the terrain slope and $d_{\perp} = \bar{\mathbf{d}} \cdot \hat{\mathbf{n}}$ is the deviation component normal to the center-beam los. Figures 15a-b show phase errors (54) vs. terrain slope, for an X-band (blue lines) and an L-band (red lines) system, operating with a look angle $\vartheta=35^\circ$ at two different altitudes, for three different values of d_{\perp} . Note that the higher the altitude, the smaller the phase error (54); moreover, the topography approximation (50) is more critical for lower wavelengths.

Let us now assume the error (52) to be purely quadratic and let δe_x be its value at the end of the synthetic aperture. In this case, the general expression of the final SAR PSF along the azimuth is given by the integral in eq.(30), reported in the following for the sake of clearness::

$$g(x') = \int_{-1}^1 \exp \left[j \frac{4\pi}{\lambda} \delta e_x \xi^2 \right] \cdot \exp \left[j \frac{\Omega_x}{2} \xi (x' - x) \right] d\xi, \quad (55)$$

where the variable change $\xi \rightarrow \Omega_x \xi / 2$ has been considered in eq.(30) and inessential multiplicative terms have been neglected; moreover, for the sake of simplicity, in eq.(55) the assumption of full azimuth bandwidth processing, i.e., $\Omega_x = \tilde{\Omega}_x$, is done.

As shown in Sect. 3.5, if $\delta e_x \neq 0$, phase and geometric aberrations appear. In particular, when $\delta e_x < \lambda/4\pi$, mainly phase artifacts amounting to approximately $(4\pi/\lambda)(\delta e_x/3)$, are detected on the final PSF. Conversely, when $\delta e_x > \lambda/4\pi$, besides a phase artifact greater than 0.33 rads (about 20 degs), a dispersion in azimuth of the final PSF appears as well.

Quadratic terms in (52) may be due to different combinations of topography and deviations. In the following, we analyze the case of a linear known topography coupled with a known track drift: results can be extended to other combinations. From (52) we have:

$$\delta e_x = \tan(\alpha_t) \frac{\dot{d}_\perp}{r \sin \vartheta} \cdot \frac{X^2}{4} \quad (56)$$

\dot{d}_\perp being the first derivative of d_\perp and X the azimuth footprint.

Realistic values for α_t and \dot{d}_\perp in (56) normally lead to $\delta e_x > \lambda/4\pi$ and thus to a focusing dispersion of the PSF. This time, the effect depends on the footprint and can be numerically evaluated via (55) after substitution for δe_x in (56). Figure 15c shows, again for two different systems (X-band in blue lines and L-band in red lines both with two different beams) with $\vartheta=35^\circ$, combinations of topography slopes and deviation drifts that generate focusing losses of 5% (solid lines) and 50% (dotted lines) with respect to the ideal PSF 3dB main-lobe width. We can observe that the wider the azimuth footprint, the larger the focusing loss or, better, the lower (i.e., more critical) the terrain slope that generates a fixed defocusing percentage. Figure 15d shows the same systems operating at a different altitude. Note that, differently from the linear error case (Figs. 15a-b), the higher the altitude, the more critical the effects. This fact is explained by the presence of the footprint in (56) which increases with the distance r .

In summary, steep topography, although perfectly known, and trajectory deviations, although known, may lead to not negligible phase and amplitude aberrations in the focused image as a consequence of approximation in (50).

This fact has been highlighted also in [8] along with a solution based on sub-aperture processing; in our case, we have fixed the region of validity of approximation (50) by quantifying (see Figs.15) phase and geometric image aberrations in terms of topographic variations and trajectory deviations.

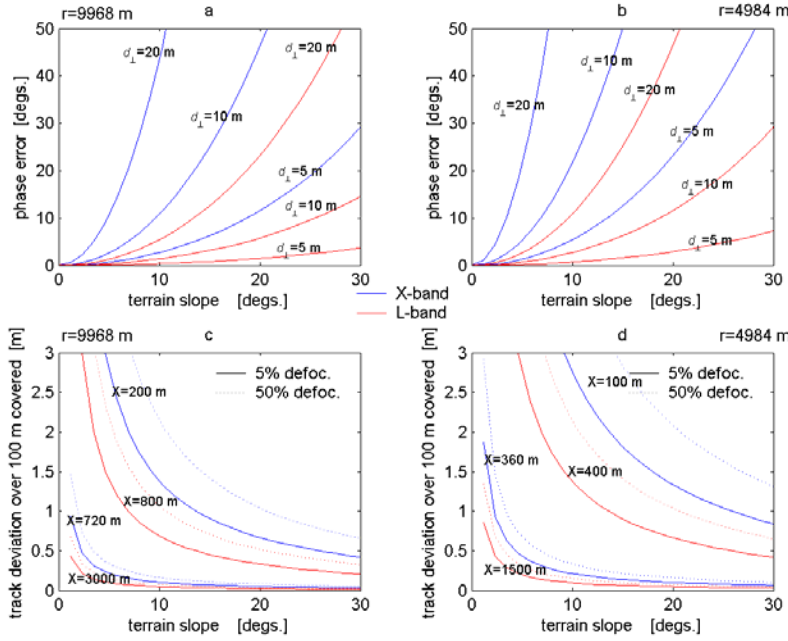


Figure 15 Effects of linear (upper plots, phase errors) and quadratic (lower plots, defocusing) errors due to the topography approximation for different terrain slopes. Systems operating at different wavelengths (blue and red) and heights (left and right) are considered. In all plots the look angle is 35° .

Extension to SAR systems different from those considered in the plots of Fig.15 can be easily carried out via (52)-(56).

3.7.2 LOS approximation

Let us assume an absence of topographic variations, fix the actual and the nominal sensor positions at the azimuth x' , and consider the CB target $P(x', r)$, i.e., the target located at the los in the broadside direction. We investigate the approximation (51) leading to (49): that is, we look for ground targets P , located at $(x, r + \Delta_{mr})$, such that:

$$\vec{d}(x') \cdot \vec{I}_c(x - x', \vartheta(x', r + \Delta_{mr})) = \vec{d}(x') \cdot \vec{I}_c(0, \vartheta(x', r)) \quad (57)$$

in other words, we seek ground targets P , located at $(x, r + \Delta_{mr})$, for which the motion error at the sensor position x' , i.e., $\delta R(x', x, r + \Delta_{mr})$, equals the motion error for the CB target $P(x', r)$, i.e., $\delta r(x', r)$. The locus of these points is a

curve, hereafter referred to as *isomoco curve* associated with $\delta r_r(x',r)$: the evaluation of which is now addressed.

Let us refer to Fig.16, where the system geometry of Fig.12 is depicted in the cross nominal track plane; $A(x')$ and $N(x')$ are the actual and the nominal sensor positions, respectively, at the azimuth coordinate x' : these points are the foci of a family of hyperbola lying in the plane orthogonal to the nominal flight track. Within this family, we pick the hyperbola passing through the CB target $P(x',r)$, and rotate it around $\vec{d}(x')$, connecting $A(x')$ and $N(x')$, thus obtaining a two-sheeted hyperboloid. By construction, this hyperboloid is the locus of the points of space for which the difference of the distances from the actual and the nominal sensor position (at the azimuth coordinate x') is equal to that of the CB target, i.e., $\delta R(x',x',r) = \delta r_r(x',r)$. The intersection between this hyperboloid and the terrain surface is the desired isomoco curve. Accordingly, as depicted in Fig.17, the x -independent $\delta r_r(x',r)$ term is exactly the motion error *at* the sensor azimuth position x' for all the targets $P(x,r+\Delta_{mr})$ of this curve passing through $P(x',r)$, that is

$$\delta R(x',x',r) = \delta r_r(x',r) = \delta R(x',x,r+\Delta_{mr}) \quad (58)$$

It can be shown (Appendix IV) that, in the absence of squint, we have:

$$\Delta_{mr} = \frac{\tan[\vartheta(x',r)] \tan[\vartheta(x',r) - \beta(x')]}{2r} [x' - x]^2 \quad (59)$$

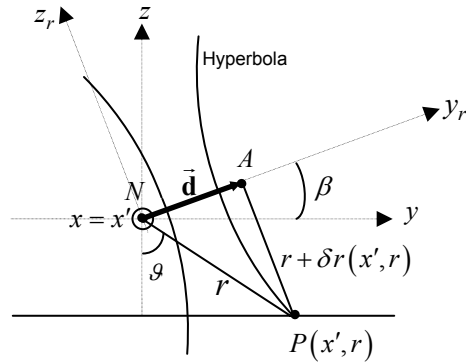


Figure 16 SAR system geometry in cross nominal track plane.

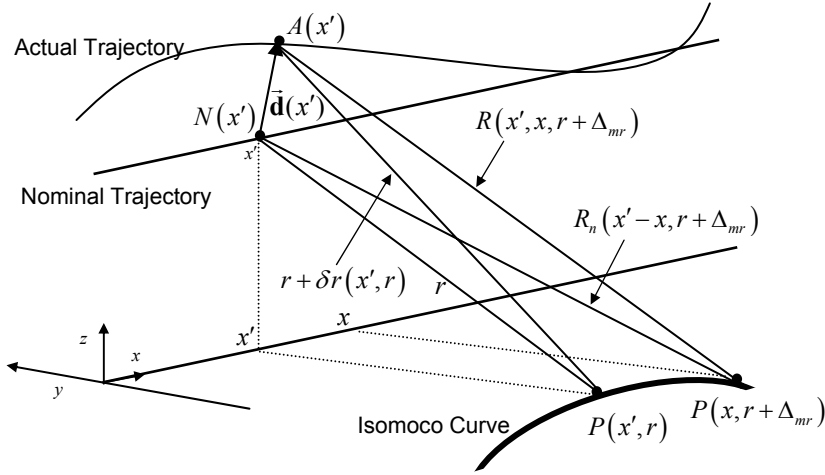


Figure 17 Isomoco curve associated with $\delta r_r(x', r)$.

$\beta(x')$ being, as usual, the angle of the platform displacement vector $\bar{\mathbf{d}}(x')$ at the azimuth position x' (see again Fig. 16). Equation (59) describes, at the fixed sensor position x' , the difference between the range coordinate of the CB target and those of all targets of the isomoco curve associated with $\delta r_r(x', r)$; accordingly it is a representation of such a curve.

Some considerations on isomoco curves are now in order.

From (59), we first observe that these curves do not depend on sensor displacement amplitude (except when $|\bar{\mathbf{d}}| = 0$ see Appendix IV). On the contrary, their concavity and curvature are strongly related to the difference $\mathcal{A}(x') - \beta(x')$ as shown in Fig.18 where isomoco curves obtained for $r=8545\text{m}$, $\vartheta=35^\circ$, $|\bar{\mathbf{d}}|=10\text{m}$ and for a flat terrain surface are depicted for different values of β .

Second, from (49) and (58) we observe that the CB approximation corresponds to assuming $\Delta_{mr}(\cdot) \approx 0$ in (58) within the azimuth footprint, or equivalently (see Appendix V), to introducing the following error $\delta R(x', x, r) - \delta R(x', x', r)$:

$$\delta e(x', x, r) \approx \frac{\bar{\mathbf{d}}(x') \cdot \hat{\mathbf{n}}(\vartheta(x', r))}{r \tan \vartheta(x', r)} \Delta_{mr} = \frac{(x' - x)^2}{2r^2} \bar{\mathbf{d}}(x') \cdot \hat{\mathbf{i}}_c(0, \vartheta(x', r)), \quad (60)$$

where the last equality holds in the absence of squint (and use of (59) is therefore possible).

In the absence of squint and for a constant deviation, i.e., for a constant

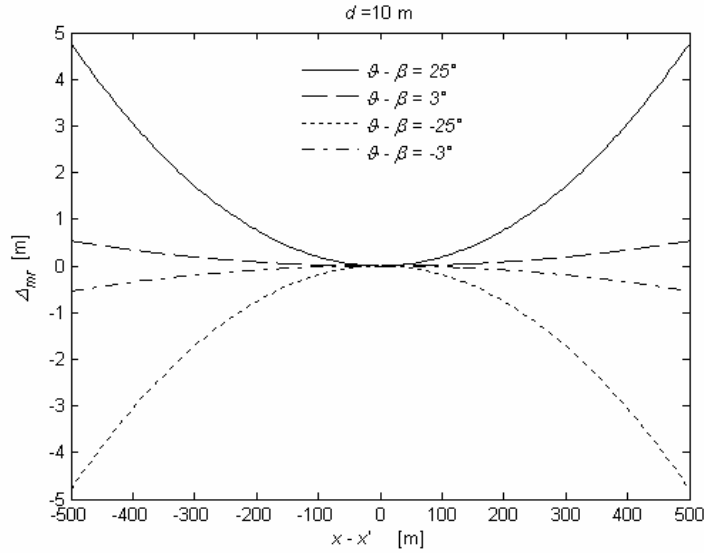


Figure 18 Isomoco curves for different displacement orientations.

$\bar{\mathbf{d}} \cdot \hat{\mathbf{l}}_c$, the error (60) becomes purely quadratic. But for very critical deviations, the magnitude of this quadratic error at the synthetic aperture border (δe_x) is generally less than $\lambda/4\pi$. As explained in Sect. 3.5, the resulting defocusing is therefore negligible, whereas phase aberrations on the final image can be detected on point scatterers. These are depicted in Figs.19a-b vs. the footprint size for different deviations, systems (X-Band in blue and L-Band in red) and heights (solid and dotted lines).

Let us now move to the case of squinted acquisitions, i.e., with the radar beam directed with an offset angle (squint angle) from the broadside direction [3], [10]. Indeed, as explained in Appendix IV, in this case, a linear component also appears in (59), thus rendering more critical the approximation (51). Moreover, such a linear component is dependent on the difference $\alpha(x') - \beta(x')$, see Fig.18 for values $x' \neq x$. In order to evaluate its impact, we also assume the presence of a track drift, again known. In this case, the coupling of los approximation and track drift leads to a quadratic component in $\delta e(x', x, r)$, the magnitude of which at the end of the synthetic aperture (δe_x) can be calculated by substituting the general expression (80) (in Appendix IV) for Δ_{mr} in (60), thus obtaining:

$$\delta e_x = \tan(\phi) \frac{\dot{d}_{\parallel}}{r} \cdot \frac{X^2}{4}, \quad (61)$$

where $d_{\parallel} = \vec{d} \cdot \hat{\mathbf{i}}_c$ is the deviation component parallel to the center-beam los; \dot{d}_{\parallel} its first derivative, and ϕ the squint angle. Realistic values for ϕ and \dot{d}_{\parallel} in (61) this time may frequently lead to $\delta e_X > \lambda/4\pi$, and thus not only to phase aberrations, but also to defocusing on the final image. This latter effect is shown in the plots of figs.19c-d obtained by numerically solving the integral in (55) after substitution for δe_X in (61). As for the topography approximation, again two different systems (with two different beams) operating with $\mathcal{G}=35^\circ$ at two different altitudes are considered to plot the combination of squint angles and deviation drifts that generate focusing losses of 5%(solid lines) and 50% (dotted lines).

To validate this result an independent experiment has been carried out by processing, with the two step MOCO algorithm in [1], raw data simulated in space domain. An X-Band system with $\mathcal{G}=35^\circ$, a footprint of 360m, a midrange distance of 4965m and a squint angle of 5 degs was considered; two different track drifts of 0.7m and 1.23m per 100m were assumed. From Fig.19c (blue dots) we expect a defocusing of 5% and 50%, respectively. In Fig. 20a plots of the azimuth cut of the PSF are depicted for the two cases,

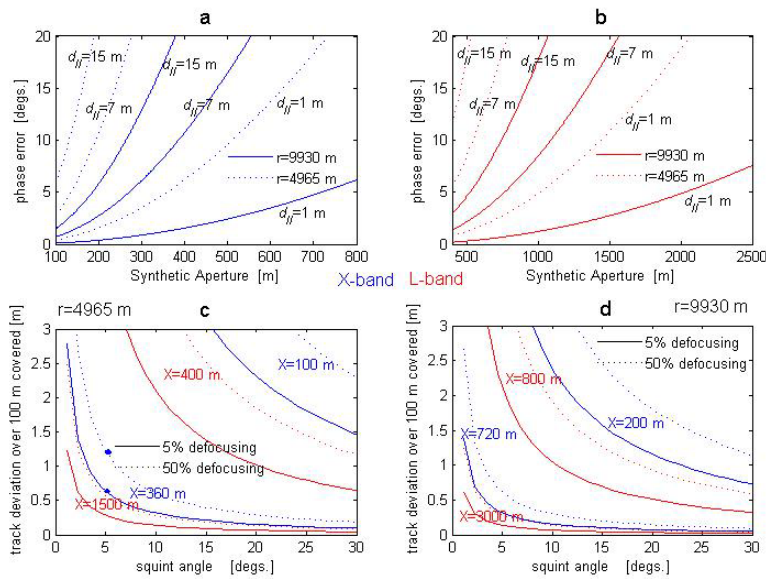


Figure 19 Effects of quadratic errors due to the los approximation on the final image. Upper plots refer to zero squint and show the phase error vs. the footprint, for different wavelengths and heights. Lower plots show the defocusing caused by track drift in the presence of squint. As for Figs. 15c-d, systems with different wavelengths (blue and red lines) and beams are considered and used at different heights (left and right). In all plots $\mathcal{G}=35^\circ$.

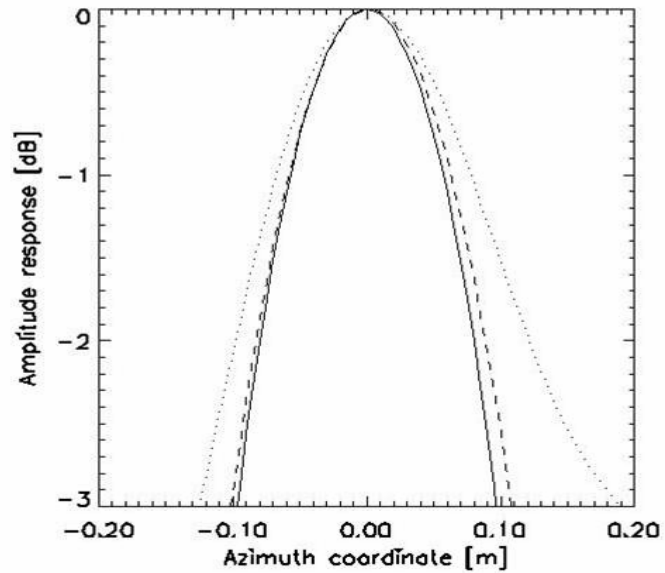


Figure 20 a

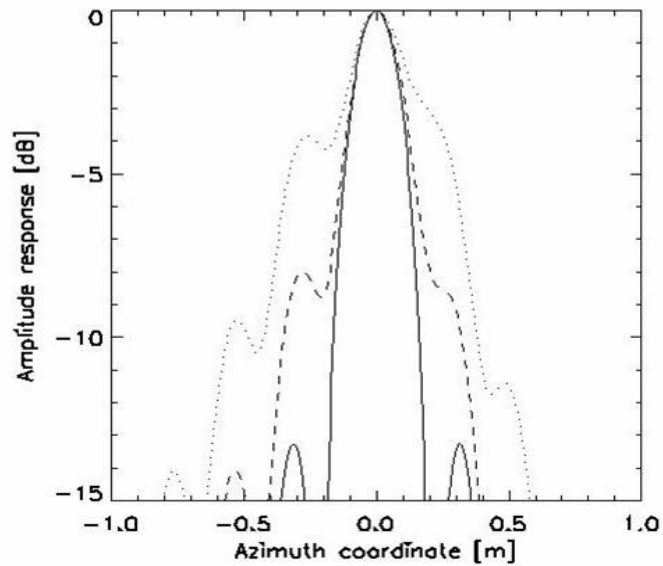


Figure 20b Azimuth cut of the post focusing Point Spread Function for 5deg of squint on two different scales (upper and lower), without (solid line), with 0.7m per 100m (dashed line) and with 1.23m per 100m (dotted line) track drift. System parameters: X-Band, 360m footprint, 4965m range, 35° look angle.

along with the ideal response: a defocusing of 5% and 58% respectively was detected; Fig. 20b shows also that side-lobe ratio becomes poor in both cases. Obviously, side-lobe ratio can be increased at the expense of resolution by reducing the processed azimuth bandwidth.

In conclusion, in the absence of squint, the los approximation in (49) corresponds to neglecting the term (59) in (58): that is, within the beam, the isomoco curves are approximated by lines (*isomoco lines*) that are orthogonal to the broadside direction (the antenna pointing direction) independently of the orientation of the trajectory displacement $\mathcal{A}(x')-\beta(x')$. RCM compensation allows the impulse response function to fit these lines before second order MOCO and, therefore, to limit the effect of CB approximation. This is not the case of squinted acquisitions where, as explained above, appearance of linear components in the isomoco curves can lead to significant defocusing in the presence of track drifts.

This problem can be tackled by referring to a plane rotated with respect to the boresight direction in Fig.16 by an angle equal to the squint angle ϕ . Isomoco lines would then become skewed and a proper processing strategy must be applied to allow the target migration matching this skew. Such a focusing strategy represents one of the original contributions of this thesis and is addressed in Chapter 4.

3.8 Summary

This Chapter presents the analysis of residual, i.e., uncompensated, motion error effects on airborne SAR images obtained by standard SAR processing with integrated MOCO. These uncompensated errors are introduced by inaccuracies of the available DEM and/or of motion sensing instruments mounted onboard the aircraft. Moreover, they can also be introduced by the so called Center Beam approximation commonly adopted by efficient MOCO algorithms.

It is shown that such uncompensated errors are critical in repeat pass interferometric applications, such as those used to detect surface displacements. In particular, it is illustrated that uncompensated motion errors generate on the final interferogram not only differential geometric phase errors, which are well known in the literature, but also differential phase artifacts. These artifacts, unlike the differential geometric phase errors, cannot be compensated by using known residual post processing compensation algorithms.

As far as positioning instrument errors is concerned, the repeat pass interferogram phase accuracy is quantified in terms of the expected motion sensing system accuracy.

Turning to center beam (CB) approximation in airborne SAR MOCO, it is shown that track deviations, topography variations and squint may lead to phase and amplitude aberrations on the final image. The analysis also stresses the need for adequate processing strategies in the presence of squint in order to avoid defocusing. This latter topic is addressed in Chapter 4.

Validity of the presented analysis is verified by some simulation examples.

APPENDIX I

Let us start from eq.(16); substituting eq.(17) in eq. (16), we obtain the following:

$$\begin{aligned} \hat{H}(x', \eta) &= \text{rect}\left[\frac{\eta}{\Omega_r}\right] \text{rect}\left[\frac{x' - x_0}{X}\right] \times \\ &\times \exp\left[-j\bar{\eta}\left(r_0 + \frac{(x' - x_0)^2}{2r_0} + \delta e_0(x_0) + \dot{\delta}e_0(x_0) \cdot (x' - x_0) + \frac{1}{2}\ddot{\delta}e_0(x_0) \cdot (x' - x_0)^2\right)\right]. \end{aligned} \quad (62)$$

Let us now implement the azimuthal FT of eq.(62). Hence:

$$\begin{aligned} \hat{H}(\xi, \eta) &= \text{rect}\left[\frac{\eta}{\Omega_r}\right] \cdot \exp[-j\bar{\eta}(r_0 + \delta e_0(x_0))] \cdot \\ &\cdot \int dx' \exp(-jx'\xi) \text{rect}\left[\frac{x' - x_0}{X}\right] \times \\ &\times \exp\left[-j\bar{\eta}\left(\frac{(x' - x_0)^2}{2r_0} + \dot{\delta}e_0(x_0) \cdot (x' - x_0) + \frac{1}{2}\ddot{\delta}e_0(x_0) \cdot (x' - x_0)^2\right)\right] \end{aligned} \quad (63)$$

Use of the stationary phase method leads to the spectrum expression of eq.(18).

APPENDIX II

Let us consider eq.(19). Note that $\eta \leq \pi/\Delta r = 4\pi/4\Delta r$, $4\Delta r \gg \lambda$, so that $\eta \ll 4\pi/\lambda$. Accordingly, we can simplify the ξ -dependent $\text{rect}(\cdot)$ function and obtain the following:

$$\begin{aligned} \hat{H}(\xi, \eta) &= \text{rect}\left[\frac{\eta}{\Omega_r}\right] \cdot \exp[-j\bar{\eta}(r_0 + \delta e_0(x_0))] \cdot \text{rect}\left[\frac{\xi + \frac{4\pi}{\lambda}\dot{\delta}e_0(x_0)}{\Omega_x}\right] \\ &\cdot \exp\left\{j\left[\frac{r_0}{2\bar{\eta}}\xi^2 + (\dot{\delta}e_0(x_0)r_0 - x_0)\xi + \frac{r_0}{2}\bar{\eta} \cdot \dot{\delta}e_0^2(x_0)\right]\right\}. \end{aligned} \quad (64)$$

Compensation of RCM and focus depth effects, and azimuth compression of eq.(64) correspond to a spectral multiplication for the $\text{rect}\left[\frac{\xi}{\Omega_p}\right]\exp\left[-j\frac{r_0\xi^2}{2\bar{\eta}}\right]$ term, Ω_p being the processed bandwidth, thus leading to the following expression of the signal spectrum:

$$\begin{aligned} \hat{H}(\xi, \eta) = & \text{rect}\left[\frac{\eta}{\Omega_r}\right] \cdot \text{rect}\left[\frac{\xi + \frac{4\pi}{\lambda}\dot{\delta}e_0(x_0)}{\Omega_x}\right] \cdot \text{rect}\left[\frac{\xi}{\Omega_p}\right] \\ & \cdot \exp[-j\bar{\eta} \cdot (r_0 + \delta e_0(x_0))] \cdot \exp\left\{j\left[\left(\dot{\delta}e_0(x_0)r_0 - x_0\right)\xi + \frac{r_0}{2}\bar{\eta} \cdot \dot{\delta}e_0^2(x_0)\right]\right\}. \end{aligned} \quad (65)$$

The multiplication of the two ξ -dependent $\text{rect}(\cdot)$ functions in eq. (65) leads to:

$$\begin{aligned} \hat{H}(\xi, \eta) = & \text{rect}\left[\frac{\eta}{\Omega_r}\right] \cdot \text{rect}\left[\frac{\xi + \frac{4\pi}{\lambda}\rho}{\bar{\Omega}_x}\right] \cdot \exp[-j\bar{\eta} \cdot (r_0 + \delta e_0(x_0))] \\ & \cdot \exp\left\{j\left[\frac{r_0}{2}\bar{\eta} \cdot \dot{\delta}e_0^2(x_0) + \left(\dot{\delta}e_0(x_0)r_0 - x_0\right)\xi\right]\right\}. \end{aligned} \quad (66)$$

where the bandwidth $\bar{\Omega}_x$ and the phase ramp slope coefficient ρ depend on the processed bandwidth Ω_p :

$$\begin{cases} \bar{\Omega}_x = \min\left[\left(\Omega_x + \Omega_p - 8\pi|\dot{\delta}e_0|/\lambda\right)/2, \Omega_p\right] & \text{if } \Omega_p \leq \Omega_x + 8\pi|\dot{\delta}e_0|/\lambda \\ \bar{\Omega}_x = \Omega_x & \text{if } \Omega_p \geq \Omega_x + 8\pi|\dot{\delta}e_0|/\lambda \end{cases} \quad (67)$$

and $\rho(\Omega_p)$ is given by the graph of Fig. 21.

Two-dimensional IFT of eq. (66) leads to the image expression of eq. (20).

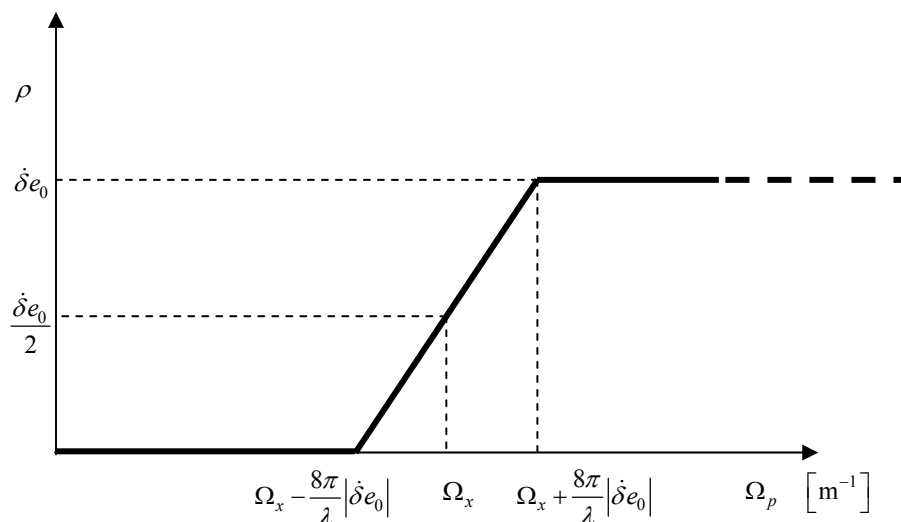


Figure 21 Phase ramp slope coefficient ρ vs. the processed bandwidth Ω_p

APPENDIX III

Let us consider eq.(29): compensation of RCM and focus depth effects, and azimuth compression (see Appendix II) leads to the following expression of the signal spectrum:

$$\begin{aligned} \hat{H}(\xi, \eta) = & \text{rect}\left[\frac{\eta}{\Omega_r}\right] \cdot \text{rect}\left[\frac{\xi}{\tilde{\Omega}_x}\right] \cdot \exp[-j\eta \cdot (r_0 + \delta e_0(x_0))] \\ & \cdot \exp\left\{j\left[\frac{r_0}{2 \cdot \left(\eta + \frac{4\pi}{\lambda}\right)} \left(\frac{-r_0 \cdot \ddot{\delta e}_0(x_0)}{1 + r_0 \cdot \ddot{\delta e}_0(x_0)}\right) \xi^2 - x_0 \xi\right]\right\} \end{aligned} \quad (68)$$

where $\tilde{\Omega}_x = \min[\hat{\Omega}_x, \Omega_p]$, Ω_p being the processed bandwidth. Note that $\eta \leq \pi/\Delta r = 4\pi/4\Delta r$, $4\Delta r \gg \lambda$, so that $\eta \ll 4\pi/\lambda$. Accordingly, a simple series expansion in the phase of the last exponential leads to:

$$\begin{aligned} \hat{H}(\xi, \eta) \approx & \text{rect}\left[\frac{\eta}{\Omega_r}\right] \cdot \text{rect}\left[\frac{\xi}{\tilde{\Omega}_x}\right] \cdot \exp[-j\eta \cdot (r_0 + \delta e_0(x_0))] \cdot \\ & \cdot \exp\left\{j\left[\frac{1}{2} \cdot \frac{\lambda \cdot r_0}{4\pi} \left(\frac{-r_0 \cdot \ddot{\delta} e_0(x_0)}{1 + r_0 \cdot \ddot{\delta} e_0(x_0)}\right) \left(1 - \frac{\lambda \eta}{4\pi}\right) \xi^2 - x_0 \xi\right]\right\} \end{aligned} \quad (69)$$

Expression of the IFT of eq.(69) along the range direction is the following:

$$\begin{aligned} \tilde{H}(\xi, r') \approx & \text{sinc}\left[\frac{\Omega_r}{2} \cdot \left(r' - r_0 - \delta e_0(x_0) - \xi^2 \cdot \frac{\lambda \cdot b(x_0)}{4\pi}\right)\right] \text{rect}\left[\frac{\xi}{\tilde{\Omega}_x}\right] \\ & \exp\left[-j\frac{4\pi}{\lambda}(r_0 + \delta e_0(x_0))\right] \cdot \exp\left\{-j\left[x_0 \xi - b(x_0) \xi^2\right]\right\} \end{aligned} \quad (70)$$

where $b(x_0)$ is given by eq.(31). Accordingly, the IFT of $\tilde{H}(\xi, r')$ along the azimuth direction is:

$$\begin{aligned} h(x', r') \approx & \exp\left[-j\frac{4\pi}{\lambda}(r_0 + \delta e_0(x_0))\right] \cdot \int \text{rect}\left[\frac{\xi}{\tilde{\Omega}_x}\right] \cdot \exp\left[j\xi^2 b(x_0)\right] \times \\ & \times \exp\left[j\xi \cdot (x' - x_0)\right] \cdot \text{sinc}\left[\frac{\Omega_r}{2} \cdot \left(r' - r_0 - \delta e_0(x_0) - \xi^2 \cdot \frac{\lambda \cdot b(x_0)}{4\pi}\right)\right] d\xi \end{aligned} \quad (71)$$

Let us suppose

$$\left|b(x_0) \cdot \frac{\tilde{\Omega}_x^2}{4}\right| < 1; \quad (72)$$

accordingly, we have $\left|\frac{\lambda}{4\pi} b(x_0) \xi^2\right| \leq \left|\frac{\lambda}{4\pi} b(x_0) \cdot \frac{\tilde{\Omega}_x^2}{4}\right| \ll \Delta r$, and eq. (71), rearranged, leads to the expression of eq.(30).

APPENDIX IV

We fix the range coordinate $r = \bar{r}$ and derive the analytical expression of the isomoco curve $\Delta_m(\cdot)$ associated with $\delta r(x', \bar{r})$. We consider the two-sheeted hyperboloid passing through $P(x', \bar{r}, \vartheta)$, the foci of which are $A(x')$ and $N(x')$ (see Fig.16 letting $r = \bar{r}$).

For the sake of cleanness, we first write its equation in a Cartesian reference system (x, y_r, z_r) with origin in $N(x')$, the x and y_r axes of which coincide with the nominal track and with the displacement vector direction, respectively; and the z_r -axis of which is implicitly defined by x and y_r (see Fig. 16). Then we move to a Cartesian reference system (x, y, z) rotated by an angle β (β being the angle of the sensor displacement vector $\vec{d}(x')$, see Fig.16) with respect to the reference system (x, y_r, z_r) introduced above. Finally, we extend the obtained results to the usual cylindrical reference system of Sect 3.1

The Cartesian equation of the above introduced two-sheeted hyperboloid in the reference system (x, y_r, z_r) is the following:

$$\frac{(y_r - d/2)^2}{a^2} - \frac{(z_r)^2}{b^2} - \frac{(x - x')^2}{b^2} = 1 \quad (73)$$

where:

- $2a = \delta r_r(x', \bar{r})$; $b^2 = a^2 - (d/2)^2$;
- $d = d(x')$ is the amplitude of the displacement vector $\vec{d}(x')$.

Let us now move to the Cartesian reference system (x, y, z) by using the following well-known rotation rules:

$$\begin{cases} y_r = z \sin \beta + y \cos \beta \\ z_r = z \cos \beta - y \sin \beta \end{cases} \quad (74)$$

thus obtaining the following hyperboloid equation:

$$\frac{(z \sin \beta + y \cos \beta - d/2)^2}{a^2} - \frac{(z \cos \beta - y \sin \beta)^2}{b^2} - \frac{(x - x')^2}{b^2} = 1 \quad (75)$$

Of course, if $d=0$, i.e. $A(x') \equiv N(x')$, we have $\delta r = a = 0$, and all points of the space belong to this particular hyperboloid the foci of which are coincident. Accordingly, we do not consider this singular case and, hereafter, we suppose $d \neq 0$.

The Cartesian coordinates of the above considered point target P can be easily obtained via the following transformation rules:

$$\bar{x} = x'; \quad \bar{y} = \bar{r} \sin \mathcal{G}; \quad \bar{z} = -\bar{r} \cos \mathcal{G}. \quad (76)$$

We assume in the following a flat terrain and consider the intersection of the hyperboloid (75) with the plane $z = \bar{z}$ thus obtaining, after proper manipulations:

$$\frac{\bar{z}^2 + y^2}{b^2} + \frac{(x - x')^2}{b^2} = \left[\frac{d \cdot (\bar{z} \sin \beta - y \cos \beta)}{2ab} + \frac{b}{a} \right]^2 \quad (77)$$

Equation (77) describes the isomoco curve lying in the plane $z = \bar{z}$ and passing, by construction, through $P(x', \bar{y}, \bar{z})$, i.e, the *isomoco curve* associated with $\delta r_r(x', \bar{r})$.

Let us now move to the common cylindrical reference system introduced in Sect.2; the range coordinate of a generic point $\hat{P}(x, y, \bar{z})$ of (77) is given by:

$$r = (\bar{r} + \Delta_{m\bar{r}}) = \sqrt{\bar{z}^2 + y^2} . \quad (78)$$

Substitution of (78) in (77) leads to:

$$c_1 \Delta_{m\bar{r}}^2 + c_2 \Delta_{m\bar{r}} + (x' - x)^2 = 0 , \quad (79)$$

where use of a second order expansion for y , via inversion of (78), has been made, and where:

$$c_1 = 1 - \left(\frac{d \cos \beta}{2a \sin \vartheta} \right)^2 - \frac{d \cos \beta}{2a \sin \vartheta} \cot^2 \vartheta ; \quad c_2 = 2\bar{r} \left(\frac{d \cos \beta}{2a \sin \vartheta} + 1 \right) .$$

Solutions of equation (79) for $\Delta_{m\bar{r}}(\cdot)$ can be easily obtained and only one is of physical interest. We can consider an expansion of $\Delta_{m\bar{r}}(\cdot)$ around $x - x' = r \tan \phi$, ϕ being the squint angle:

$$\begin{aligned} \Delta_{m\bar{r}} \approx \Delta_{m\bar{r}} \Big|_{x' = x - r \tan \phi} + \frac{\partial \Delta_{m\bar{r}}}{\partial x'} \Big|_{x' = x - r \tan \phi} (x - x' - r \tan \phi) + \\ + \frac{1}{2} \frac{\partial^2 \Delta_{m\bar{r}}}{\partial x'^2} \Big|_{x' = x - r \tan \phi} (x - x' - r \tan \phi)^2 , \end{aligned} \quad (80)$$

leading to (59) when absence of squint, i.e., when $\phi=0$, is assumed.

APPENDIX V

Let us expand $\delta R(x', x', r)$ along the range coordinate r :

$$\delta R(x', x', r) \approx \delta R(x', x', \bar{r}) + \left. \frac{\partial \delta R(x', x', r)}{\partial r} \right|_{r=\bar{r}} (r - \bar{r}) \quad (81)$$

It is easy to show [3] that $\partial \delta R(x', x', r) / \partial r = -\vec{\mathbf{d}} \cdot \hat{\mathbf{n}} / (r \tan \bar{\mathcal{G}})$; so that substitution of (81) in (58), and use of (59) lead to (60).

It is interesting to compare eq. (60) to the expression of $\varphi(x', x, r)$ derived in Chapter 2 (see eq.(67), Appendix III, Chapter 2) and reported in the following for the sake of clearness:

$$\varphi(x', x, r) \approx \delta r_{xr}(x', x, r) - \delta r_r(x', r) - \frac{(x' - x)^2}{2r^2} \delta r_{xr}(x', x, r) \quad (82)$$

Equations (81) and (82) both represent the difference $R(x', x, r) - R(x', x', r)$. Equation (81) is obtained in the hypothesis of flat terrain; this is not the case for the expression eq.(82).

In the hypothesis of flat terrain, $\delta r_r(x', r)$ becomes equal to $\delta r_{xr}(x', x, r)$ (see Chapter 2) and eqs. (81) and (82) become coincident.

When the flat terrain hypothesis is relaxed, the difference between eq.(82) and eq.(81) is given by the term: $\delta r_{xr}(x', x, r) - \delta r_r(x', r)$ which coincides with eq.(52) (see eq.(71), Appendix III, Chapter 2), separately analyzed in Sect. 3.7.1, where only topography approximation is addressed.

References

- [1] G.Fornaro; “Trajectory Deviations in Airborne SAR: Analysis and Compensation”, IEEE Trans. Aerosp. Electron. Syst., 35, July 1999.
- [2] S.Buckreuss; “Motion errors in airborne synthetic aperture radar system”, European Trans. Telecommunications, 2, 1991.
- [3] G.Franceschetti and R.Lanari; Synthetic Aperture Radar Processing, CRC PRESS, New York, 1999.
- [4] A.Moreira and Y.Huang; “Airborne SAR Processing of highly squinted data using a chirp scaling approach with integrated motion compensation”, IEEE Trans. on Geosci. Remote Sens., 32, 1994.
- [5] E.Aliviazatos, A.Potsis, A.Reigber, A. Moreira and N. Uzunoglu; “SAR Processing with motion compensation using the extended wavenumber algorithm”, Proc. EUSAR, Ulm, 2004.
- [6] R.Bamler; “A Comparison of Range-Doppler and Wavenumber Domain SAR Focusing Algorithms”, IEEE Trans. on Geosci. Remote Sens., 30, 1992.
- [7] A.Reigber and K.P.Papathanassiou; “Correction of residual motion errors in airborne repeat-pass interferometry”, Proc. IGARSS, Sydney, 2001.
- [8] K.A.C.de Macedo and R.Scheiber, ”Precise Topography–and Aperture Dependent Motion Compensation for Airborne SAR”, IEEE Geosci. and Remote Sens. Lett., 2, 2005.
- [9] D.Blacknell, A.Freeman, S.Quegan, I.A.Ward, I.P.Finley, C.J.Oliver, R.G.White and J.W.Wood; “Geometric accuracy in airborne SAR images”, IEEE Trans. Aerosp. Electron. Syst., vol. 25, pp.241-258, Mar. 1989.
- [10] G.Fornaro, E.Sansosti, R.Lanari and M.Tesauro; “Role of Processing Geometry in SAR Raw Data Processing”, IEEE Trans. Aerosp. Electron. Syst., 38, 2002.
- [11] A.Papoulis; Probability, Random Variables, and Stochastic Processes, McGraw-Hill Inc., third edition, Singapore, 1991.
- [12] D.J.Di Filippo, G.E.Haslam and W.S.Windall; “Evaluation of a Kalman Filter for SAR Motion Compensation”, Proc. IEEE PLANS 88, Orlando, Florida, September 1988.
- [13] Honeywell technical product description:
<http://content.honeywell.com/dses/products/navigators/gn-h764g.htm>
- [14] Northrop Grumman technical product description:
<http://www.nsd.es.northropgrumman.com/Automated/sitemap/index.html>

- [15] Applanix technical product description;
http://www.applanix.com/html/products/prod_airborn_index.html

Chapter 4

Airborne SAR Focusing in the Presence of Squint

Due to platform attitude instabilities, airborne SAR raw data are generally acquired in “squinted” geometries, i.e., with an offset angle (squint angle) of the radar beam from broadside direction, which may produce artifacts in the focused images if not properly accounted for during the SAR processing [1]-[4]. Additionally, due to the presence of atmospheric turbulences, airborne SAR raw data are also affected by deviations of the platform from an ideal straight flight track. Such deviations may significantly impair the final image quality. As shown in chapter 3, in order to eliminate/mitigate these errors to an acceptable level, Motion Compensation (MOCO) must be included at the raw data processing stage [5]-[7].

Recently, processing problems have been highlighted when trajectory deviations occur in squinted geometry [7]. These problems have been investigated in Sect. 3.7, where it is shown that track deviations and squint may lead to phase and amplitude aberrations on the final image, due to the effects induced by center beam approximation in motion compensation. The analysis shown in Sect. 3.7 also stresses the need for adequate processing strategies in the presence of squint in order to avoid defocusing.

In this chapter we investigate the impact of the focusing operation carried out on squinted raw data with motion errors.

We first (Sect. 4.1) shortly review the basic rationale of standard SAR focusing in the presence of squint, but in the absence of track deviations. In particular, we show (Sect. 4.2) that standard efficient SAR focusing strategy [4], carried out in the usual cylindrical geometry, can be easily extended to a more convenient, for the squinted case, conical geometry [1].

Then, we show that, differently from the no-deviation case, raw extension of efficient standard two step MOCO approach [5]-[7] to conical geometry, although possible, does not allow avoiding defocusing in the final image.

Accordingly, a strategy different from that of [5]-[7] must be adopted to overcome problems shown in Sect. 3.7 and registered in [7] in the presence of both track deviations and squint.

In this Chapter we highlight, for the first time, the key role played by *range walk correction* in SAR focusing of squinted airborne data.

Based on such an analysis, a new motion compensation approach able to properly manage trajectory deviation at non-zero squint is proposed.

The key point of this approach consists in the separation of Range Cell Migration compensation in two different steps: Range Curvature correction, to be carried out, as usual, *before* the second order MOCO; and Range Walk correction, to be implemented, differently from the standard MOCO approach [5]-[7], *after* the second order MOCO

Simulation results, aimed at validating the effectiveness of the proposed approach are also presented.

4.1 SAR squinted data focusing in the absence of track deviations

Let us refer to Fig. 1, where the SAR system geometry is depicted; the usual cylindrical reference system, the axis of which coincides with the sensor flight path is considered; data are supposed to be acquired with an offset point angle ϕ_d (squint angle) from the broadside direction; absence of trajectory deviation is here assumed.

Evaluation of the SAR TF in the presence of squint is now in order.

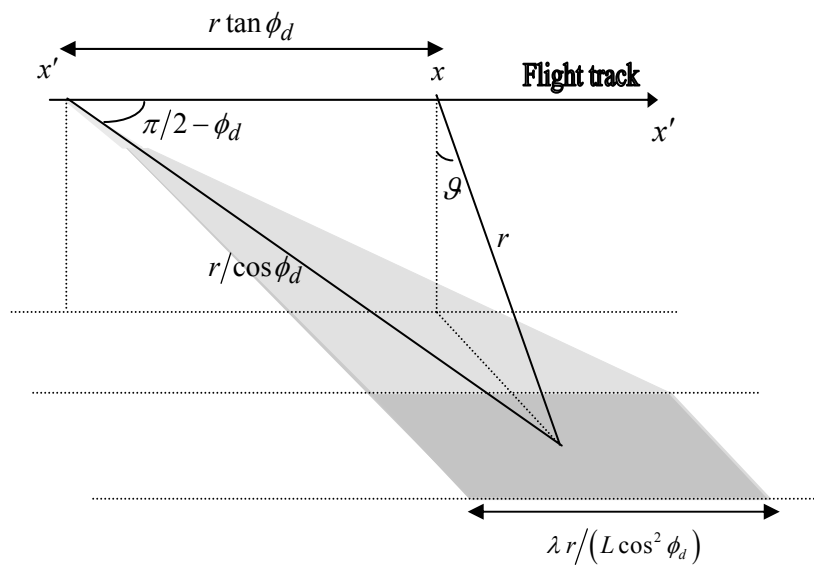


Figure 1 SAR system geometry in the presence of squint.

4.1 SAR squinted data focusing in the absence of track deviations 151

As usual, we assume to transmit a chirped pulse, the carrier frequency, chirp-rate and duration of which are f , α and τ , respectively; in this case the new expression:

$$g(x' - x, r' - r, r) = \text{rect} \left[\frac{r' - r - \Delta R}{c\tau/2} \right] w^2 \left[\frac{x' - x + r \tan \phi_d}{X_d} \right] \times \exp \left(-j \frac{4\pi}{\lambda} \Delta R \right) \cdot \exp \left[\frac{2\alpha}{c^2} (r' - r - \Delta R)^2 \right] \quad (1)$$

replaces eq.(22) in Sect. 1.1. In eq.(1), see Fig. 1, the azimuth footprint X_d in squinted geometry is given by:

$$X_d = \frac{\lambda r}{L \cdot \cos^2 \phi_d} \quad (2)$$

As usual:

- (x, r) are the azimuth and range coordinates of the generic illuminated target
- $r' = ct/2$ is the range signal sampling coordinate (c being the speed of the light);
- x' is the sensor azimuth position;
- λ is the carrier wavelength;
- $w(\cdot)$ is the antenna ground illumination pattern;
- L is the effective azimuth length of the physical antenna;
- $\Delta R = R - r$, R being the sensor to target distance.

Examination of eq.(1) shows that it coincides with the standard, i.e., in the absence of squint, impulse response of eq.(22) in Sect. 1.1, except for the argument of the ground illumination function $w[\cdot]$.

It is interesting to note that $w[\cdot]$ does not play any role in the evaluation of the stationary phase points when FT of (1) is addressed. Accordingly evaluation of FT of (1) can be easily carried out along the lines described in Chapter 1, Appendix I, since stationary phase points calculated in non squinted case are equal to those for the squinted case; it is easy to show that in this latter case we have [4]:

$$G(\xi, \eta, r) = \text{rect} \left[\frac{\eta}{\Omega_r} \right] \text{rect} \left[\frac{\xi - \xi_d}{\Omega_x} \right] \times \exp \left[j \frac{\eta^2}{4b} \right] \cdot \exp \left[-j \left(\sqrt{\bar{\eta}^2 - \xi^2} - \bar{\eta} \right) r \right] \quad (3)$$

where

$$\xi_d = \bar{\eta} \sin \phi_d \quad (4)$$

and, as usual, $\bar{\eta} = \eta + 4\pi/\lambda$; description of other symbols in eq.(3), already introduced in previous chapters, is addressed in Table of Symbols.

Equation (3) represent the SAR system TF in the general case of squinted acquisition, and differs from that provided in Chapter 1, eq. (28), only for the presence of the squint term ξ_d in the ξ dependent $\text{rect}(\cdot)$ function.

According to eq.(3) the ξ -dependent component of the spectrum is still band limited to the bandwidth Ω_x , but now its central spatial frequency ξ_d (known as the Doppler Centroid when converted in Hz) is no more zero and is ϕ_d -dependent, see eq.(4).

It is clear that precise and efficient SAR focusing of data acquired in the absence of track deviations, but in the presence of squint, can be carried out in the 2-D Fourier domain along the lines shown in Sect. 1.3, provided that the new expression (3) of the SAR system TF is considered [2], [4].

In particular, equivalently to the standard processing chain described in Sect. 1.3, SAR focusing in the presence of squint is aimed at compensating phase distortions of the system TF of eq.(3). This compensation performs, first of all, the range compression, i.e., compensation of the $\eta^2/4b$ phase term in eq. (3). This operation, following the analysis shown in Sect. 1.3, leads to the following expression of the data in the spatial (x', r') domain [4]:

$$h(x', r') = \iint dx dr \gamma(x, r) \exp\left(-j \frac{4\pi}{\lambda} R\right) \times \\ \times w^2 \left(\frac{x' - x + r \tan \phi_d}{X_d} \right) \text{sinc} \left[\frac{\Omega_r}{2} (r' - R) \right] \quad (5)$$

The target to distance R may be expanded along x' around the value $x' = x - r \tan \phi_d$, and the argument of the $\text{sinc}(\cdot)$ function in eq.(5) can be rewritten as follows:

$$r' - R \approx \\ r' - \frac{r}{\cos \phi_d} + \sin \phi_d (x' - x + r \tan \phi_d) - \frac{\cos^2 \phi_d}{2r} (x' - x + r \tan \phi_d)^2 \quad (6)$$

Equation (6) represents the curve along which the range-compressed point target response, which can be easily obtained from eq.(5) by letting $\gamma(x, r) = \delta(x - x') \delta(r - r')$, is spread in the presence of squint. It exhibits appearance of two effects: *range walk* and *range curvature*. The former is

4.1 SAR squinted data focusing in the absence of track deviations 153

described by the linear term (not present in the absence of squint, i.e. $\phi_a=0$), and the latter by the quadratic one.

It is clear that compensation of residual phase distortion term of eq.(3) corrects the Range Cell Migration (RCM) effect in both its linear (Range Walk, shortly RW) and non-linear (Range Curvature, shortly RC) components; accommodates the azimuth focus depth and performs the azimuth compression. Note that range dependent TF compensation can be efficiently carried out, up to high squint angles, by performing a spectral interpolation or equivalently by using fast scaled inverse FT along the lines shown in Section 1.3.

4.2 SAR focusing in conical geometry

In the following we shortly review the role of reference geometry in SAR processing.

Processing procedure briefly described in the previous sub-Section, is implemented, in 2-D Fourier Domain, with respect to the usual cylindrical reference system: in this case, after data focusing operation, each target is imaged (with a finite resolution depending by the used SAR system) at the azimuth and the range position corresponding to a cylindrical processing (output) geometry. In radar jargon this is referred to as Zero Doppler¹ (ZD) geometry Wave Number (ZD-WN) processing.

Nevertheless the SAR raw data processing operation can be generalized by referring to conical processing (output) geometry [1]. In order to clarify this point, let us consider the cylindrical and the conical geometries shown in Figs.2 and 3, respectively. In this case, x_{cy} and r_{cy} are the target spatial coordinates in the usual cylindrical reference system (x_{cy}, r_{cy}, θ) , the axis of which coincides with the antenna flight path (Fig.2). Moreover, x and r are the target coordinates in the conical reference system (x, r, θ) of Fig.3, wherein the axis again represents the antenna trajectory and the conic aperture is given by the angle ϕ_p . Transformations between the two reference systems are given by:

¹ A very popular interpretation of the synthetic antenna concept is the one based on *Doppler frequency* shift. However, we must state that this concept is not necessary for developments and implementation of SAR processing algorithms. As far as the SAR image generation is concerned, the radar platform could stop at each transmission point, without any impact in the data processing operation [4]. We underline that here and in the following the utilization of the common radar jargon do not implies in any way the use of the *Doppler frequency* shift concept.

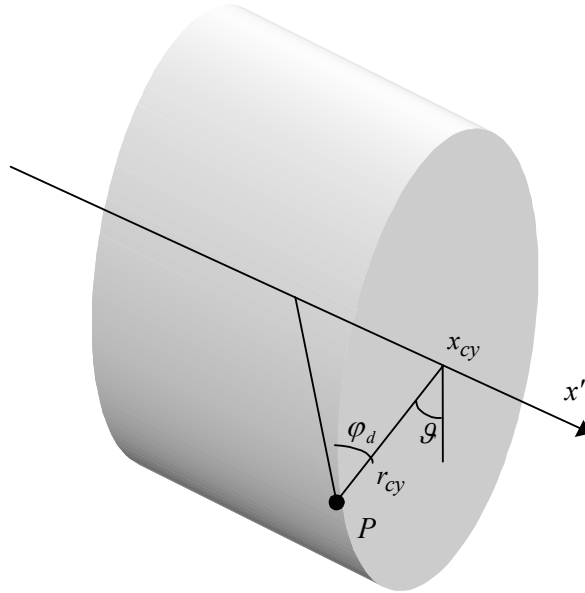


Figure 2 Cylindrical processing geometry. Axis coincides with flight path. Target coordinates are (x_{cy}, r_{cy}, θ) .

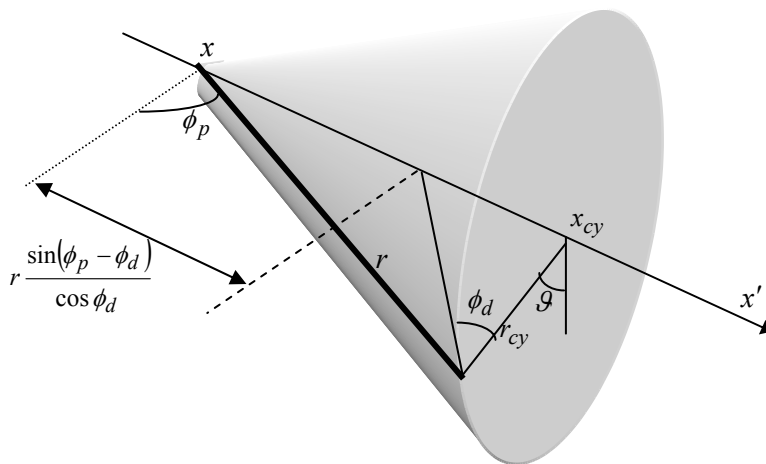


Figure 3 Conical processing geometry. Axis coincides with flight path. Target coordinates (x, r, θ) are defined with respect to conical angle ϕ_p .

$$r_{cy} = r \cos \phi_p \quad (7)$$

$$x_{cy} = x + r \sin \phi_p \quad (8)$$

Hereafter we refer to ϕ_p , which defines the conical reference system, as the processing angle and to the squint angle ϕ_d as the acquisition angle. Let us note that the common cylindrical reference system represents a particular case ($\phi_p=0$) of the more general conical reference system (see eqs.(7), (8) and Figs. 2, 3).

In the reference system of Fig. 3, we have the usual expression for the raw data:

$$h(x', r') = \iint dx dr \gamma(x, r) \exp\left(-j \frac{4\pi}{\lambda} r\right) g(x' - x, r' - r, r) \quad (9)$$

where $\gamma(x, r)$ is now the scene reflectivity function in the conical reference system. In this case, the expression of the impulse response function is given by [1]:

$$g(x' - x, r' - r, r) = \text{rect}\left[\frac{r' - r - \Delta R}{c\tau/2}\right] w^2 \left[\frac{x' - x - r \cdot d(\phi_p, \phi_d)}{X_d}\right] \times \exp\left(-j \frac{4\pi}{\lambda} \Delta R\right) \cdot \exp\left[\frac{2\alpha}{c^2} (r' - r - \Delta R)^2\right] \quad (10)$$

where

$$X_d = \frac{\lambda r \cos \phi_p}{L \cdot \cos^2 \phi_d} \quad (11)$$

$$d(\phi_p, \phi_d) = \frac{\sin(\phi_p - \phi_d)}{\cos \phi_d} \quad (12)$$

$$\Delta R(x' - x, r) = R(x' - x, r) - r \quad (13)$$

$$R(x' - x, r) = \sqrt{(r \cos \phi_p)^2 + (x' - x - r \sin \phi_p)^2} \quad (14)$$

Note that the target-to-antenna distance (14) has been transformed to the adopted conical coordinates by means of the transformation rules (7) and (8).

It can be shown, along the lines described in Chapter 1, Appendix I, that FT of eq.(10) leads to [1]:

$$G(\xi, \eta, r) = \text{rect}\left[\frac{\eta}{\Omega_r}\right] \text{rect}\left[\frac{\xi - \xi_d}{\Omega_x}\right] \times \exp\left[j\frac{\eta^2}{4b}\right] \cdot \exp\left[-j\left(\sqrt{\tilde{\eta}^2 - \xi^2} \cos\phi_p - \tilde{\eta}\right)r - j\xi r \sin\phi_p\right] \quad (15)$$

Some considerations about eq.(15) are now in order.

First of all we note that eq.(15) describes a generalized SAR system TF: by setting $\phi_p=0$ we obtain the standard expression for the SAR TF in the standard cylindrical reference system of (3).

Furthermore, it is clear that, equivalently to the standard cylindrical geometry WN focusing [2],[4], SAR processing in a conical geometry, i.e., $\phi_p \neq 0$, is aimed at compensating the phase distortion of the system TF described in eq.(15). This compensation performs the range compression; corrects both Range Walk and Range Curvature effect; accommodates the azimuth focus depth and performs the azimuth compression. Again, range dependent TF compensation can be efficiently carried out by using fast scaled inverse FT or, equivalently, by performing the following spectral interpolation:

$$\eta' \rightarrow \sqrt{\tilde{\eta}^2 - \xi^2} \cos\phi_p + \xi \sin\phi_p - \frac{4\pi}{\lambda} \quad (16)$$

which, similarly to the ZD case [8] [9], accounts for the non linear mapping, often referred to as *Stolt Mapping* (see Sect. 1.3.3.) of the range frequencies of the spectrum of $\gamma(\cdot)$.

As a matter of fact, we observe that the mapping of eq.(16) can be separated in two steps:

$$\eta' \rightarrow \sqrt{\tilde{\eta}^2 - \xi^2} \cos\phi_p - \sqrt{(4\pi/\lambda)^2 - \xi^2} \cos\phi_p \quad (17)$$

$$\eta'' \rightarrow \sqrt{(4\pi/\lambda)^2 - \xi^2} \cos\phi_p + \xi \sin\phi_p - \frac{4\pi}{\lambda} \quad (18)$$

It is easy to show [1] that the spectral interpolation (17) corrects the Range Cell Migration (RCM) effect in both its linear (RW) and non-linear (RC) components, whereas the residual mapping (18) accommodates the azimuth focus depth and performs the azimuth compression.

We underline that the standard “orthogonal” (ZD) processing procedure is a particular case ($\phi_p=0$) within this extended conical description. Furthermore in [1] it is shown that in order to minimize phase aberrations in the focused image, the most convenient processing geometry is the one closest to the acquisition geometry: in the following (using again the common radar jargon) we refer to this strategy, i.e., $\phi_p=\phi_a$, as Acquisition Doppler (AD) WN processing (AD-WN).

In conclusion, we can say that according to [1], in the absence of track deviations, extension of the standard 2-D Fourier SAR processing from a cylindrical geometry (WN-ZD processing) to a conical geometry can be easily carried out, and allows improving the accuracy of SAR focused imaged when raw data are acquired in squinted geometry.

In the following we explore the possibility to extend the MOCO procedure shown in Sect.3.1 to conical geometry.

4.3 Standard MOCO in conical geometry

As shown in Chapters 2 and 3, raw data acquired in the presence of track deviations are corrupted by the following term:

$$\delta R(x', x, r) = R_n \left[\sqrt{1 + \frac{\bar{\mathbf{d}} \cdot \bar{\mathbf{d}}}{R_n^2} - 2 \frac{\bar{\mathbf{d}} \cdot \hat{\mathbf{I}}}{R_n}} - 1 \right] \quad (19)$$

where, as usual (see Sect 3.7), R_n is the sensor-to-target distance with respect to the nominal trajectory; $\bar{\mathbf{d}}(x')$ is the vector, lying in the plane orthogonal to nominal flight track, that accounts for platform displacements from the nominal trajectory, $\hat{\mathbf{I}}(x-x', \mathcal{G}(x, r))$ is the unit line-of-sight vector; ‘ \cdot ’ denotes the vector inner product.

As already noted, compensation of the motion error (19), depending on both the sensor position (through x') and the location of the illuminated target (through x, r), would require a space variant filtering tailored to each target. Unfortunately, this operation is enormously time consuming, so that in eq.(19) the center beam approximation:

$$\bar{\mathbf{d}}(x') \cdot \bar{\mathbf{I}}(x-x', \mathcal{G}(x, r)) \approx \bar{\mathbf{d}}(x') \cdot \bar{\mathbf{I}}(0, \mathcal{G}(x', r')) = \delta r_r(x', r') \quad (20)$$

is commonly adopted, see Sect. 3.7.

As shown in Chapter 3, compensation of the motion error (20) is carried out in two steps [5]-[7] along the scheme introduced in Sect. 3.1 and reported in Fig. 4 for the sake of clearness. First of all, compensation of the middle range motion error, usually referred to as *first order* MOCO, is

carried out after the range compression step. Then, a phase compensation of the range-variant motion error, usually termed *second order* MOCO, is accomplished after the RCM compensation, just before the azimuth compression.

We can observe that, in the general scheme of Fig.4, motion error correction operations, highlighted with the dashed box, involve, basically, multiplications in the spatial domain (see Sect 3.1): implementation of such operations in a conical geometry thus represents not a difficult task.

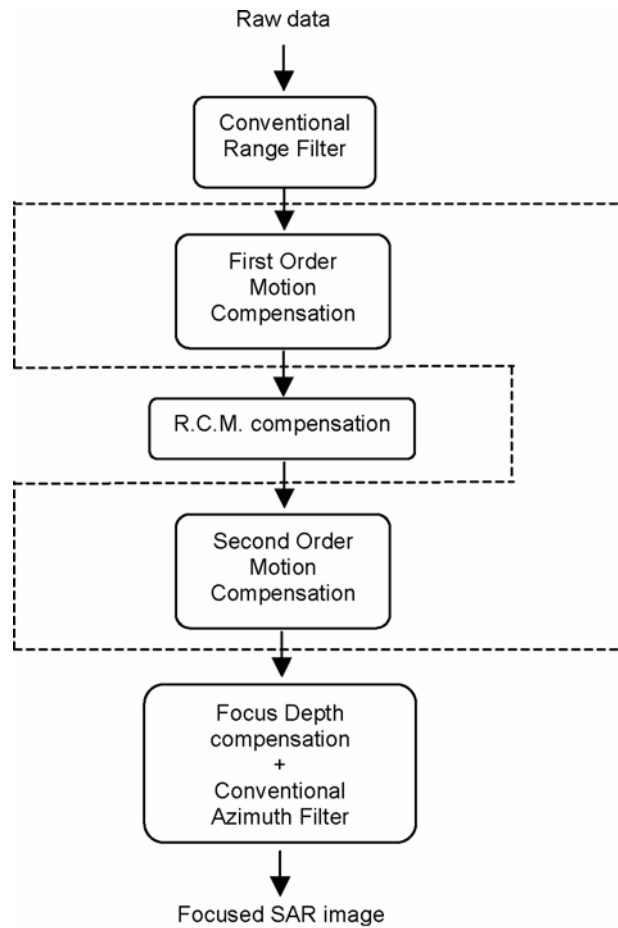


Figure 4 Block diagram of SAR processor with integrated Motion Compensation. Additive Motion Compensation terms with respect to the conventional SAR processor are highlighted with the dashed box.

Moreover, RCM compensation, as well as azimuth depth accommodation and azimuth compression, depend on the chosen processing geometry according to eqs. (17) and (18). Accordingly, extension of the general scheme of Fig.4, to any processing geometry can be easily carried out by means of the spectral interpolations described by eqs. (17) and (18), which can be efficiently performed via fast scaled FT [1].

Following the discussion in Sect.4.2, it is convenient to let $\phi_p=0$ in eqs. (17) and (18) when SAR raw data are acquired in the presence of track deviations, but in the absence of squint.

In this case, as shown in Sect 3.7, RCM compensation allows the impulse response function to fit isomoco-lines (lines where the approximation in (20) is minimized) before second order MOCO and, therefore, to limit the effect of center beam approximation.

To better emphasize this point, deeply analyzed in Sect. 3.7, we show in Fig.5 the difference between the left (space variant) and the right (space invariant) terms in (20) for the SAR system geometry of Table I, a target located at the scene center and the platform height variation depicted in Fig.6. It is noted that the direction where the minimum approximation is reached coincides with the azimuth direction.

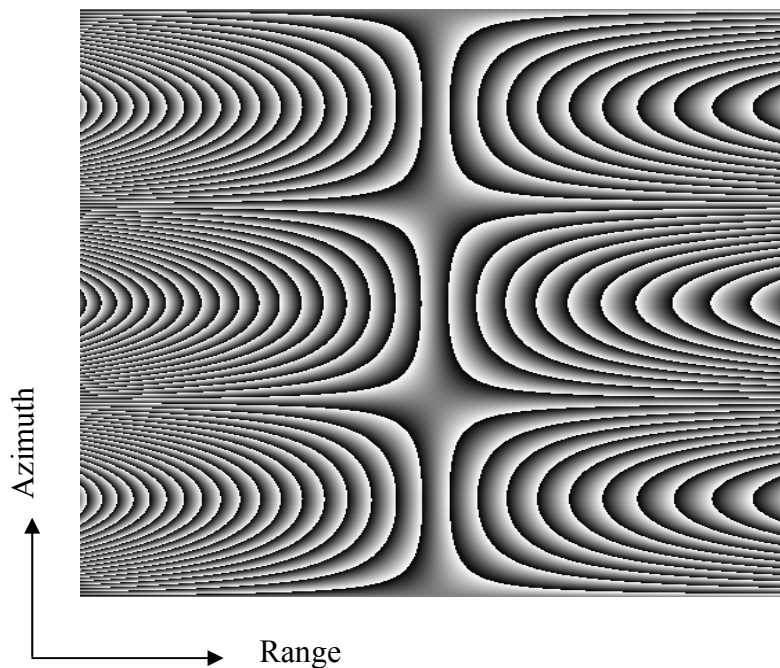


Figure 5 Phase difference between space invariant and space variant motion compensation correction: each fringe correspond to 4π rads

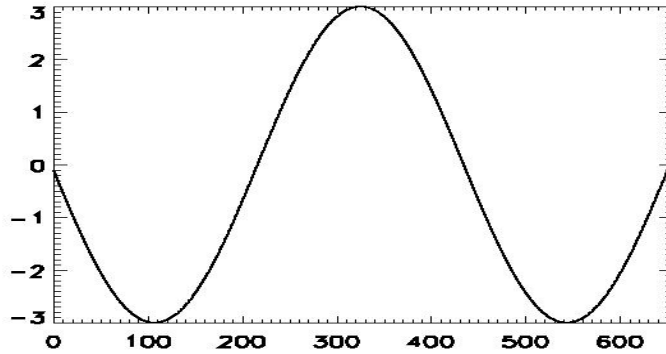


Figure 6 Height deviation [m] vs the azimuth [m].

Let us now move to consider trajectory deviations in the presence of squint. In this case, as explained in Sect. 3.7, appearance of linear components in the isomoco curves is registered; accordingly, the direction of isomoco lines becomes dependent on the vector displacement orientation, so that isomoco lines, in general, no longer coincide with the azimuth direction. Accordingly, RCM compensation, independently of the adopted processing geometry, does not allow, in this case, the impulse response function to fit isomoco-lines, so that effects of center beam approximation may be strong, and significant defocusing in the presence of track drifts can be registered (see Sect. 3.7, Figs. 19 and 20).

It is clear that standard two step MOCO procedure [5]-[7] of Fig. 4 is not able to deal both with squint and track deviations [7]; moreover, extension of such a processing procedure to conical geometry is possible, but ineffective, since the direction of the isomoco lines does not depend on the adopted processing geometry, and RCM migration compensation, independently of the adopted processing geometry, does not allow, in the presence of squint, the impulse response function to fit isomoco-lines

TABLE I Simulated Sensor Parameters

Nominal height	3000 m	Sampling Frequency	100 MHz
Midrange coordinate	4984 m	Chirp bandwidth	90 MHz
Wavelength	3.14 cm	Chirp duration	5 μ s
Platform velocity	80 m/s	Azimuth resolution	0.22 m
PRF	500 Hz	Doppler bandwidth	370 Hz
Synthetic aperture length	360 m	Number of azimuth samples	4096

4.4 Motion compensation in the presence of squint

In this section we present a new WN based algorithm for Motion compensation of airborne squinted data.

Differently from the non-squinted case, we now describe the actual sensor position through a vector $\vec{d}(x')$ lying in the plane rotated with respect to the boresight direction by an angle equal to the squint angle ϕ_a (see Fig. 7). Isomoco lines would then become skewed and isomoco lines follow this skew (see Sect. 3.7). In this case their direction no longer depends on the displacement orientation; however, differently from the non squinted case, now the direction of isomoco lines does not coincide with the azimuth direction. In order to highlight this effect we show in Fig. 7 the same difference shown of Fig.6 but in the presence of a squint angle $\phi_a = 40^\circ$.

It is noted that now the direction of the isomoco lines, i.e., the direction where the minimum approximation in (20) is reached, follows the range walk direction.

Accordingly, similarly to the standard MOCO procedures [5]-[7] introduced in Chapter 3 and briefly discussed in Sect. 4.3, also in the presence of an acquisition squint angle $\phi_a \neq 0$ it is convenient to adopt a two step MOCO approach.

Still, second order MOCO must be carried out after the rectification of the target response, inside the illumination interval, along a direction where the center beam approximation in (20) (now carried out by considering the

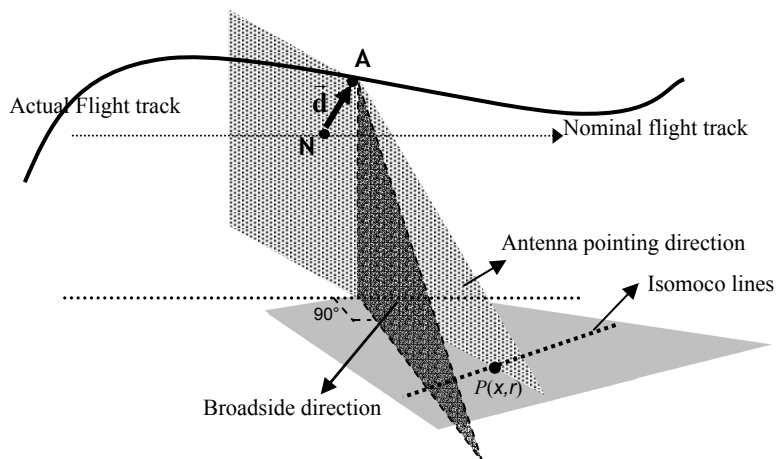


Figure 7 Height deviation [m] vs the azimuth [m].

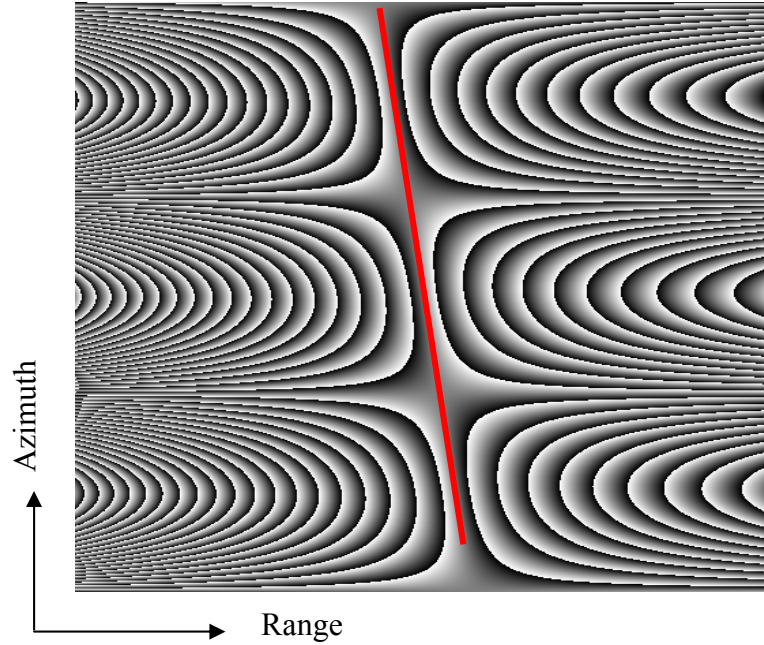


Figure 8 Same as Fig. 5, but in the presence of a squint angle $\phi_d=40^\circ$. Range walk direction is also plot (red line)

presence of the squint angle $\phi_d \neq 0$) is minimized in terms of phase residual errors. However, differently from the no-squinted acquisition case, now the direction where the minimum approximation is reached does coincide with the range walk direction (red line in Fig 8).

Accordingly, it is convenient to carry out the RCM compensation in two separate steps: we first accommodate range curvature via the following SM modification (see Appendix I):

$$\eta' \rightarrow \sqrt{\eta^2 - \xi^2} \cos \phi_p - \sqrt{(4\pi/\lambda)^2 - (\xi - \eta \sin \phi_d)^2} \cos \phi_p + \eta \sin \phi_p \sin \phi_d \quad (21)$$

where the general case of a conical processing reference has been considered. At this point the target response is rectified along the range walk direction. Accordingly the data are back transformed in the spatial domain and second order MOCO can be successfully applied, since the aberrations induced by center beam approximation (20) are now minimized.

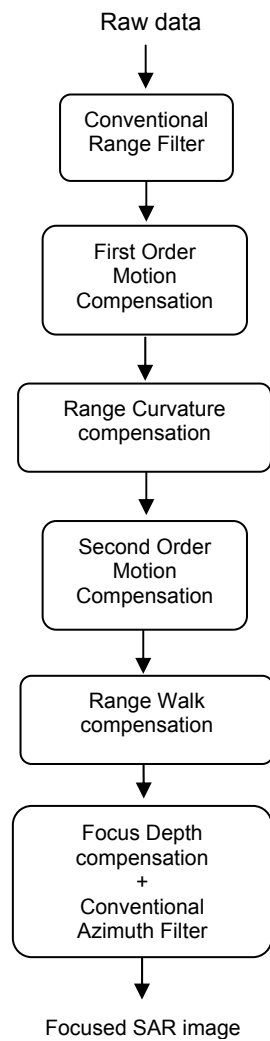


Figure 9 Block diagram of the proposed SAR processor for Motion Compensation of squinted data.

Finally, after transforming the data in the azimuth-frequency range-frequency (ξ, η) domain, the residual *Stolt Mapping* :

$$\begin{aligned} \eta'' \rightarrow & \sqrt{(4\pi/\lambda)^2 - (\xi - \eta \sin \phi_d)^2} \cos \phi_p \\ & + (\xi - \eta \sin \phi_d) \sin \phi_p - \frac{4\pi}{\lambda} \end{aligned} \quad (22)$$

is applied to the data to compensate for the range walk and carry out the azimuth focusing, including the focus depth.

Additional considerations on the proposed approach, the basic structure of which is depicted in Fig. 9, are now in order.

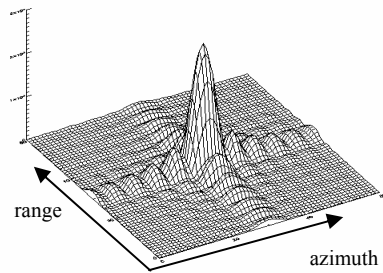
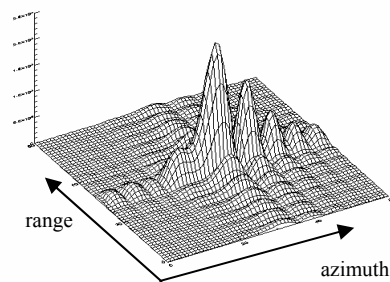
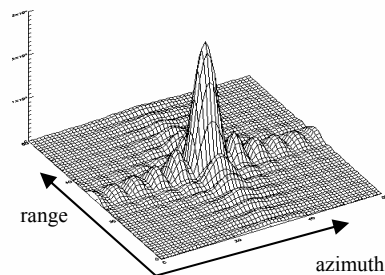
First of all, differently from Fig. 4 [5]-[7], in this case RCM compensation is carried out in two different steps. It is evident that the proposed algorithm generalizes for $\phi_d \neq 0$ the Standard MOCO procedure [5]-[7].

Furthermore, the proposed approach is very general, in the sense that it may process the data in any conical geometry; of course, following the discussion of Sect. 4.2, it is convenient to carry out AD processing, by setting $\phi_p = \phi_d$ in (21) and (22). Moreover, the spectral interpolation operations described by (21) and (22) may be, in principle, carried out in more efficient ways, which are not investigated in this chapter and are matter of future work.

Finally, to validate the effectiveness of the proposed MOCO algorithm, we compare it to the standard one of [5]-[7], by using simulated data relative to the SAR system of Table I.

A constant squint angle $\phi_d = 5^\circ$ has been fixed; the motion error plotted in Fig. 6. A 3D representation of the final PSF plot obtained by using the proposed MOCO algorithm (Fig. 10a) and the standard one [5]-[7] (Fig. 10b) is shown.

To appreciate the focusing capability of the proposed algorithm we show in Fig. 10c the PSF in the absence of motion errors, with the AD-WN processor described in Sect. 4.2. No differences could be appreciated with respect the results of Fig. 10a, thus confirming the validity of the shown theory.

**Figure 10a****Figure 10b****Figure 10c**

Point Spread Function obtained by processing simulated raw data acquired with $fd=5^\circ$ in the presence (10a and 10b) of motion error of Fig.6 and in the absence of any motion error (10c). Fig. 10a is obtained by using the proposed algorithm; Fig 10b is obtained by using the standard MOCO algorithm.

4.5 Summary

In this chapter the problem of airborne SAR focusing in the presence of track deviations is addressed.

It is shown that, in the presence of squint, standard WN based MOCO [5]-[7] approach is ineffective, even when it is carried out in the acquisition geometry.

A new WN based algorithm for Motion Compensation of squinted raw data acquired with motion errors is proposed.

The key point of this algorithm consists in the separation of Range Cell Migration compensation in two different steps: Range Curvature correction, to be carried out, as usual, *before* the second order MOCO; and Range Walk correction, to be implemented, differently from the standard MOCO approach [5]-[7], *after* the second order MOCO. This procedure allows minimizing the aberrations induced by center beam approximation, adopted in [5]-[7], thus reducing defocusing effects in the final SAR image.

Simulation results aimed at assessing the effectiveness of the presented theory are also included.

The presented algorithm operates in the Wave-Number domain and may process the data in any conical geometry: its efficient implementation via fast scaled FT is under investigation.

APPENDIX I

In this Appendix we derive the expression of the spectral mapping that allows correction of Range Curvature effect. The general conical reference system of Fig. 3 is considered; moreover, the presence of squint is assumed.

Let us refer to the SAR data expression (5) after the range-compression step and consider the reference system of Fig. 3; in this case the new expression:

$$h(x', r') = \iint dx dr \gamma(x, r) \exp\left(-j \frac{4\pi}{\lambda} R\right) w^2\left(\frac{x' - x - rd}{X_d}\right) \text{sinc}\left[\frac{\Omega_r}{2}(r' - R)\right] \quad (23)$$

replaces eq. (5). In eq. (23) use of symbols defined in (11)-(14) has been made. The spectrum of eq.(23) is given by

$$H(\xi, \eta) = \iint dx dr \gamma(x, r) \exp[-j(4\pi/\lambda)r] M(\xi, \eta, r) \exp[-j\xi x - j\eta r] \quad (24)$$

where $M(\cdot)$ coincides, but for the η^2 dependent tem, with the SAR TF of eq.(15):

$$M(\xi, \eta, r) = \text{rect}\left[\frac{\eta}{\Omega_r}\right] \text{rect}\left[\frac{\xi - \xi_d}{\Omega_x}\right] \times \exp\left[-j\left(\sqrt{\bar{\eta}^2 - \xi^2} \cos\phi_p - \bar{\eta}\right)r - j\xi r \sin\phi_p\right] \quad (25)$$

Let us refer to the range compressed SAR signal of (23). The R term may be now expanded along x' around the value $x' = x + r \cdot d(\phi_p, \phi_d)$, and the argument of the sinc(\cdot) function in eq. (23) can be now rewritten as follows:

$$r' - R = r' - r \frac{\cos\phi_p}{\cos\phi_d} + \sin\phi_d \left[x' - x - r \cdot d(\phi_p, \phi_d) \right] - \Delta_{RC} \quad (26)$$

Equation (26) represents, similarly to eq.(6), the curve along which the range-compressed point target response is spread in the presence of squint; in this case, (x, r) are referred to the conical reference system of Fig.3,

As already noted *range walk* effect is described by the linear term in (26), whereas *range curvature* effect by the Δ_{RC} one.

It is clear that the expression of the range compressed data which accounts for only the *range walk* effect coincides with eq.(23) except for the

argument of the $\text{sinc}(\cdot)$ function, which has not to show the presence of the Δ_{RC} term related to the *range curvature* effect. In other words the expression of the range-compressed data after the *range curvature* correction step is the following:

$$h(x', r') = \iint dx dr \gamma(x, r) \exp\left(-j \frac{4\pi}{\lambda} R\right) w^2\left(\frac{x' - x - rd}{X_d}\right) \text{sinc}\left[\frac{\Omega_r}{2} \left(r' - r \frac{\cos \phi_p}{\cos \phi_d} + \sin \phi_d (x' - x - rd)\right)\right] \quad (27)$$

and, therefore, its two-dimensional spectrum, given by the two dimensional FT of eq.(27), is the following:

$$H(\xi, \eta) = \text{rect}\left[\frac{\eta}{\Omega_r}\right] \iint dx dr \gamma(x, r) \exp\left[-j\eta \left(r \frac{\cos \phi_p}{\cos \phi_d}\right)\right] \times \int dx' w^2\left(\frac{x' - x - rd}{X_d}\right) \exp\left(-j \frac{4\pi}{\lambda} R\right) \exp[j\eta \sin \phi_d (x' - x - rd)] \exp[-j\xi x'] \quad (28)$$

Letting $x' - x - rd = p$, the last integral of eq.(28) can be rewritten as:

$$\exp[-j\xi(x + rd)] \times \int dp w^2\left(\frac{p}{X_d}\right) \exp\left(-j \frac{4\pi}{\lambda} R(r, p)\right) \cdot \exp[j\eta \sin \phi_d \cdot p] \cdot \exp[-j\xi p] \quad (29)$$

where

$$R(r, p) = \sqrt{(r \cos \phi_p)^2 + (p - r \cos \phi_p \tan \phi_d)^2}. \quad (30)$$

The integral of eq.(29) may be approximated, but for nonessential constant factors, via the stationary phase method as follows:

$$\exp[-j\xi(x + rd)] \times w^2\left(\frac{p_s}{X_d}\right) \exp\left(-j \frac{4\pi}{\lambda} R(r, p_s)\right) \exp[j\eta \sin \phi_d p_s] \exp[-j\xi p_s], \quad (31)$$

where:

$$p_s = r \cos \varphi_p \tan \varphi_d - \frac{(\xi - \eta \sin \varphi_d) r \cos \varphi_p}{\sqrt{\left(\frac{4\pi}{\lambda}\right)^2 - (\xi - \eta \sin \varphi_d)^2}} \quad (32)$$

is the stationary phase point obtained by solving in p the following equation:

$$\frac{4\pi}{\lambda} \frac{\partial R}{\partial p} + \xi - \eta \sin \varphi_d = 0. \quad (33)$$

Substituting eq. (32) in eq.(31) we can solve eq.(29) and rewrite eq.(28) as follows:

$$\begin{aligned} H(\xi, \eta) &= \\ &= \iint dx dr \gamma(x, r) \exp[-j(4\pi/\lambda)r] N(\xi, \eta, r) \exp[-j\xi x - j\eta r] \end{aligned} \quad (34)$$

where:

$$\begin{aligned} N(\xi, \eta) &= \text{rect}\left[\frac{\eta}{2\Omega_r}\right] \text{rect}\left[\frac{\xi - \xi_d}{2\Omega_x}\right] \exp[j\bar{\eta}r] \times \\ &\quad \times \exp\left[-jr \cos \varphi_p \sqrt{\left(\frac{4\pi}{\lambda}\right)^2 - (\xi - \eta \sin \varphi_d)^2}\right] \\ &\quad \times \exp[-j\eta r \cos \varphi_p \cos \varphi_d] \exp[-j\xi r \sin \varphi_p] \end{aligned} \quad (35)$$

Range Walk correction in WN domain consists in a spectral interpolation leading from eq.(24) to eq.(34). It is easy to show that such an operation is described by the *Stolt Mapping* of (21).

References

- [1] G.Fornaro, E.Sansosti, R.Lanari and M.Tesauro; “Role of Processing Geometry in SAR Raw Data Processing”, IEEE Trans. Aerosp. Electron. Syst., 38, 2002.
- [2] G.Franceschetti, R.Lanari and E.S.Marzouk; “A new two dimensional squint mode SAR processor”, IEEE Trans. Aerosp. Electron. Syst., 32, 854, 1996.
- [3] G.W.Davidson and I.Cumming; “Signal properties of spaceborne squint-mode SAR”, IEEE Trans. on Geosci. Remote Sens., 35, 611,1997.
- [4] G.Franceschetti and R.Lanari; Synthetic Aperture Radar Processing, CRC PRESS, New York, 1999.
- [5] A.Moreira and Y.Huang; “Airborne SAR Processing of highly squinted data using a chirp scaling approach with integrated motion compensation”, IEEE Trans. on Geosci. Remote Sens., 32, 1994.
- [6] G.Fornaro; “Trajectory Deviations in Airborne SAR: Analysis and Compensation”, IEEE Trans. Aerosp. Electron. Syst., 35, July 1999.
- [7] E.Aliviazatos, A.Potsis, A.Reigber, A. Moreira and N. Uzunoglu; “SAR Processing with motion compensation using the extended wavenumber algorithm”, Proc. EUSAR, Ulm, 2004.
- [8] C. Cafforio, C. Prati and F.Rocca; “SAR data focusing using seismic migration techniques”, IEEE Trans. Aerosp. Electron. Syst, 27, 1991.
- [9] R.Bamler; “A Comparison of Range-Doppler and Wavenumber Domain SAR Focusing Algorithms”, .IEEE Trans. on Geosci. Remote Sens., 30, 1992.

Chapter 5

Airborne DIFSAR: Experiments with Real Data

As shown in Chapter 1, interferometric processing of repeat pass SAR data acquired by spaceborne platforms is a well established technique. It allows the generation of high accuracy products such as Digital Elevation Models (DEM). More recently substantial developments have been achieved in the contest of centimetric/millimetric accuracy ground deformation monitoring via the Multiple-Pass Differential SAR Interferometry technique [1].

This DIFSAR technique makes SAR sensors powerful instruments for forecasting environmental hazard on one hand [2], and for evaluation of environmental damages on the other [3]. Satellite DIFSAR allows, today, generating spatially dense surface deformation maps with centimeter to millimeter accuracy, with no environmental impact on the investigated areas. Furthermore, different algorithms have been recently proposed [4], [5] and successfully applied [6] to detect and follow the temporal evolution of deformations via the generation of time series.

Unfortunately, this powerful technique is strongly limited by the use of satellite SAR sensors.

Satellites orbits, indeed, are governed by celestial laws; this implies, first of all, that the repeat cycle of satellites (often referred to as *revisiting time*), after which the same region is imaged again, is fixed and cannot be changed in case of emergencies.

Furthermore, the satellite revisiting time is often rather long and hardly falls below the limit of one month, causing loss in interferogram coherence (see Chapter 1) and, so, in the accuracy we need for Earth's surface displacements.

Moreover, available spaceborne systems provide only a restricted offer in terms of usable operative frequencies.

Finally, orbits covered by remote sensing satellites, cannot allow North-South deformation detections; .

Accordingly, space-borne sensors could be not flexible enough to be really helpful in catastrophe management, and exploitation of a more flexible use of the DIFSAR technique is thus today needed.

In this context airborne SAR platforms could allow overcoming the above mentioned limits. With respect to spaceborne SAR systems, although

characterized by a lower imaging spatial coverage, airborne SAR systems assure spatial higher resolutions due to smaller acceptable dimensions of transmitting antennas and also have an extremely higher operative flexibility. As consequence, they allow using low-frequency systems and reducing the revisiting time to the order of few tens of minutes: these features are of key interests in some environmental risk monitoring areas such as those related to volcanic activity and ground slide movement monitoring.

Notwithstanding, airborne SAR processing may be an issue even for the generation of amplitude images. Problems arise mainly due to the presence of atmospheric turbulences that introduce trajectory deviations from the nominal straight flight. As far as the amplitude image generation is concerned, efficient frequency domain SAR focusing algorithms allow one to generate focused SAR images where geometric and radiometric resolution losses are negligible (see Sect. 3.1). However, phase inaccuracies may appear due to the presence of uncompensated motion errors (residual errors) caused by inaccuracies of the available DEM and/or of the Inertial Navigation Unit (INU). As discussed in Sect. 3.4, such errors do not impact the accuracy of single pass interferometric products because most of residual phase errors present in the two images cancel each other during the signal beating of the two interferometric channels. This is not the case for airborne repeat pass interferometry where residual errors at the two channels may be significantly different. Accordingly, uncompensated motion errors represent a major difficulty for the application of the differential interferometry technique to airborne SAR systems. These problems have been highlighted and quantified in terms of phase accuracy of the final images in Chapter 3. A possible remedy has been discussed in [7]; however, its application on airborne differential interferometry has been only partly successful [8].

In this work we show the result of a differential interferometry X-band experiment carried out by using the OrbiSAR system of Orbisat (Brazil), which is equipped by accurate INU system [9], [10]. Following the theoretical analysis shown in Chapter 3, the system shows enough position measurement accuracy to preserve the phase characteristics of the processed images. Theoretical results discussed in Chapter 3 have been fully confirmed by the obtained experimental results. Although based only on two repeated acquisitions, separated by a time interval of the order of few minutes, the obtained differential interferogram, which essentially show the absence of any ground deformations, confirms the high accuracy of the used SAR system and its potentialities for airborne multi pass DIFSAR monitoring.

5.1 Motion sensing system requirements

Let us consider the usual SAR system geometry in the plane orthogonal to the ideal flight track: (x, r) are azimuth and (slant) range coordinates of the generic scene scatter point P in a cylindrical reference system, the axis of which coincides, as usual, with the nominal trajectory; x' is the position of the illuminating antenna; \vec{d} is the displacement vector and $\delta r_r^a(x', r)$ is its projection onto the look direction (see Sect. 2.2) component along the target line of sight. Moreover, as usual, we denote with r' the range sampling coordinate associated to the fast time.

As shown in Sect. 3.1, starting from knowledge of the $\delta r_r^a(\cdot)$ term it is possible, by using proper Motion Compensation (MOCO) procedures, to compensate motion errors. Note that $\delta r_r^a(\cdot)$ can be computed starting from the measured trajectory deviations and the scene terrain profile. Accordingly, as we are unable to use the actual $\delta r_r^a(\cdot)$ term because of INU and GPS inaccuracies or DEM errors, the adopted compensation term is the measured $\delta r_r^m(\cdot)$ term. Errors in evaluation of the airborne position, as well as errors in evaluation of the topographic height, may affect the accuracy of the final images, as discussed in Chapter 3. Such errors, referred to as residual errors, generally do not impact the accuracy of single pass interferometric products because their effects are mostly compensated during the signal beating of the two interferometric channels, see Sect.3.4. Unfortunately, this may not be the case for airborne repeat pass interferometry where residual errors at the two channels can be significantly different, thus impairing the final interferogram accuracy. A quantitative analysis of the aberrations induced by residual errors on the final airborne interferogram accuracy is shown in Chapter 3, and summarized in the following.

In the case of airborne repeat pass interferometry, the final interferogram can be corrupted by a differential phase error, which passes from the raw data to the focused images. This error can be estimated and compensated on the final images as in [7].

Additionally, the final interferogram can be also affected by a differential phase artifact which is peculiar to the interaction between the SAR processing step and the different residual errors at the two channels. Despite the fact that this latter differential phase artifact cannot be compensated by using methods available in the literature, starting from the expected accuracy of the used position measurement system mounted onboard the aircraft, we can estimate the phase accuracy of resulting differential interferogram affected by the above mentioned differential phase artifacts, intrinsically generated by the SAR processing. This allows us to set

the limits on the accuracy of the used Motion Sensing Systems (MSS) mounted onboard the aircraft, when perfect knowledge of topography is assumed, and vice-versa.

As far as MSS accuracy is considered, as shown in Sect 3.6, the effects of linear uncompensated residual errors on airborne SAR images may be critical even for modern positioning instruments; on the contrary, quadratic residual errors generate phase artifacts which can be considered negligible when modern MSS are used. In particular, the rms interferometric phase artifact σ_φ is given by:

$$\sigma_\varphi = \frac{2\pi}{\lambda} \sqrt{6} \cdot r_0 \sigma_{\delta_e}^2 \quad (1)$$

where σ_{δ_e} is the rms value of the motion sensing instrument drift. Equation (1) fixes the measurement positioning system requirements for repeat pass airborne interferometric applications.

5.2 Experimental results

In this Section we show the results of an airborne differential interferometry experiment carried out by using the OrbiSAR system [9]. The Sensor parameters are collected in Table I.

The drift rms value of the used positioning instrument [10] is limited to the value $\sigma_{\delta_e} < 10^{-5}$.

In order to verify that the used navigation instruments fulfill the requirements of Sect.5.1, let us refer to Fig. 1 where, starting from the adopted SAR geometry of Table I, the rms interferometric phase artifact σ_φ is plotted, according to (1), versus the rms value σ_{δ_e} of the positioning instrument drift. It is recognized that the used positioning instruments lead to negligible phase artifacts.

The investigated test site is relative to the Ecuador area: three different flights in the same day have been carried out. No fast deformations are present in the monitored area. The images have been processed with respect to nominal tracks with a maximum normal baseline value of 5 m. During the Motion Compensation, a smoothed version of the low resolution SRTM DEM has been used to limit inaccuracies related to center-beam approximation.

TABLE I. SENSOR PARAMETERS

Nominal height	7010 m	Chirp duration	5 μ s
Range delay	60.2 μ s	Chirp bandwidth	45 MHz
Wavelength	3.12 cm	Range pixel spacing (s.l.)	1.5 m
Platform velocity	110 m/s	Number of range pixels	4096
Pulse Repetition Frequency	1644 Hz	Azimuth pixel spacing (s.l.)	0.27 m
Azimuth beam width	7.5 degs	Azimuth resolution (m.l.)	1 m

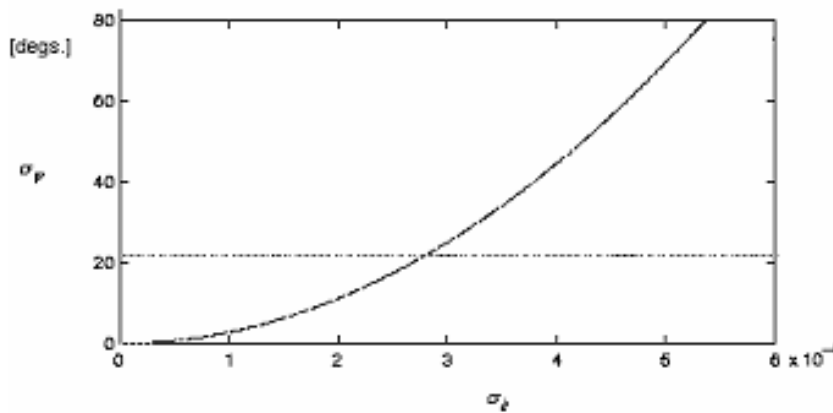


Figure 1 Rms interferometric phase artifact versus the rms value of the motion sensing instrument drift for the considered SAR geometry.

In Figs. 2 we show one processed SAR image of the illuminated area; in Fig.3 we show one wrapped differential interferogram obtained by applying the scheme of Fig. 12 in Chapter 1 (no phase unwrapping has been applied in this case) to two focused SAR images.

Some considerations about the differential interferogram of Fig.3 are now in order.

First of all, differently from the system used in [7], [8] and in line with the theoretical analysis presented in chapter 3, we do not observe any residual uncompensated phase error associated to uncompensated trajectory deviations that appears, see [7], [8], as phase undulations along the azimuth, almost constant in the range direction. Accordingly, we did not apply any residual trajectory deviation compensation procedure [7].

Furthermore, the differential interferogram of Fig. 3 is recognized to be noisy in some areas. This is certainly not surprising, considering that a vegetated area is present in the illuminated scene and decorrelation effects are thus expected even for revisiting time of a few hours, due to scattering property variations, between the two passes, induced by leaf movements. To highlight these effects, we show in Fig. 4 the coherence map relative to the interferogram of Fig.3. It is evident that over the vegetated area, a strong coherence loss is measured; moreover, it is interesting to observe that the high resolution SAR data of Figs. 2-5 allow clearly identify a river and a lake, characterized by low backscattered field in the SAR image of Fig.3, and by low levels of coherence in Fig. 4.

In the other areas of the monitored scene, the differential interferogram is mainly flat and no deformations are detected. Residual fringes, that cannot be associated to atmospheric variations, are observed in the top of the image. These fringes turn out to be correlated with the topography, however they are not residual topographic errors in the differential interferogram generation step but rather a consequence of the DEM smoothing during the compensation processing. Post processing phase compensation procedures and modifications of the motion compensation procedure to accommodate such phase inaccuracies are under testing.

In order to appreciate the quality of the obtained airborne differential interferogram, we show in fig. 3 an ERS differential interferogram in an area with absence of deformations. This interferogram was used to carry out a MP-DIFSAR analysis with ERS data that allowed monitoring several regional a localized ground deformation phenomena with an accuracy on the order of millimeter per year [5]. Comparing Figs. 3 and 5 we may recognize the congruence in terms of phase accuracy of the two differential interferograms and the improvements in terms of spatial resolution of the airborne (Fig.2) over the spaceborne (Fig.5) data.

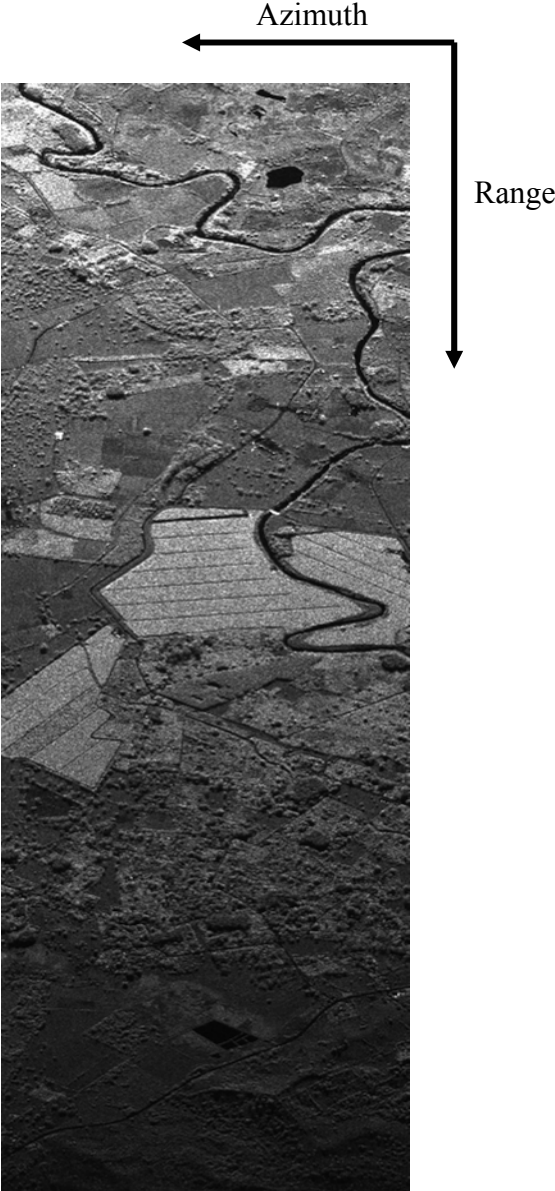


Fig. 2 Airborne SAR image of the monitored area.

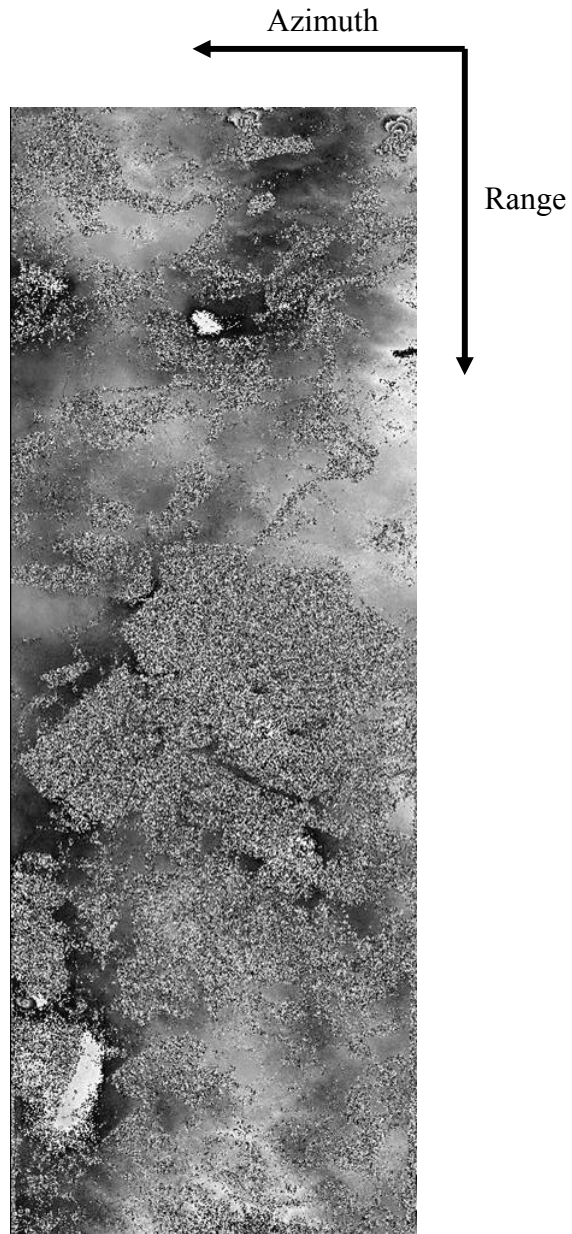


Fig. 3 Airborne differential SAR interferogram of the monitored area.

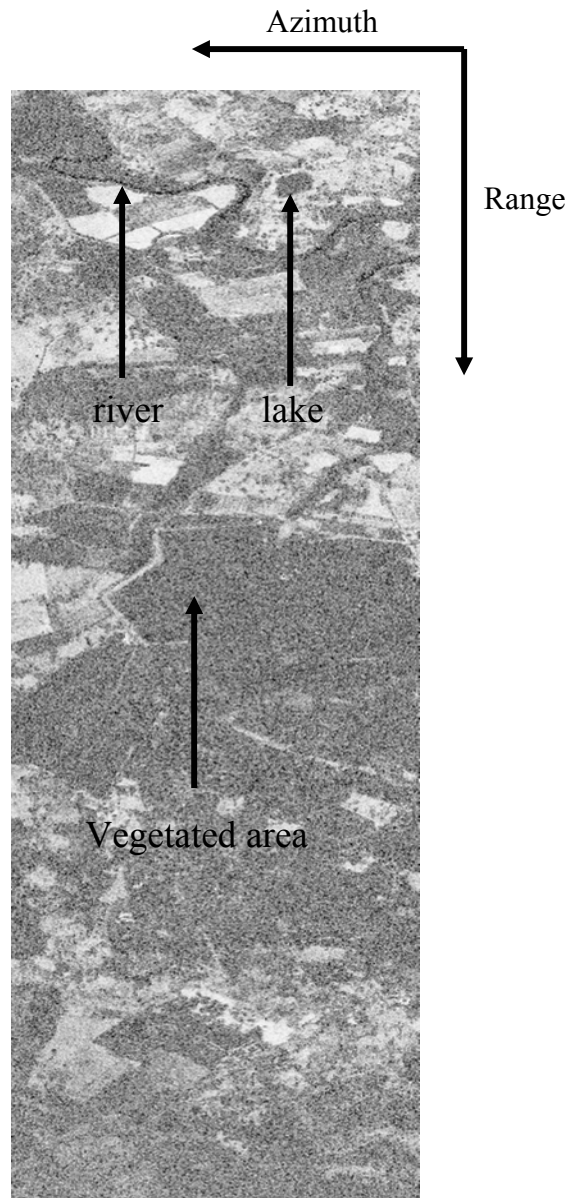


Fig. 4 Coherence map relative to the interferogram of Fig. 3.

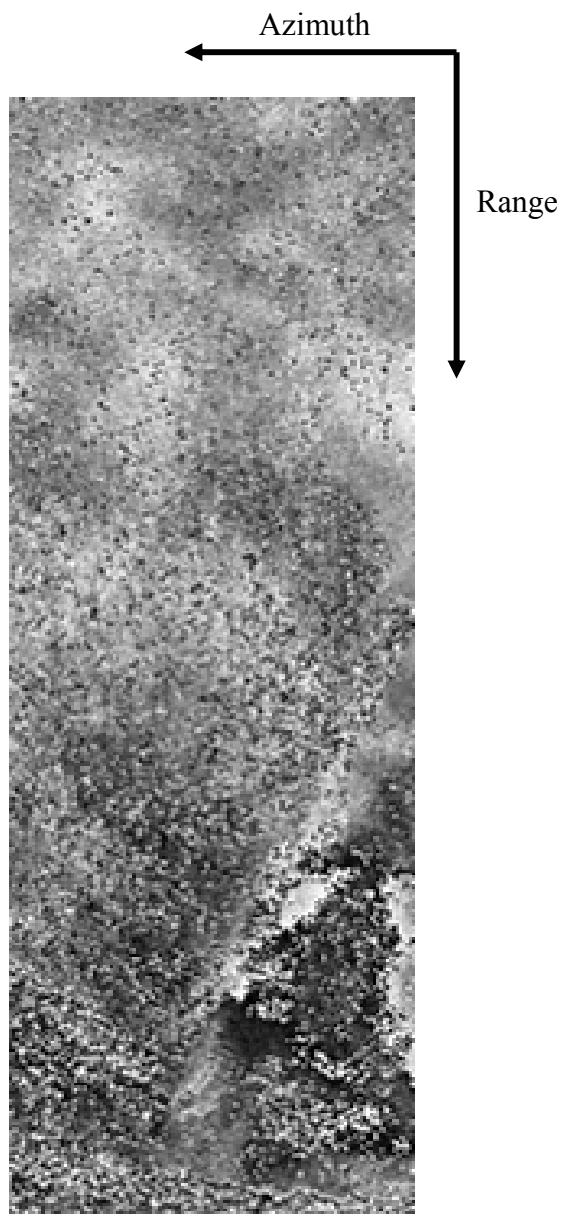


Fig 5 ERS tandem differential interferogram over an area with size similar to that in Fig.3

References

- [1] K.Gabriel, R.M. Goldstein and H.A.Zebker; "Mapping small elevation changes over large areas: Differential interferometry", J. Geophys. Res., 94, 1989.
- [2] D.Massonnet, P.Briole and A.Arnaud; "Deflation of Mount Etna monitored by spaceborne radar interferometry". Nature, London, 375, 567, 1995.
- [3] D.Massonnet, M.Rossi, C.Carmona, F.Ardagna, G.Peltzer, K.Feigl and T.Rabaute, "The displacement field of the Landers earthquake mapped by radar interferometry", Nature, 364, 1993.
- [4] A.Ferretti, C.Prati and F.Rocca; "Permanent scatterers in SAR interferometry", IEEE Trans. Geosci. Remote Sens., 39, 1, 2001.
- [5] P.Berardino, G.Fornaro, R.Lanari and E.Sansosti; "A new Algorithm for Surface Deformation Monitoring based on Small Baseline Differential SAR Interferograms", IEEE Trans. Geosci. Remote Sens., 40, 11, 2002.
- [6] A.Borgia, P.Tizzani, G.Solaro, M.Manzo, F.Casu, G.Luongo, A.Pepe, P.Berardino, G.Fornaro, E.Sansosti, G.P.Ricciardi, N.Fusi, G.Di Donna and R.Lanari, "*Volcanic spreading of Vesuvius, a new paradigm for interpreting its volcanic activity*", Geoph. Res. Letters, 32, L03303, doi:10.1029/2004GL022155.
- [7] A.Reigber and K.P.Papathanassiou; "Correction of residual motion errors in airborne repeat-pass interferometry", Proc. IGARSS, Sydney, 2001.
- [8] A.Reigber and R.Scheiber; "Airborne Differential SAR Interferometry: first results at L-band", IEEE Trans. Geosci. Remote Sens., 41, 6, 2003.
- [9] M.Rombach, A.Fernandes, D.Luebeck and J.Moreira; "Newest Technology for mapping using airborne interferometric synthetic aperture radar systems", Proc. IGARSS, Toulouse, 2003
- [10] Applanix technical product description;
http://www.applanix.com/html/products/prod_airborn_index.html

TABLE of Symbols

Symbol	Description
x	azimuth coordinate [m]
r	range coordinate [m]
ϑ	look angle [rad]
x'	azimuth coordinate in SAR data grid [m]
r'	range coordinate in SAR data grid [m]
R	target-to antenna distance [m]
ΔR	$R_n - r$
R_n	nominal target-to antenna distance [m]
δR	$R - R_n$
c	light speed [m/s]
λ	carrier wavelength [m]
f	carrier frequency [Hz]
Δf	transmitted Bandwidth [Hz]
τ	transmitted pulse duration τ [s]
b	$\frac{4\pi \Delta f}{\lambda f c \tau}$
a	chirp rate [rad/s ²]
L	effective antenna azimuth dimension [m]
L_r	effective antenna range dimension [m]
$w(\cdot)$	antenna illumination function in azimuth direction
X	azimuth footprint [m]
$\gamma(x,r)$	reflectivity pattern
$\bar{\gamma}(x,r)$	$\gamma(x,r) \cdot \exp(-j4\pi r/\lambda)$
$\hat{\gamma}(x',r')$	focused SAR image
Δx_{raw}	azimuth resolution of SAR raw data [m]
Δr_{raw}	range resolution of SAR raw data [m]
Δx	azimuth resolution of SAR focused image [m]
Δr	range resolution of SAR focused image [m]
$g(\cdot)$	SAR system impulse response
ξ	Fourier mate of x' [rad/m]
η	Fourier mate of r' [rad/m]
$\bar{\eta}$	$\eta + 4\pi/\lambda$
$G(\xi, \eta, r)$	SAR system transfer function
Ω_x	SAR system TF azimuth bandwidth [rad/m]
Ω_r	SAR system TF range bandwidth [rad/m]

Acknowledgements

I wish to thank many people who helped me during my PhD research.

First of all, I am grateful to my tutor Prof. Giorgio Franceschetti who has supported me for all the time of my PhD.

Furthermore, I am indebted with all my colleagues from DIET at University of Naples Federico II, and from IREA-CNR of Naples for their help, friendship and support.

Special thanks are due to Antonio Iodice for stimulating discussions.

Words of thanks go to Joao R. Moreira and Christian Wimmer from ORBISAT Remote Sensing, for providing the Airborne data and for their gentleness and hospitality.

Last, but not the least, my best acknowledgements go to my colleague Gianfranco Fornaro for his invaluable support; he continually stimulates my interest for research and study with suggestions, discussions and constructive criticisms.

Finally, I have to thank Mariarosaria, Anna Maria and Carmine without their sustain all this would not ever have been possible.

